TÉCNICO LISBOA

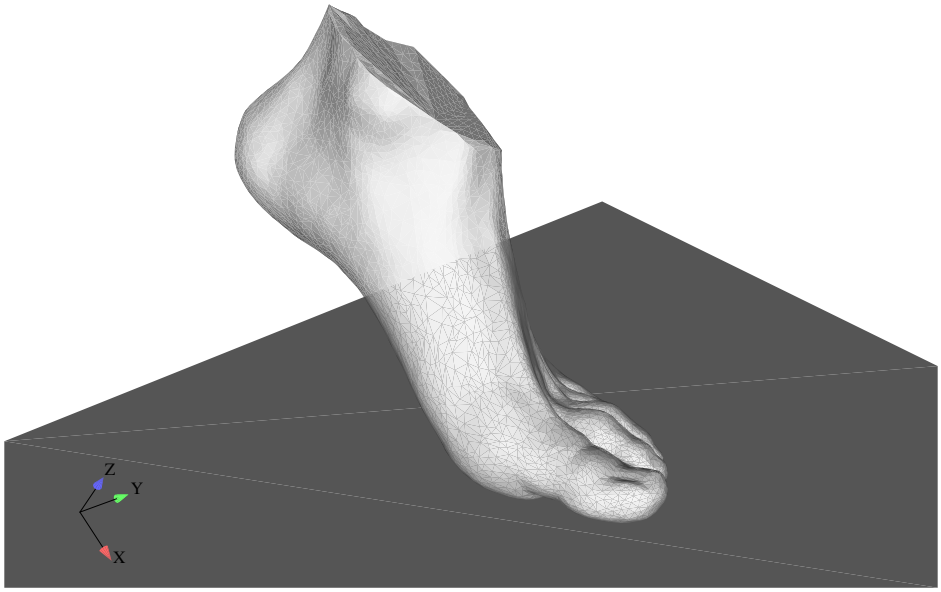

Simulation and Analysis of the Foot-Ground Interaction using a MSD-FEM Co-simulation Approach

Francisco Aires Martins Guedes de Melo

Thesis to obtain the Master of Science Degree in

Mechanical Engineering

Supervisors: Prof. Miguel Pedro Tavares da Silva
Prof. Pedro Miguel de Almeida Areias

Examination Committee

Chairperson: Prof. Luís Filipe Galrão Reis
Supervisor: Prof. Miguel Pedro Tavares da Silva
Member of the Committee: Prof. João Orlando Marques Folgado

November 2023

Declaration

I declare that this document is an original work of my own authorship and that it fulfills all the requirements of the Code of Conduct and Good Practices of the Universidade de Lisboa.

Acknowledgments

To my supervisors, Professor Miguel Tavares da Silva, for introducing me to the fascinating world of Biomechanics and for the constant support and encouragement in the development of this work, and to Professor Pedro Areias, for the motivation and broad sharing of knowledge in the area of computational analysis.

To my colleague Sérgio Gonçalves for his continuous availability and support for experimental and numerical work.

To my colleagues at Instituto Superior Técnico and Academia de Música de Santa Cecília for their companionship throughout this journey.

To my family, in particular my parents and siblings, for their trust and enthusiasm throughout the development of my work, and to Margarida for her tireless support, always providing extra motivation.

Resumo

O uso humano de exoesqueletos tem aumentado nos últimos anos e, portanto, o desenvolvimento de ferramentas computacionais para simulação e melhoramento das interações homem-máquina e homem-ambiente é fundamental.

Este trabalho descreve uma nova metodologia para a análise dinâmica e estrutural de sistemas biomecânicos que apresenta a utilização de um software de Dinâmica de Sistemas Mecânicos (DSM) em constante comunicação com um programa do Método de Elementos Finitos (MEF). O software DSM fornece a posição relativa dos corpos em contato ao programa MEF que realiza a deteção de contacto e o cálculo das respetivas forças, que são reportadas de volta ao primeiro código. A metodologia de co-simulação implementada combina a simplicidade e eficiência da formulação multicorpo no tratamento da cinemática e cinética global do sistema com a análise estrutural detalhada fornecida pelo MEF.

A primeira aplicação do código desenvolvido foi o problema base de contacto bola-plano e os resultados obtidos foram validados através da comparação com um modelo de contato já estabelecido. Seguidamente foi considerada a simulação do contacto pé-solo durante a marcha humana, envolvendo a aquisição de dados experimentais de natureza geométrica, cinemática e cinética, e no desenvolvimento de um modelo de pé geometricamente preciso mas fisiologicamente simplificado. As forças de reação do solo e as distribuições de pressão obtidas provaram ser consistentes com os dados experimentais correspondentes. No entanto, algumas discrepâncias são destacadas principalmente relacionadas com o modelo de fricção simplificado considerado e à posição elevada dos dedos do pé na geometria digitalizada 3D utilizada no modelo do pé.

Palavras-chave: Co-Simulação, Sistemas Multicorpo, Elementos Finitos, Contacto Pé-Chão, Marcha Humana.

Abstract

The human use of exoskeletons has been rising in recent years and, therefore, the development of computational tools to simulate and improve human-machine and human-environment interactions is fundamental.

This work describes a new methodology for the dynamic and structural analysis of biomechanical systems that features the use of a Multibody System Dynamics (MSD) software in constant communication with a Finite Element Method (FEM) program. The MSD software provides the relative position of the contacting bodies to the FEM program that performs contact detection and the calculation of the contact forces, which are reported back to the multibody side of the code. The implemented co-simulation methodology combines the simplicity and efficiency of the multibody formulation in handling the global kinematics and kinetics of the system with the detailed structural analysis provided by FEM.

The first application of the developed software was the benchmark problem of the bouncing ball and the obtained results were validated through comparison with an already established contact model. Next, the simulation of foot-ground contact during human gait was considered, resulting in the acquisition of experimental data of geometric, kinematic and kinetic nature, and the development of a geometrically accurate but physiologically simplified foot model. The obtained ground-reaction forces and pressure distributions proved to be consistent with the correspondent experimental data. However, some discrepancies are highlighted mainly related to the simplified friction model considered and the elevated position of the toes in the 3D scanned geometry used for the foot model.

Keywords: Co-Simulation, Multibody Systems, Finite Element, Foot-Ground Contact, Human Gait.

Contents

List of Tables

List of Figures

Nomenclature

List of Acronyms

2D - Two Dimensions

3D - Three Dimensions

ADF - Approximate Distance Function

CoM - Center of Mass

CoP - Center of Pressure

DoF - Degree of Freedom

FCC - Fully Cartesian Coordinates

FEM - Finite Element Model

MSD - Multibody System Dynamics

ODE - Ordinary Differential Equations

PDE - Partial Differential Equation

PPT - Pressure Pain Thresholds

List of Symbols

Γ - Boundaries of a generic body

$\mathbf{\Delta u}$ - Nodal displacement

δ - Relative normal contact deformation

$\dot{\delta}$ - Relative normal contact velocity

$\dot{\delta}^{(-)}$ - Initial relative normal contact velocity

λ - Vector of the Lagrange multipliers

ν - Poisson's ratio

ξ, η, ζ - Local coordinates of reference frame

$\mathbf{\Phi}$ - Vector of kinematic constraints

$\mathbf{\Phi_q}$ - Jacobian matrix

ϕ - Potential function

χ - Hysteresis damping factor

ψ - Vector of shape functions

Ω - Deformed configuration of a generic body

$\mathbf{A}$ - Transformation matrix

$\mathbf{C}$ - Transformation matrix (Chapter 3); Right Cauchy-Green deformation tensor (Chapter 4)

c_r - Coefficient of restitution

E - Young modulus

F - Gradient of deformation

F_N - Contact force

g - Gap function

$\mathbf{g}$ - Vector of generalized external forces

K - Generalized stiffness matrix

$\mathbf{M}$ - Global mass matrix

$\mathbf{q}$ - Generalized coordinate vector

$\dot{\mathbf{q}}$ - Generalized velocity vector

$\ddot{\mathbf{q}}$ - Generalized acceleration vector

$\mathbf{r}$ - Global position vector (Chapter 3); Residual vector (Chapter 4)

$\dot{\mathbf{r}}$ - Global velocity vector

$\ddot{\mathbf{r}}$ - Global acceleration vector

$\mathbf{r}$ - Residual vector

Chapter 1

Introduction

1.1 Motivation

In the animal kingdom, an external skeletal structure that provides support and protection against predators and the environment is known as an exoskeleton [1]. When referring to humans, an exoskeleton is a structural mechanism worn externally in order to enhance physical performance [2, 3]. Interest in exoskeletons and their potential in both rehabilitation of patients with disabilities and performance enhancement of healthy subjects has been growing in recent times [4]. When designing an exoskeleton or an assistive device, one of the most fundamental aspects to have in consideration is comfort. This type of devices are often used for long periods of time, so discomfort can dictate their acceptance or rejection by the user. Therefore, it is important to study the structural compatibility between the user and the exoskeleton, by estimating the forces generated in the human-machine interface, as these forces are directly related to the pressure and wear transmitted to the skin. Furthermore, at the same level of importance, the adequate characterization of the interface forces generated between the user and the surrounding environment is also of paramount relevance. Not only these forces relate directly with comfort issues but also their accurate estimation is a fundamental input for the correct simulation and analysis of the human movement.

Given that the human body presents significant differences in terms of physiognomy between individuals, the design of exoskeletons usually implies a level of personalization to the user's characteristics. This further exacerbates the need to keep the designing process lean and cheap. Therefore, the inclusion of computational simulation and analysis while designing this type of devices is mandatory, since it allows the iteration phase to occur before prototyping is initiated, reducing waste and, consequently, unnecessary costs. Additionally, and if desired, it provides data for the entire system, while physical measurements are often limited by anatomical access to specific body sections. However, the accuracy in predicting human-exoskeleton contact forces and the resulting movement through computational methods is still limited [5].

In Biomechanics, multibody dynamics methodologies are usually considered for gross-motion analysis and simulation, having as advantages their relative simplicity and low computational cost, but pro-

ducing data with limited accuracy in regards to contact forces. On the other hand, in other fields of engineering, resorting to detailed structural analyses is very common, being the Finite Element Method (FEM) an extremely prominent computational tool to achieve such objective. This methodology is associated with high data accuracy but also with an high computational effort. If made compatible with one another, these two approaches can allow for highly accurate data at significantly lower computational cost.

1.2 Objectives

The main objective of this work is to develop a computational methodology that allows for the detailed and accurate estimation of the human-exoskeleton and human-environment contact forces. With such objective in mind, a co-simulation strategy is adopted, in which a multibody program takes care of the dynamics of the combined system and a finite element method code deals with the complex deformations occurring at the interface. The use of both methodologies in a co-simulation environment is, to the author's knowledge, unprecedented for this type of application and it aims to take advantage of their complementary nature. It is important to note that, even though the main objective of the work refers to contact in the human-machine interface in a general way, meaning it can be in any part of the human body, as a starting point, the study of the interaction between the foot and the ground was selected.

The development of the required software resulted in the addition and adaptation of two already existing computer programs: on the multibody side, a contact module was created and implemented in a *Matlab* (MathWorks, Natick, MA) program developed in house and on the FEM side, a *Fortran* program was adapted and further developed to accommodate the communication with the multibody part. Both programs are briefly described in subsequent sections, while the contact module developed in the context of the this work is presented in more detail, throughout the document.

1.3 Literature Review

In order to contextualize the work developed in this document, a brief overview of the main topics is presented next, including methodologies centered around co-simulation between Multibody System Dynamics (MSD) and Finite Element Method (FEM), the main foot models proposed in recent years, the main marks in the history of exoskeleton design and their main applications, and the study of comfort.

1.3.1 Co-simulation

In this work, a co-simulation methodology is proposed between a MSD software and a FEM program. The two codes are in continuous communication throughout the simulations, complementing each other's strengths and shortcomings by producing precise data at a reduced computational cost.

Co-simulation methodologies between MSD and FEM are still very scarce. Even though its potential is promising, its implementation is rather complex and, therefore, the work produced is still of an ex-

ploratory nature. However, some work has been published with co-simulation methodologies that bridge the gap between these two domains. Monteiro et al. [6] proposed a similar co-simulation methodology to the one used in this present work but applied to the study of cervical spine dynamics, in which an intersomatic fusion is simulated to confirm its potential advantages. Müller et al. [7] presented a co-simulation workflow to predict the patellofemoral joint kinematic behavior and contact, combining rigid body dynamics with a nonlinear finite element analysis. Ambrósio et al. [8] proposed a co-simulation environment that uses an integrated memory shared communication methodology between a multibody and a finite element code applied to the interaction of highspeed catenary-pantograph system. Finally, Dietz et al. [9] and Olivier et al. [10] also applied a co-simulation methodology to simulate the interaction between vehicles (described using MSD) and flexible tracks and soil (associated with FEM).

Although promising, it is possible to conclude that this type of work is quite recent and still in early development. However, it is expected that, with advances in computational efficiency and development of more generic software, the challenges in combining these two domains will be reduced and they will be more intertwined in the future.

1.3.2 Foot Models

The human foot is a complex system composed by bones, joints, ligaments and muscles, that provide support for the rest of the human body and allow a wide range of different movements. Therefore, a realistic representation of contact in this body section in computational models can be challenging.

A vast array of different foot-ground contact models are proposed in the literature and it is important to understand what type of assumptions and simplifications are considered. Therefore, a brief overview of the main differences found in these models is provided next.

Saraiva et al. [11] present a detailed review of foot-ground contact models considered by different authors, in recent years. This review features 2D and 3D formulations, and both barefoot and shod foot models. Given the scope of this work, only 3D barefoot models were analyzed. The different models can be classified in regards to the geometric representation of the contacting surface, the modeling assumptions considered and the numeric contact model adopted.

In terms of the representation of the foot, models can consider specific contact points or approximate the bottom of the foot as a combination of geometric shapes, depending on the desired accuracy and computational efficiency. In the first case, the number of contact points defined can vary, as well as their location. There are many examples of models that only consider a single contact point [12–15], but cases in which four [16], twelve [17] (see Figure 1.1) or even forty [13] are also available in the literature. In the second case, the most common geometric shapes used are spheres [18, 19] and ellipsoids [20].

Moreira et al. [21] proposed a model in which the main foot and the toes are represented by a set of spheres, as illustrated in Figure 1.1(b). Contact is simulated between these spheres and the rigid floor, using a contact model based on the work by Kelvin-Voigt and Hunt and Crossley, which are discussed in detail in the next section.

Jansen et al. [18] also described the foot's geometry with the use of spheres, but proposed a dif-

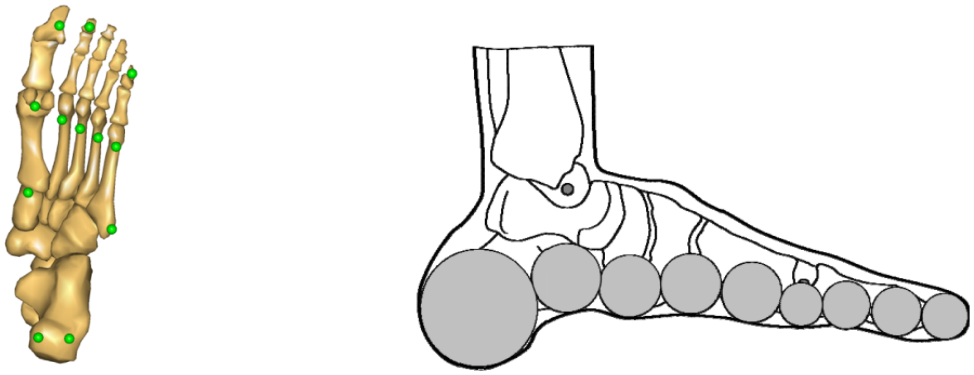

(a) (b)

Figure 1.1: Foot-ground contact models proposed by Fluit et al. [17] (a) and Moreira et al. [21] (b).

ferent contact model: the elastic foundation method. In this method, contacting bodies are considered rigid with a thin layer of elastic material in their surfaces. The geometry of each contacting surface is approximated with a triangular mesh of suitable density, and at the centroid of each triangular element a spring is placed. In contacting elements, a contact force is calculated in terms of the characteristics of the corresponding spring. The stiffness of this spring is associated with the area of the respective element, the mechanical properties of the chosen material and the thickness of the elastic layer [22].

Another common simplification, which was considered by Moissenet et al. [12] and also adopted in this present work, is the assumption of null acceleration and velocity at the contact point throughout the entire contact phase. This can have implications on the results, depending on the friction model applied, which will be discussed later in this document.

A deeper analysis of the main contact models considered in this work is presented in the next chapter, in which their numerical formulations are compared.

1.3.3 Exoskeleton Design

There is no denying that the interest in exoskeletons and their potential in solving human physical shortcomings in different fields in society has been increasing in recent years. This is evident by the increased number of scientific papers being published on the topic, year after year [23, 24].

Before briefly exploring the evolution of exoskeletons through time, it is important to note that several types of these devices can be identified based on their application purpose. As previously mentioned, exoskeletons can have different purposes (replacement of normal physical performance, rehabilitation or enhancement beyond human capabilities) and, therefore, be applied in different fields of society (biomedical, industrial, military or sports). They can also be divided into: active and passive, in regards to type of actuation and power consumption [25]; tethered and untethered, in terms of their adaptability to everyday outside a clinical environment [26]; and between weight-bearing (which transfer load directly to the ground and reduce the user's physical stress) and joint-targeting (in which an additional torque is applied to a specific joint or joints in order to achieve a physiological goal [27]). Exoskeletons can also support the entire human body or only interfere with a specific section.

The earliest mention of a device similar in appearance and purpose to what is considered an exoskeleton nowadays dates back to 1890, when Nicholas Yagin, a russian engineer, developed an apparatus for assisting movement. He was granted a US patent for his device, which could be described as a long bow operating in parallel to the legs of the user [1, 24]. This mechanical structure would assist the user in walking, running and jumping, and its concept model is presented in Figure 1.2.

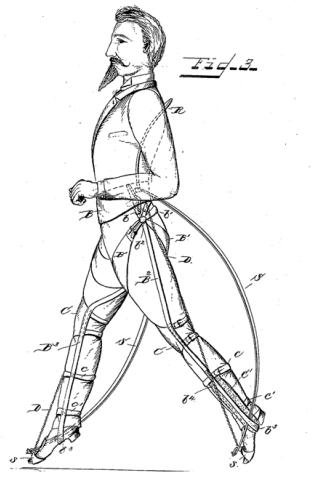

Figure 1.2: Concept model of Yagin's exoskeleton [28].

The term "exoskeleton" was only associated with its current meaning in the 1960s, when the US Armed Forces and General Electric created the first powered exoskeleton, named Hardiman, which allowed a ratio of strength enhancement of 25 for human limbs, it had 30 degree of freedoms and weight around 680 kg [1, 24].

In more recent years, in 2004, the Human Engineering and Robotics Laboratory of the University of California, Berkeley, presented BLEEX to the world, the first functional energetically autonomous load carrying human exoskeleton (see Figure 1.3(a)). This exoskeleton was designed for strength and endurance enhancement of soldiers, disaster relief workers, wildfire fighters, and other emergency personnel [29]. Another modern example of an exoskeleton designed for a military environment and, therefore, to augment the performance of physically able users is HULC [30] (see Figure 1.3(b)).

However, as previously mentioned, exoskeletons can also be developed to replace or rehabilitate the user's natural physical ability. University of Tsukuba's HAL exoskeleton (see Figure 1.4) specializes in assisting users who suffer from spinal cord injuries, traumatic brain injuries and cerebrovascular diseases. It detects the user's bio-electrical signals sent by the brain to the muscular system when a movement is eminent and performs referred movements in accordance with the wearer's voluntary commands [31]. Other examples in the medical field are eLEGS (see Figure 1.4, once again from Berkeley, which targets paraplegic users and gives them the ability to stand and walk again with the aid of crutches [32]; ReWalk (see Figure 1.4), which provides powered hip and knee motion to enable individuals with spinal cord injury to stand upright, walk, turn and climb and descend stairs; and ReStore (see Figure 1.4), which focuses on the rehabilitation of individuals with lower limb disability due to stroke and illustrates that, depending on the size of the targeted area, exoskeletons can vary in their bulkiness [33].

(a) (b)

Figure 1.3: Berkeley Lower Extremity Exoskeleton (BLEEX) [29] (a) and Human Universal Load Carrier (HULC) [30] (b).

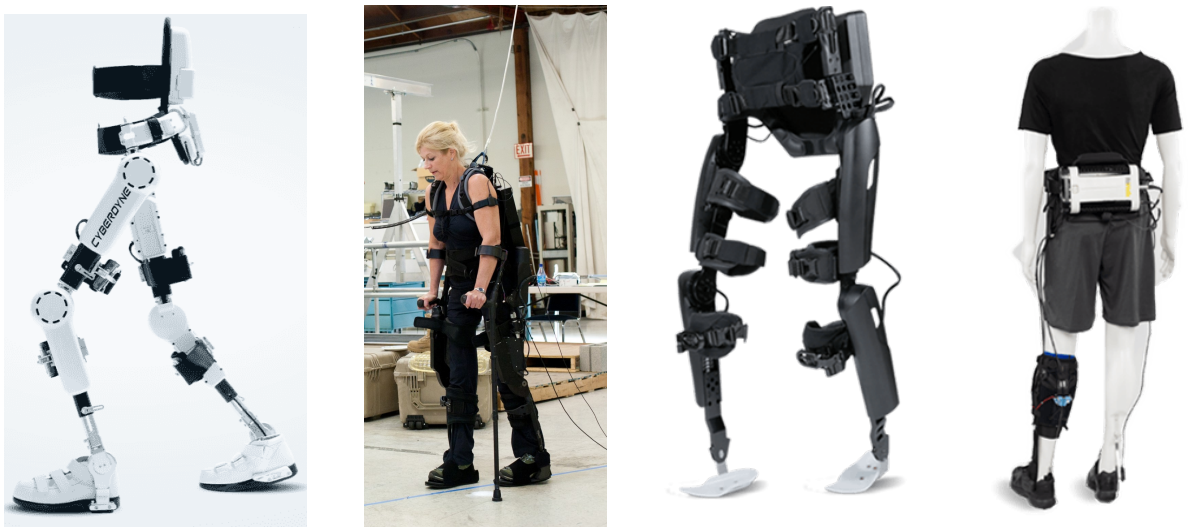

(a) (b) (c) (d)

Figure 1.4: Exoskeleton types: HAL [34] (a), eLEGS [32] (b), ReWalk [33] (c) and ReStore [33] (d).

1.3.4 Comfort

As previously stated, a comfortable adjustment of an exoskeleton over the biological structures of the user is instrumental. When wearing an exoskeleton or an orthosis, contact and friction forces between the device and the skin tend to develop, and the magnitude of said forces is crucial if the design is to take into account the patient's comfort. In particular, if the exoskeleton is to be used by people with neuromuscular pathologies, the lack of sensitivity in the lower limbs can often lead to wounds as a

consequence of inappropriate designs [35].

Therefore, it is extremely important to define the user's comfort and to find ways to measure it, especially because it is a very subjective concept.

The term comfort is often used on the basis of common knowledge regarding its meaning. It is expected that the meaning is self evident, leaving its definition rather dubious [36].

Oxford's Dictionary defines *comfort* as "the state of being physically relaxed and free from pain" [37], while, as stated in [22], Zhang et al. define it as lack of discomfort or a feeling of well-being. Both of these definitions present two ways of measuring comfort: by quantifying a person's wellness or by their lack of discomfort. The latter is often preferred because the physiological mechanisms associated with discomfort or pain are well documented and, therefore, a patient's well being can be determined in relation to their level of unwellness. Discomfort or pain are associated with sensory neurons known as nociceptors, that alert the body to potentially damaging stimuli at the skin, whether it be related to extremes in temperature, pressure and injury-related chemicals. These stimuli are transduced into long ranging electrical signals that are relayed to higher brain centers [38].

In the context of exoskeleton design and other mechanical structures to be used by humans, such as orthosis, comfort is usually evaluated through pressure pain thresholds (PPT), meaning the minimum intensities of pressure stimuli that are perceived as painful [39].

1.4 Thesis Outline

Chapter I - The first chapter serves as an introduction to the work developed. It addresses the motivation behind it and its main objective, while also providing some context regarding its exploratory and, consequently, ever adapting nature. The chapter closes with a brief overview of the topics that are at the core of the work.

Chapter II - The second chapter focuses on delivering theoretical knowledge needed to understand the applied methodology and result analyses presented later.

Chapter III - The third chapter is dedicated to explaining the multibody formulation. Its main equations are presented, the advantages of using the Fully Cartesian Coordinates formulation (FCC) are highlighted and the developed work is contextualized within the multibody system formulation. At the end of the chapter, a multibody software developed in *Matlab* is concisely introduced, accompanied by a brief description of the main additions resultant of this work.

Chapter IV - The fourth chapter shifts the attention to the Finite Element Method side of the work. SimPlas, a FEM *Fortran* software used in this work is presented, and the main computational techniques implemented are described in detail.

Chapter V - The fifth chapter introduces the bouncing ball problem as the benchmark contact example, that is used for theoretical validation of the contact models implemented. The formulation used for each one of the contact models implemented is showcased, followed by the obtained results.

Chapter VI - The sixth chapter marks the transition into practical applications of the developed software. The chapter begins with a listing of all experimental procedures performed in order to gather all the

necessary data. This data includes information used for the formulation of a satisfactory foot model and the kinematic and dynamic behavior of a human foot during a gait cycle (human walking). The chapter ends with the presentation and discussion of the results associated with the gait analysis performed.

Chapter VII - The seventh and final chapter concludes the work with its main considerations, presenting a critical overview of the developed work. The main obstacles are listed, alongside the knowledge gathered from them and remarks are made about what could be done in the future to progress this type of methodology.

Chapter 2

Background

2.1 Ankle-Foot Biomechanics

In order to ensure reasonable simulation results, it is necessary to strive to create a model of the ankle-foot structure as realistic as possible. Therefore, a brief description of its main structural components, how they interact with each other and how that interaction results in motion is presented below.

The ankle-foot system is located in the lower extremity of the human body and it is responsible for supporting its weight during standing and for providing stabilization in gait. Consequently, it is reasonable that the anatomy of the ankle-foot is complex and robust. It is composed of: bones, which provide structural integrity and rigidity; joints, that are associated with flexibility and range of motion; and muscles, which control movement. Given that in the present work the muscular system is not featured in the adopted foot model and its influence is not contemplated in the simulations, they will not be discussed in the present overview.

Two different views of the skeleton structure of the ankle-foot are presented in Figures 2.1 and 2.2, its superior and medial views, respectively.

Starting from the top, the foot is connected to the rest of the human body through the ankle articulation, which connects the talus, in the foot, to the tibia and fibula, located in the lower part of the leg.

The bones in the foot can be organized in three distinct groups: tarsal, metatarsal and phalanx bones. Beginning from the proximal portion of the foot, there are seven tarsal bones. The talus is located on top of the largest and strongest tarsal bone, the calcaneus, which forms the heel and has the Achilles tendon attached to it. The navicular bone sits between the posterior portion of the talus and the anterior section of the cuneifornms (medial, intermediate and lateral). These three bones form a row alongside the cuboid, which is a cube shaped bone that lies on the most lateral position of this distal row [21].

The middle section of the foot is characterized by the metatarsal bones. These long bones form articulations that are connected to the proximal portion of the foot by the tarsometatarsal joints and connected to the distal section of the foot by the metatarsophalangeal joints. There are five metatarsal bones, each associated to one toe, and they are slightly distinct in regards to size and shape. The first

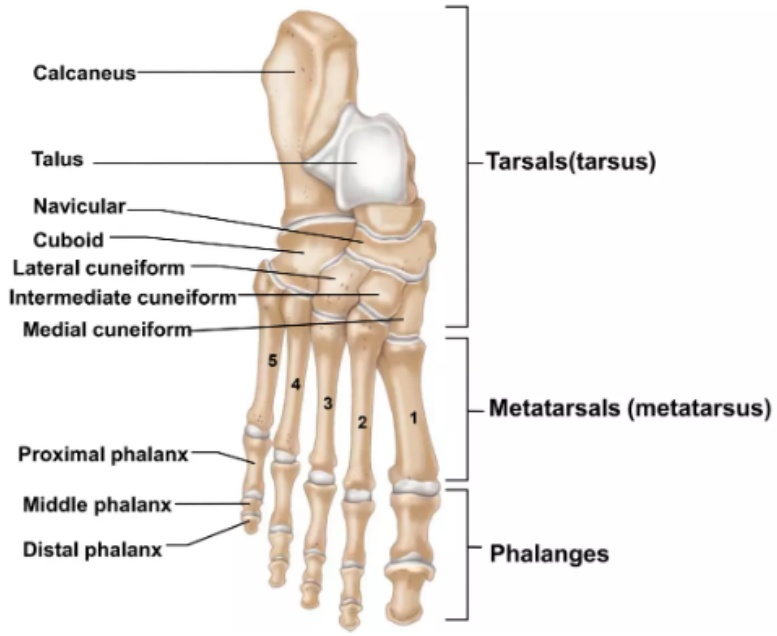

Figure 2.1: Superior view of ankle-foot bone structure [40].

Figure 2.2: Medial view of ankle-foot bone structure [40].

metatarsal is the shortest and widest, and its base articulates with the medial cuneiform. The second metatarsal extends further than the first one, making it the longest of the metatarsal bones, and its base articulates with the intermediate cuneiform, as well as with the medial and lateral cuneiforms in a ”key-like” arrangement. This ensures stability and structural robustness. The additional three metatarsal bones are all very similarly shaped: broad at the base, narrow in the shaft and dome shaped in the head section. The third articulates at its base with the lateral cuneiform, while the fourth and fifth ones are connected to the cuboid [21].

Finally, in the distal portion of the foot, the metatarsal bones are connected through the metatarsophalangeal joints to the phalanx bones. The big toe or hallux, which is associated to the first metatarsal bone, is composed by two phalanges, while all other toes have three phalanges in their structure. The main function of these bones is to ensure stability, weight bearing and distribution, and to promote propulsion during human locomotion and other types of movement [21].

Focusing now on joints, the foot is composed by six main joints, which allow motion and ensure that the body's contact with the floor is done at the most comfortable and stable angle at all times. As seen in Figure 2.3, the six joints are: ankle, subtalar, midtarsal (talonavicular and calcaneocuboid joints), tarsometatarsal, metatarsophalangeal and interphalangeal [21].

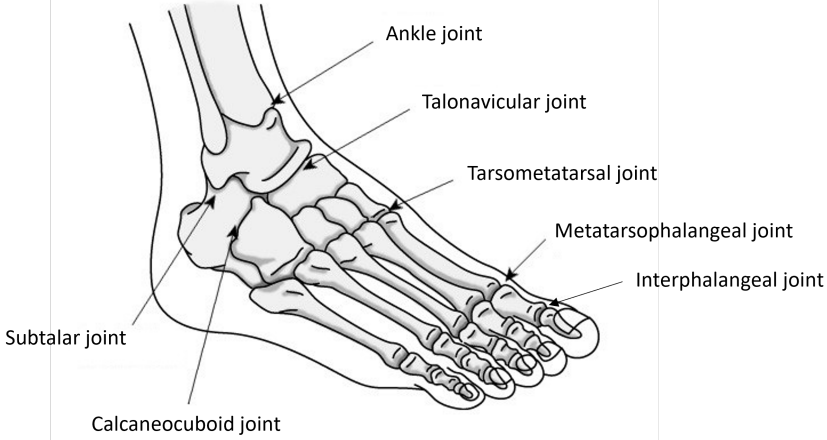

Figure 2.3: Main joints of the ankle-foot [41] (edited).

A joint is a link between two bodies that allows movement (translation or rotation) in some directions, while restricting it in others. In the present case of the ankle-foot system, only rotational joints will be considered. Each rotation occurs about an axis in a plane of motion. In biomechanics, the three planes that define space are the sagittal plane, the frontal or coronal plane and the transverse plane (see Figure 2.4). Before presenting in detail each one of the ankle-foot joints, it is important to define what types of movements are associated with the foot.

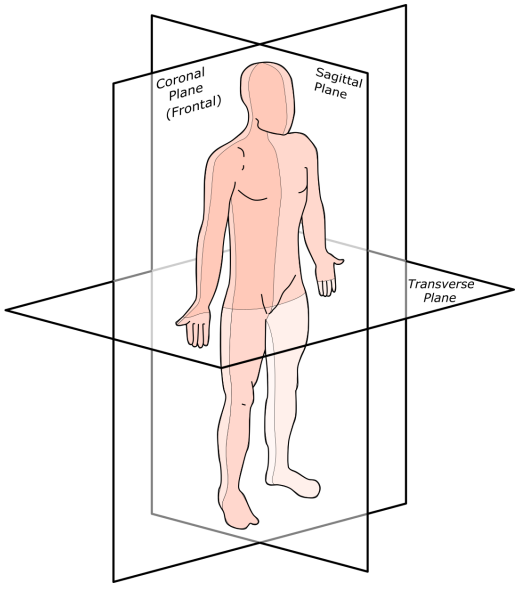

Figure 2.4: Anatomical planes [42].

The foot is capable of performing 4 types of motion: adduction/abduction, plantarflexion/dorsiflexion, inversion/eversion and supination/pronation. Figure 2.5 represents, in a very simple way, the three axis around which the foot is able to rotate.

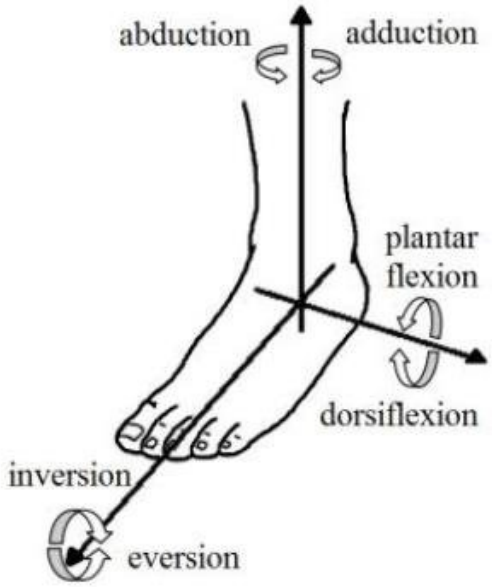

Figure 2.5: Foot movements [43].

Adduction of the foot occurs when its distal section rotates over its proximal section (heel) in the transverse plane, towards the body's midline. Abduction is characterized by a similar rotation but away from the body's midline. Plantarflexion and dorsiflexion of the foot can be described, once again, by a rotation of its distal section over its proximal section, but this time in the saggital plane. Plantarflexion is associated with a downward motion of the foot (away from the tibia), while dorsiflexion describes a upward movement (closer to the tibia). In the frontal plane, the foot is capable of being inverted or everted. The inversion of the foot occurs when it is tilted, such that its plantar surface is facing the body's midline and, naturally, eversion of the foot occurs when its plantar surface is facing away from the body's midline. Finally, supination results from the simultaneous occurance of adduction, inversion and plantarflexion of the foot, while pronation is associated with the combination of abduction, eversion and dorsiflexion of the foot [44].

Now that the available movements of the foot are defined, it is possible to fully characterize each one of the joints and to illustrate how they contribute for its general motion. In regards to number of degrees of freedom, the six foot joints can be organized in two different groups: the midtarsal, metatarsophalangeal and interphalangeal joints have two degrees of freedom, while the ankle, subtalar and tarsometatarsal only have one. The first three joints are responsible for the adduction/abduction and plantarflexion/dorsiflexion of the foot, and it is important to note that these can occur independently.

Starting once again from the distal section of the foot, the ankle joint is the link between the foot and the rest of the human body. It connects the distal section of the tibia to the talus bone and it is responsible for the foot's ability to dorsiflex or plantarflex. The subtalar joint is comprised of both the talocalcaneal joint and the talocalcaneal portion of the talocalcaneonavicular. This joint is associated

with the supination and pronation of the foot. The midtarsal joint is composed by the talonavicular and the calcaneocuboid joints. As previously stated, this joint is associated with two axes of motion, one oblique and the other longitudinal, which are confined to the talonavicular joint and the calcaneocuboid joint, respectively. It is important to note that, although each axis only allows movement in one plane, because the combined angles act in the three body planes, the supination/pronation motions are linked to this joint. The tarsometatarsal joints are located in the interface between the posterior portion of the metatarsal bones and the lesser tarsus, and are only capable of a slight gliding motion (except between the first metatarsal and the medial cuneiform bones, where considerable movement is possible). The metatarsophalangeal joints are located between the round heads of the metatarsal bones and the bases of the phalanges, and are responsible for large extensions of the phalanges but small flexions. Finally, as the name hints to, the interphalangeal joints lay between the phalanges and allow extension, which is linked to abduction, and flexion, which is linked to adduction.

2.2 Gait Cycle and Foot-Ground Contact Forces

Human walking, scientifically referred to as gait movement, can be defined as a method of locomotion involving the use of two legs, alternately, to provide both support and propulsion [45].

Since it is one of the most basic human movements, the interest in analyzing it and breaking it down into different phases has been present in mankind's mind for centuries. Going as far back as ancient Greece, Aristotle (384–322 BCE) is recognized as the first known written reference to the analysis of human walking. Naturally, the tools and procedures available to perform an in depth analysis of the movement were practically non-existent and, therefore, his observations were not scientifically tested and remained, for many centuries, just observations. The further understanding of human anatomy that characterized the time of the Renaissance in Europe or the invention of photography a couple of centuries later are great examples of developments on different scientific fields that provided a gradually more robust basis for the analysis of human locomotion. The most relevant definitions, concepts and analysis techniques tend to be the most recent ones and, consequently, those will be the ones addressed in this work. However, the interest reader on the full historic timeline of human walking related findings is directed to the work developed by Baker [46].

Focusing on the last decades, through the invention of new analysis techniques and gradually more precise data, the characterization of the different phases present in gait has simultaneously become more precise and controversial. The different classifications of the several sub-phases of the gait movement made by the main modern authors in the field are presented in Table 2.1, which was adapted from the work of Baptista [22].

In this work, the classification system considered is the one by Whittle [45], which in turn agreed with the one proposed by Perry [47]. This is regarded as the most commonly used formulation in the field. Even though different authors disagree on the classification of sub-phases, there is consensus around the two main phases and the starting point of a gait cycle, as it will be seen hereafter.

Considering the stride of one leg, each gait cycle is commonly divided into two periods: the stance

Table 2.1: Major classification system of the gait cycle sub-phases (adapted from [22])

Perry (1992)	Sutheland (1994)	Vaughan (1999)	Whittle (2001)	Olney (2005)
Initial Contact	Initial Double Support	Initial Contact	Initial Contact	Heel Strike
Loading Response		Foot Flat	Loading Response	
Midstance	Single Limb Support	Midstance	Midstance	Midstance
Terminal Stance	Second Double Support	Heel-Off	Terminal stance	Push-Off
Pre-swing		Toe-Off	Pre-swing	
Initial Swing	Initial Swing	Acceleration	Initial Swing	Acceleration
Mid-swing	Mid-swing	Mid-swing	Mid-swing	Mid-swing
Terminal Swing	Terminal Swing	Deceleration	Terminal Swing	Deceleration

phase and the swing phase (see Figure 2.6). The stance phase encompasses the period during which the foot is in contact with the ground (around 60% of the cycle), while the swing phase refers to the period in which the foot is in the air for limb advancement (around 40% of the cycle).

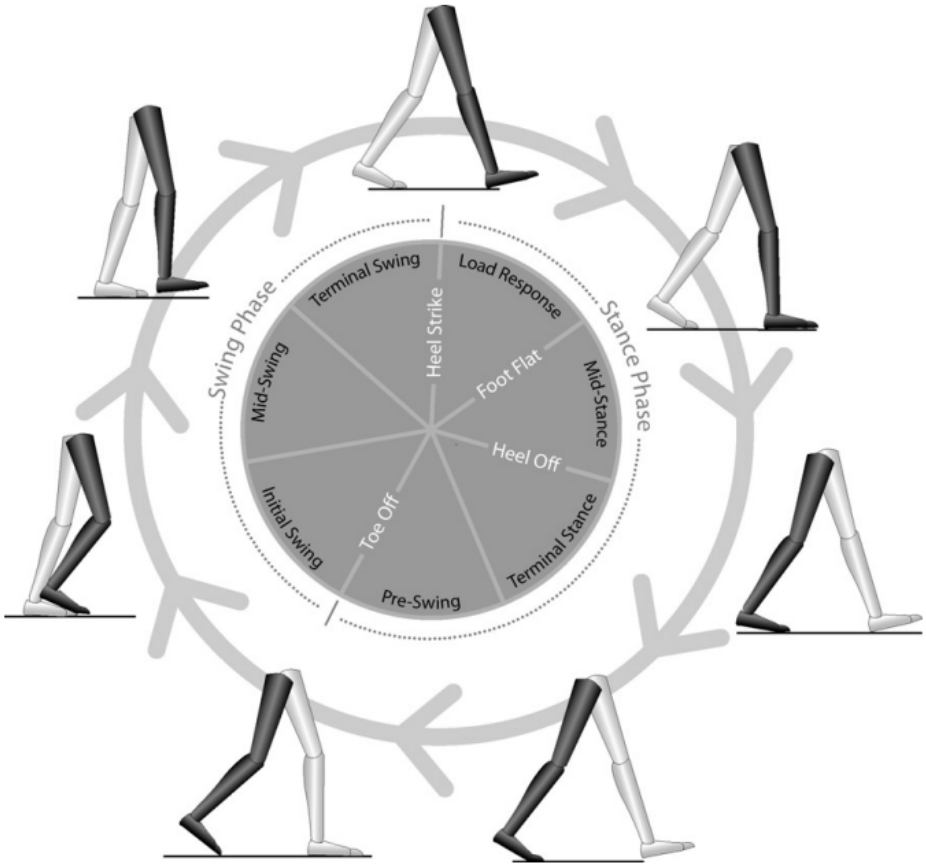

Figure 2.6: Different phases and sub-phases during a gait cycle on a normalized time scale [45].

By definition, a gait cycle is the period of time between any two identical events during walking. However, the common convention dictates that a gait cycle begins and ends with the *heel strike*, marking also the beginning of the *stance phase*. This event is characterized by the initial contact of the leading limb with the ground and marks the beginning of the *load response sub-phase*. This sub-phase sees the leading limb taking over the full body weight by fully placing the foot in contact with the ground.

Once this happens, *foot flat* is achieved. Next, during the *midstance sub-phase*, the body advances and the opposite limb swings forward. This section of the movement puts the subject in some instability, given that the supporting base is smaller and the center of gravity is higher. Once the opposite limb achieves the *heel strike*, the leading limb reaches *heel off*. This event sees the heel lose contact with the ground and it marks the beginning of the *terminal stance sub-phase*. During terminal stance, the body moves forward and as the leading limb gradually reduces contact with the ground, the *pre-swing sub-phase* occurs. The continuous propulsion of the body results in the *toe-off* event, in which the contact between the toes and the ground is lost and the *swing phase* is initiated. During the *swing phase*, the leading limb moves all the way from the back of the body to the front, passing through the opposite limb that is in the *stance phase*. The *swing phase* is divided into three different sub-phases: *initial*, *mid* and *terminal* swing. In the initial *swing sub-phase*, the leading limb accelerates forward, reaching the *mid-swing sub-phase*, in which the swinging limb passes the opposite limb, finally reaching the *terminal swing sub-phase*, in which deceleration occurs in preparation of a new *heel strike* event. Naturally, this ends the *swing phase* and begins a new gait cycle [48].

The identification of specific gait events, phases and sub-phases is instrumental for laying a solid base for nearly all aspects of gait analysis. Gait was previously described in a spatial dimension, meaning the focus was on the positioning and orientation of the limbs, but it can also be described from a temporal perspective. This approach focuses, naturally, on the duration of each section. When dealing with gait analysis, it is important to consider both aspects, since pathologies can affect gait's spatial and temporal components independently [49].

Whether the gait analysis is being performed on a healthy subject or with the purpose of diagnosing a certain pathology, the available techniques and equipment for data collecting have been rising in recent years. Gait analysis, and all other multibody system analysis, are based on kinematic and kinetic data.

On the one hand, the term kinematics refers to the study of a movement without taking into account the underlying forces that cause the movement. The focus is solely in the position, velocity and acceleration of sections of the multibody system. This type of data can be collected from direct measurement of linear and angular displacements of body sections provided by joint angles, limb velocities and accelerations [48]. A more recent method of indirect measurement of the movement is based on motion capture (MOCAP) systems. A group of cameras is set around the laboratory and through reflective markers attached to the body, anatomical relevant points are tracked throughout the movement. It is important to note that markerless MOCAP systems also exist and are starting to be used when the focus is the overall behavior of the whole body, while marker based systems are still preferred when a specific body section is under study, giving their higher precision. In the case of gait analysis, the placement of the markers is more dense on the lower limbs than the rest of the body, as it will be seen in a later chapter.

On the other hand, the term kinetics is associated with the study of the forces and moments that cause motion. These can be gravitational forces, external forces, forces produced by muscle contractions and ground reaction forces. Since the scope of this present work is the accurate determination of the contact forces, the focus is pointed towards ground reaction forces and the respective data collecting techniques and equipment. Ground reaction forces are registered through the use of force plates. These

plates are placed on the ground and the subject is asked to performed the movements on top of them. On the case of gait analysis, the laboratory setup usually resembles the one depicted in Figure 2.7.

Figure 2.7: Laboratory setup for data acquisition for gait analysis [50].

2.3 Contact Models

As previously established, one of the most important aspects in the design of exoskeletons is the user's comfort, which is directly related to the contact forces in the human-machine interface. These forces are associated with contact-impact events that frequently occur and dictate the behavior of multi-body systems [51].

Impact is described by Gilardi et al. [52] as a complex phenomenon which occurs when two or more bodies collide for a very brief duration, involving high force levels, rapid dissipation of energy and large changes in acceleration values. Additionally, contact is assumed to be a continuous process which takes place over a finite time. However, impact and contact are usually used interchangeably.

Contact analysis and models can be divided into two different approaches, depending on the characteristics of the contact problem considered. On the one hand, the nonsmooth dynamics formulation is based on geometrical constraints and considers rigid bodies, meaning deformations are small enough to not influence the global motion of the body. With this formulation, unilateral constraints are used to compute contact impulses that prevent the occurrence of penetration. On the other hand, the regularized approach is associated with flexible bodies, meaning the deformation of the bodies in the contact zone is allowed, and the contact forces are determined based on the indentation or compliance of the contact surfaces. This approach basically considers that the contacting surfaces are covered by spring-damper elements [53]. The nonsmooth dynamics formulation is computationally efficient but it is not fit

for a general-purpose program, requiring distinct numerical strategies for different contact scenarios. In contrast, the regularized or continuous approach is much more capable of handling distinct contact problems, given that some contact parameters are well calibrated, including the equivalent stiffness or the degree of nonlinearity of the indentation. Therefore, given its overwhelming advantages, the regularized approach has been steadily more present in the most popular commercial multibody programs.

Next, some of the main continuous contact models that marked the evolution of the field are presented, starting by the pioneering work of Hertz, over which all of the subsequent models were developed upon.

Hertz's Contact Model

Hertz's work [54] is still regarded as the foundation for the majority of contact problems that arise in all kinds of engineering applications. The model is based on the theory of elasticity and the collision between two spheres of isotropic materials. It relates the contact force with a nonlinear power function of the penetration and it is expressed as

$$F_N = K\delta^n \tag{2.1}$$

where K represents the generalized stiffness parameter, δ is the relative normal deformation between the contacting bodies and n is typically equal to 1.5 for cases where there is a parabolic distribution of contact stresses, as in the original work by Hertz [54]. The generalized stiffness parameter is associated with the material properties and shape of the contacting surfaces.

For the case of contact between two spheres *i* and *j*, K is obtained using the radii of both spheres and their material properties as

$$K = \frac{4}{3(\sigma_i + \sigma_j)}\sqrt{\frac{R_i R_j}{R_i + R_j}}, \tag{2.2}$$

in which the material parameters σ_i and σ_j are obtained through

$$\sigma_l = \frac{1 - \nu_l^2}{E_l} \qquad (l = i, j) \tag{2.3}$$

where ν_l represents the Poisson's ratio and E_l represents the Young's modulus, for each sphere.

It is evident in (2.1) that the contact is being modeled as a nonlinear spring that acts in the direction of the collision and, therefore, it is limited to elastic deformations and does not account for any damping effect. These limitations became the motivation for the subsequent contact models, including the one proposed by Hunt and Crossley [55].

Hunt and Crossley's Contact Model

After the addition of a Kelvin-Voigt like damping term to the Hertz's model [54], Hunt and Crossley [55] demonstrated that the linear spring-damper model does not represent the physical nature of energy

transferred during the contact. Alternatively, they proposed the addition of a nonlinear viscous-elastic element to Hertz's force-deformation law, resulting in

$$F_N = K\delta^n + \chi\delta^n\dot{\delta} \tag{2.4}$$

where $\dot{\delta}$ is the relative normal contact velocity and χ is the hysteresis damping factor, which is given by

$$\chi = \frac{3K(1-c_r)}{2\dot{\delta}^{(-)}} \tag{2.5}$$

in which, once again, K represents the generalized stiffness parameter, c_r represents the coefficient of restitution and $\dot{\delta}^{(-)}$ represents the initial contact velocity.

Therefore, the Hunt and Crossley's model can be represented in a more concise form as

$$F_N = K\delta^n\left[1 + \frac{3(1-c_r)}{2}\frac{\dot{\delta}}{\dot{\delta}^{(-)}}\right] \tag{2.6}$$

This model solved some problems that its predecessors had, regarding discontinuities at the initial and final instants of contact, that is, contact starts and ends with a null value for the contact force [51].

By observing (2.5), it is possible to note that when considering a perfect plastic contact, i.e., $c_r = 0$, the hysteresis damping factor is not infinite as it would be expected. Consequently, this model is suited for hard contacts with high values of the restitution coefficient, and it does not accurately predict contact between soft materials. This was the motivation for the model presented by Flores, which is discussed in the next section.

Flores Contact Model

With a similar expression as (2.6), Flores' model [51] is described by

$$F_N = K\delta^n\left[1 + \frac{8(1-c_r)}{5c_r}\frac{\dot{\delta}}{\dot{\delta}^{(-)}}\right] \tag{2.7}$$

with

$$\chi = \frac{8K(1-c_r)}{5c_r\dot{\delta}^{(-)}} \tag{2.8}$$

As previously mentioned, this model aims to address contact problems, regardless of the restitution conditions felt (from soft to hard materials). From the analysis of (2.8) it becomes clear that for a perfectly elastic contact (c_r = 1), the hysteresis damping factor assumes a null value, and when the contact is purely plastic (c_r = 0), the hysteresis damping factor is infinite, which is coherent from a physical point of view [51].

Chapter 3

Multibody Dynamics with Fully Cartesian Coordinates

A multibody system can be defined as an array of rigid or flexible bodies that have their relative motion constrained by kinematic joints and that are acted upon by forces. These forces may be associated with springs, dampers, actuators or external forces [21].

In this section, the main equations associated with multibody dynamics are presented, followed by a brief description of the Fully Cartesian Coordinates (FCC) formulation, highlighting its advantages. Finally, the focus of this present work is formally defined, contextualizing it within the methodolgy associated with multibody dynamics.

3.1 Fundamental Equations of Multibody Dynamics

Since the FCC formulation is associated with dependent coordinates, the vector of generalized coordinates $(\mathbf{q})$ is composed by a greater number of coordinates than the degrees of freedom (DoFs) of the system. Therefore, the need for kinematic constraint equations arises in order to express the dependencies between generalized coordinates. These equations form the vector of kinematic constraints of the system $(\mathbf{\Phi})$, resulting in the following expression:

$$\mathbf{\Phi}(\mathbf{q}, t) = \mathbf{0} \tag{3.1}$$

The solution of equation (3.1) provides the kinematic consistent position of any element of the multibody system during the analysis' period. Its solution is obtained numerically, given its non-linearity nature. Several numerical methods could be selected but the Newton-Raphson method was the one chosen in this present work, and it was implemented as represented in equations (3.2):

$$\begin{cases} \mathbf{\Phi_q} \mathbf{\Delta q}_k = -\mathbf{\Phi}(\mathbf{q}_k, t) \\ \mathbf{q}_{k+1} = \mathbf{q}_k + \mathbf{\Delta q}_k \end{cases} \tag{3.2}$$

where $\mathbf{\Phi_q}$ represents the Jacobian matrix of the system, which is composed by the partial derivatives of the kinematic constraints, with respect to the generalized coordinates. For a certain time step *t*, the index *k* represents the iteration number and $\mathbf{\Delta q}_k$ is the residual of the Newton-Raphson method. The iteration process will occur until the norm of the residual vector ($\|\mathbf{\Delta q}_k\|$) is smaller than a specified tolerance.

In order to fully characterize the kinematics of the system, it is necessary to define the generalized velocities ($\dot{\mathbf{q}}$) and accelerations ($\ddot{\mathbf{q}}$). The following equations are considered:

$$\dot{\mathbf{\Phi}}(\mathbf{q}, \dot{\mathbf{q}}, t) = \mathbf{0} \Leftrightarrow \mathbf{\Phi_q}\dot{\mathbf{q}} = \nu = -\mathbf{\Phi}_t \tag{3.3}$$

$$\ddot{\mathbf{\Phi}}(\mathbf{q}, \dot{\mathbf{q}}, \ddot{\mathbf{q}}, t) = 0 \Leftrightarrow \mathbf{\Phi_q}\ddot{\mathbf{q}} = \gamma = \nu_t - (\mathbf{\Phi_q}\dot{\mathbf{q}})_\mathbf{q}\dot{\mathbf{q}} \tag{3.4}$$

where ν and γ represent the right-hand-side vectors of the velocity and the acceleration equations, respectively. Additionally, $\mathbf{\Phi}_t$ and ν_t are the vectors that hold the partial derivatives of $\mathbf{\Phi}$ and ν with respect to time.

For a constrained multibody system, the equations of motion are as follows:

$$\mathbf{M}\ddot{\mathbf{q}} + \mathbf{\Phi}_\mathbf{q}^T\lambda = \mathbf{g} \tag{3.5}$$

where $\mathbf{M}$ represents the global mass matrix of the system, λ is the vector of the Lagrange multipliers and $\mathbf{g}$ is associated with the vector of generalized external forces.

Equation (3.5) can be solved through two different perspectives: forward dynamics and inverse dynamics.

Forward Dynamics

When analyzing a problem from a forward dynamics' perspective, one is interested in obtaining the system's response to a set of known external forces. This means that the unknown variables are the system's generalized accelerations ($\ddot{\mathbf{q}}$) and the Lagrange multipliers (λ). In order to assure the same number of equations as the number of unknown variables, equation (3.4) is also considered, and the system of equations of motion becomes:

$$\begin{bmatrix} \mathbf{M} & \mathbf{\Phi}_\mathbf{q}^T \\ \mathbf{\Phi_q} & \mathbf{0} \end{bmatrix} \begin{Bmatrix} \ddot{\mathbf{q}} \\ \lambda \end{Bmatrix} = \begin{Bmatrix} \mathbf{g} \\ \gamma \end{Bmatrix} \tag{3.6}$$

The sequence of steps that characterize forward dynamic analysis is schematically represented in Figure 3.1 and briefly described hereafter.

Forward dynamic analysis begins with an initialization step that checks the consistency of the initial conditions for the generalized position and velocity vectors. Next, the global mass matrix $\mathbf{M}$, the Jacobian matrix $\mathbf{\Phi_q}$, the vector of generalized forces $\mathbf{g}$ and the right-hand-side vector of the acceleration equation γ are assembled and evaluated. Once these variables are defined, the equations of motion

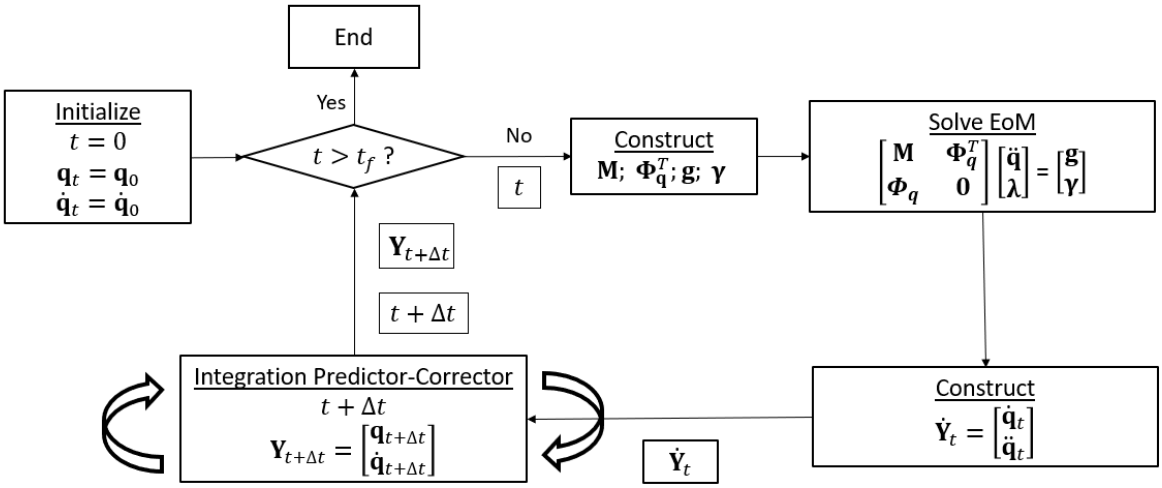

Figure 3.1: Flowchart of Forward Dynamic Analysis.

are solved and the generalized acceleration vector at the current time t_i is determined, as well as the Lagrange multipliers λ. Once this is achieved, by numerical integration of the generalized velocity and acceleration vectors, the generalized position and velocity vectors at the following time instant t_{i+1} are determined. The type of integrator used in this work will be discussed in a subsequent section as well as the predictor-corrector integration method. If the new time instant is higher than the final time of the simulation ($t_i > t_f$), the process ends. Otherwise, it repeats itself, starting from the assembling step with the data associated with the new time instant.

Inverse Dynamics

When an inverse dynamics strategy is chosen, one is focused in obtaining the system's response to known kinematics and external forces. In this case, the Lagrange multipliers are the only unknown variables and, therefore, the solution can be found directly from:

$$\boldsymbol{\Phi}_{\mathbf{q}}^T \lambda = \mathbf{g} - \mathbf{M}\ddot{\mathbf{q}} \tag{3.7}$$

3.2 Fully Cartesian Coordinates Formulation with Generic 3D Rigid Body

3.2.1 Generic 3D Rigid Body

The generic rigid body is the central piece in the FCC formulation, and so its clear definition is of the upmost importance. For a generic 3D rigid body *i*, its generalized coordinate vector ($\mathbf{q}_i$) is composed by one point and one directional vector, as follows:

$$\mathbf{q}_i = \begin{Bmatrix} \mathbf{r}_{O_i}^T & \mathbf{v}_{1_i} & \mathbf{v}_{2_i} & \mathbf{v}_{3_i} \end{Bmatrix}^T \tag{3.8}$$

in which $\mathbf{r}_{O_i} = \begin{Bmatrix} x_i & y_i & z_i \end{Bmatrix}^T$ is the position vector of point O_i, and x_i, y_i and z_i its cartesian coordinates. Furthermore, $\mathbf{v}_{1_i}$, $\mathbf{v}_{2_i}$ and $\mathbf{v}_{3_i}$ are the direction unit vectors that characterize the body's reference frame.

As established, the generalized coordinate vector ($\mathbf{q}_i$) is a column vector with twelve entries. However, a generic 3D rigid body only possesses six DoFs, which means the generalized coordinates are not independent. Therefore, six kinematic constraints of the rigid body ($\mathbf{\Phi}$) are required to expressed the said dependencies. These unit module constraints guarantee the rigid nature of the body and are defined as follows:

$$\mathbf{v}_{j_i}^T \mathbf{v}_{j_i} - 1 = 0, \quad j = 1, 2, 3 \tag{3.9}$$

$$\mathbf{v}_{1_i}{}^T \cdot \mathbf{v}_{2_i} = 0 \tag{3.10}$$

$$\mathbf{v}_{2_i}{}^T \cdot \mathbf{v}_{3_i} = 0 \tag{3.11}$$

$$\mathbf{v}_{3_i}{}^T \cdot \mathbf{v}_{1_i} = 0 \tag{3.12}$$

Consequently, for a general 3D multibody system composed of *nb* unconstrained rigid bodies, the global generalized coordinate vector and global kinematic constraints vector are, respectively, defined as:

$$\mathbf{q}_{(nc\times 1)} = \begin{Bmatrix} \mathbf{q}_1^T & \dots & \mathbf{q}_i^T & \dots & \mathbf{q}_{nb}^T \end{Bmatrix}^T \tag{3.13}$$

$$\mathbf{\Phi}_{(nh\times 1)} = \begin{Bmatrix} \mathbf{\Phi}_1 & \dots & \mathbf{\Phi}_i & \dots & \mathbf{\Phi}_{nb} \end{Bmatrix}^T = \mathbf{0} \tag{3.14}$$

where $nc = 12nb$ represents the total number of generalized coordinates of the system and $nh = 6nb$ represents the total number of kinematic constraints of the rigid body type.

Now that the generic 3D rigid body is defined, the main aspects of the FCC formulation that were relevant for the development and implementation of this work are presented in the next section.

3.2.2 Kinematics of Generic Points and Vectors

While using the previously presented definition of a generic 3D rigid body, one guarantees that the position and orientation of all bodies of the system is fully known throughout the analysis. This means that the kinematics of any generic point or vector, belonging to a given rigid body, are fully determined and can always be calculated from the vector of generalized coordinates ($\mathbf{q}$) of the rigid body.

Kinematics of a generic point

Considering a generic point *P* that belongs to a generic rigid body *i*, its position can be described in two different ways: using the rotation matrix $\mathbf{A}$ or using the transformation matrix $\mathbf{C}$, depending on the convenience of the calculation.

When considering the system's global reference frame xyz, the position of a generic point *P* can be described through the position vector $\mathbf{r}_P$, such that $\mathbf{r}_P = \begin{Bmatrix} x_P & y_P & z_P \end{Bmatrix}^T$. Alternatively, it can also be described as the sum of vectors $\mathbf{r}_{Oi}$ and $\mathbf{r}_{OiP}$, resulting in:

$$\mathbf{r}_P = \mathbf{r}_{Oi} + \mathbf{r}_{OiP} \tag{3.15}$$

where vector $\mathbf{r}_{Oi}$ is the position vector of the origin point of body *i*'s local reference frame and vector $\mathbf{r}_{OiP}$ is the vector that goes from point O_i to point *P*, in the global reference frame.

In the first case, considering body *i*'s local reference frame $\xi_i\eta_i\zeta_i$, equation (3.15) can be changed into:

$$\mathbf{r}_P = \mathbf{r}_{Oi} + \mathbf{A}_i\mathbf{r}'_{O_iP} \tag{3.16}$$

in which $\mathbf{A}_i$ represents the transformation matrix associated with the orientation of the local reference frame of body *i* in respect to the global reference frame and $\mathbf{r}'_{O_iP}$ represents the vector that goes from point O_i (origin of body *i*'s local reference frame) to point *P*, in the body's local reference frame. Matrix $\mathbf{A}_i$ is simply composed by the body's local reference vectors as column vectors:

$$\mathbf{A}_i = \begin{bmatrix} \mathbf{v}_{1_i} & \mathbf{v}_{2_i} & \mathbf{v}_{3_i} \end{bmatrix} \tag{3.17}$$

Furthermore, since this unitary vectors are orthogonal, matrix $\mathbf{A}$ is, as well, orthogonal (i.e., $\mathbf{A}^T = \mathbf{A}^{-1}$).

In the second case, considering body's *i* general coordinate vector, the position vector $\mathbf{r}_P$ can be obtained through:

$$\mathbf{r}_P = \mathbf{C}_i^P\mathbf{q}_i \tag{3.18}$$

where $\mathbf{C}_i^P$ is a $[3 \times 12]$ constant transformation matrix that expresses the coordinates of a generic point *P* as a function of the generalized coordinates of the generic body to which it belongs, resulting in:

$$\mathbf{C}_i^P = \begin{bmatrix} 1 & 0 & 0 & \xi_i^P & 0 & 0 & \eta_i^P & 0 & 0 & \zeta_i^P & 0 & 0 \\ 0 & 1 & 0 & 0 & \xi_i^P & 0 & 0 & \eta_i^P & 0 & 0 & \zeta_i^P & 0 \\ 0 & 0 & 1 & 0 & 0 & \xi_i^P & 0 & 0 & \eta_i^P & 0 & 0 & \zeta_i^P \end{bmatrix} \tag{3.19}$$

with ξ_i^P, η_i^P and ζ_i^P are the local coordinates of point *P* in the local reference frame of body *i*.

The velocity ($\dot{\mathbf{r}}_P$) and acceleration ($\ddot{\mathbf{r}}_P$) of point *P* can be obtained directly from the constant matrix $\mathbf{C}_i^P$, and from the vector of the generalized velocities ($\dot{\mathbf{q}}_i$) and accelerations ($\ddot{\mathbf{q}}_i$) of body *i*, respectively:

$$\dot{\mathbf{r}}_P = \mathbf{C}_i^P \dot{\mathbf{q}}_i \tag{3.20}$$

$$\ddot{\mathbf{r}}_P = \mathbf{C}_i^P \ddot{\mathbf{q}}_i \tag{3.21}$$

It becomes clear that the use of matrix $\mathbf{C}_i^P$ strongly benefits the computational efficiency when calculating the generalized velocities and accelerations of the system. For a more detailed explanation of how the matrix is formed, the interested reader is directed to Roupa et al. [56].

Contrary to what happens with matrix $\mathbf{C}$, matrix $\mathbf{A}$ is not a constant matrix and needs to be updated in each time step of the analysis.

Kinematics of a generic vector

Following a similar line of thought, let one consider a generic vector $\mathbf{v}$ in the local reference frame of body *i*. This vector can be defined as:

$$\mathbf{v} = \mathbf{C}_i^{\mathbf{v}} \mathbf{q}_i \tag{3.22}$$

where $\mathbf{C}_i^{\mathbf{v}}$ is also a $[3 \times 12]$ constant transformation matrix that expresses the coordinates of a generic vector $\mathbf{v}$ as a function of the generalized coordinates of the generic body to which it belongs, such that:

$$\mathbf{C}_i^{\mathbf{v}} = \begin{bmatrix} 0 & 0 & 0 & \xi_i^{\mathbf{v}} & 0 & 0 & \eta_i^{\mathbf{v}} & 0 & 0 & \zeta_i^{\mathbf{v}} & 0 & 0 \\ 0 & 0 & 0 & 0 & \xi_i^{\mathbf{v}} & 0 & 0 & \eta_i^{\mathbf{v}} & 0 & 0 & \zeta_i^{\mathbf{v}} & 0 \\ 0 & 0 & 0 & 0 & 0 & \xi_i^{\mathbf{v}} & 0 & 0 & \eta_i^{\mathbf{v}} & 0 & 0 & \zeta_i^{\mathbf{v}} \end{bmatrix} \tag{3.23}$$

Similarly to the case of a generic point, this type of matrix allows the direct calculation of the velocity ($\dot{\mathbf{v}}$) and acceleration ($\ddot{\mathbf{v}}$) of the generic vector $\mathbf{v}$, through the generalized velocities ($\dot{\mathbf{q}}_i$) and accelerations ($\ddot{\mathbf{q}}_i$) of body *i*, respectively:

$$\dot{\mathbf{v}} = \mathbf{C}_i^{\mathbf{v}} \dot{\mathbf{q}}_i \tag{3.24}$$

$$\ddot{\mathbf{v}} = \mathbf{C}_i^{\mathbf{v}} \ddot{\mathbf{q}}_i \tag{3.25}$$

3.3 Generalized External Forces

Considering that the main focus of the present work is the detailed description of the contact phenomena, it is deemed necessary to define the way forces, and in particular contact forces, are included in the equations of motion of a multibody system.

The vector of generalized forces associated with body *i* is the sum of the contributions of several different types of forces, such as gravitational forces, external forces, forces exerted by springs and dampers and contact forces, as follows:

$$\mathbf{g}=\left\{\mathbf{g}_{grav}+\mathbf{g}_{ext}+\mathbf{g}_{spring-damper}+\mathbf{g}_{contact}\right\} \tag{3.26}$$

The generalized form of a concentrated force $\mathbf{f}=\{f_x\ f_y\ f_z\}^T$ applied at point *P* is obtained resorting, once again, to the transformation matrix $\mathbf{C}$ that expresses the coordinates of the force application point *P* as a function of the generalized coordinates of the generic body to which it belongs to (equation (3.19)). It can be defined in the following way:

$$\mathbf{g}_i^f=\mathbf{C}_i^{P^T}\mathbf{f} \tag{3.27}$$

Considering the result presented in equation (3.27), the main focus of the present work is, therefore, to accurately determine the contact forces and their relative application points, generated for a given state of the system (i.e., position and velocity) at the interface between the anatomical structure and the surrounding environment. Then assemble those forces into the generalized force vector to be applied to the equations of motion of the system.

A general description of this co-simulation method is provided in the next section.

Chapter 4

Continuum Contact with Static Condensation based on Approximate Distance Function

A multibody *Matlab* software developed in house [56] was used and further developed with the addition of a contact module. This additional module allows contact detection between bodies in a multibody system and allows for contact forces to be added to the vector of generalized forces (g), contributing for more realistic and complete analyses. The module features not only the previously described contact model proposed by Flores et al., but also a new continuum contact model with static condensation based on an approximate distance function. This model is associated with a co-simulation methodology, in which the previously mentioned multibody *Matlab* program is in direct communication with a *Fortran* program based on the finite element method. This program is called *SimPlas* and was also developed in house [57].

In this section, the communication between the two programs associated with the co-simulation methodology adopted is described in detail. Furthermore, the contact model implemented in *SimPlas* is showcased and the main techniuues and concepts used are explained.

4.1 Communication between Programs

In order to contextualize where the communication between *Matlab* and SimPlas occurs in the simulation process, Figure 3.1 was updated into Figure 4.1.

And so, in each time step, when assembling the vector of generalized forces (g), *SimPlas* is called as an executable file, it performs contact detection, it calculates the localized contact forces and returns all the obtained results back to*Matlab*. The two programs communicate through writing and reading of text files.

SimPlas interprets the contact between two bodies as one main body being penetrated by a group of

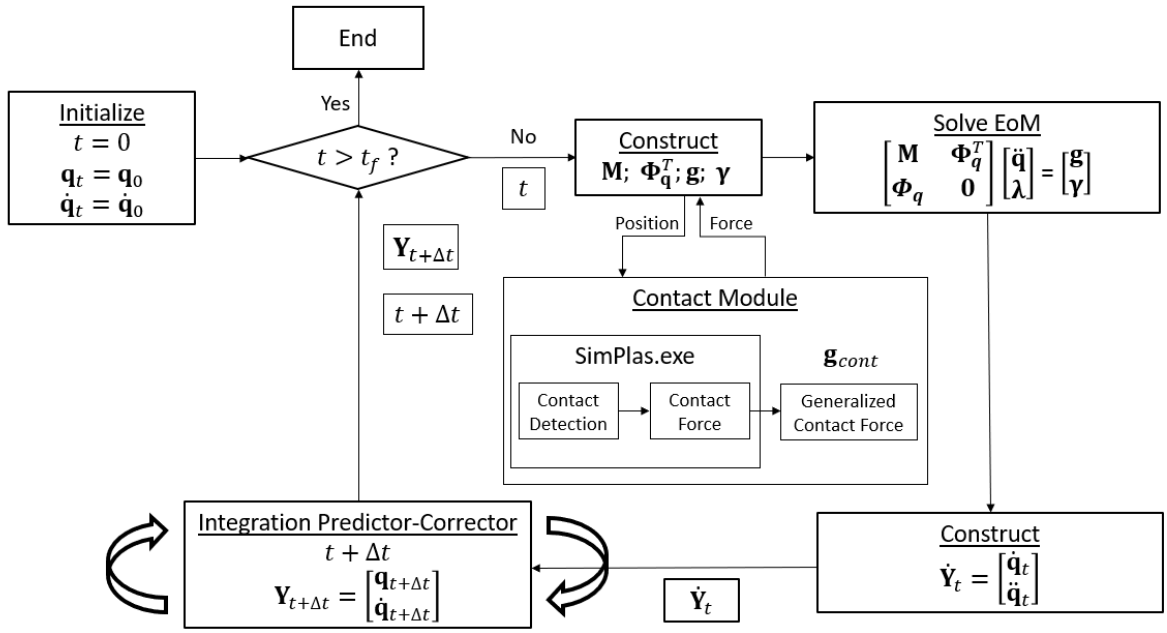

Figure 4.1: Multibody System Diagram with contact module.

points, that represent one secondary body. *SimPlas* is prepared to receive from the *Matlab* program, the relative position of the points associated with the secondary body in the main body's local coordinates. With this information, it is capable of determining if each one of the points has penetrated the main body and so, if contact has occurred (contact detection). In the case of contact, it calculates the respective contact force and reports this information back to *Matlab*, which takes care of turning this localized force into a generalized force and adds it to vector $\mathbf{g}$.

Now, after this general overview of how the two programs communicate, it is important to formally present *SimPlas'* software.

4.2 *SimPlas Program*

SimPlas is a *Fortran* program that utilizes the finite element method to solve a vast array of types of problems, from different fields of engineering. In the present work, it is used to solve contact problems.

Before focusing on the structure of *SimPlas'* software and the computational techniques used to achieve the developed contact model, a brief overview of the considered FEM formulation is presented.

Finite Element Method Formulation

SimPlas is a very complete program that allows a high degree of manipulation by the user, in terms of what type of formulation, computational techniques and inputs they are interested in using. Therefore, since FEM is a broad term that can encompass a lot of different approaches to a specific problem, it is important to clarify, on a general level, what type of assumptions were considered.

Firstly, the type of elements used are four nodes tetrahedral (FEM-TET4) and the shape functions are defined as follows:

$$\psi = \left\{1 - \xi_1 - \xi_2 - \xi_3, \quad \xi_1, \quad \xi_2, \quad \xi_3\right\} \tag{4.1}$$

with ξ_1, ξ_2 and ξ_3 as the coordinates of the parent domain.

Secondly, the gradient of deformation is considered to be:

$$F_{ij} = \frac{\partial \psi_K}{\partial \mathbf{X}_j} \mathbf{X}_{K_i} \tag{4.2}$$

with $i, j = 1, 2, 3$. The subscript *K* is associated to the node being considered and $\mathbf{X}$ represents the position coordinates.

With the gradient of deformation defined, it is possible to establish the right Cauchy–Green deformation tensor as:

$$\mathbf{C} = \mathbf{F}^T \mathbf{F} \tag{4.3}$$

Finally, it was considered the compressible neo-Hookean material model. This model is a hyperelastic material model, often utilized in computational mechanics and biomechanics to describe the nonlinear behavior of soft tissues.

SimPlas' Contact Problems

Now that the general interpretation of a contact problem by SimPlas has been described, the next subsections include a detailed presentation of *SimPlas'* software structure, starting by introducing its preprocessing module, *SimPre*, followed by the explanation of how contact detection occurs and the contact model used to calculate the contact forces.

4.2.1 *SimPre* (*SimPlas'* Preprocessing Module)

As part of the preprocessing stage associated with SimPlas, some inputs need to be provided before the multibody simulation can be initiated.

At the current stage of development and as previously mentioned, *SimPlas* performs contact detection between two bodies (one is considered the main body and the other one is designated as secondary). The mechanical properties of the two bodies' materials need to be defined, including the Young modulus and the Poisson ratio, and *SimPlas* also requires that a mesh of the main body be provided as input. Still as part of the preprocessing procedure, *SimPlas* can apply static condensation to the main body, which will be discussed next.

Static Condensation

Static Condensation, also known as static reduction or Guyan reduction, is a technique used in structural analysis and finite element analysis to reduce the size of a complex structure or system. This is obtained by reducing the total number of degrees of freedom to the ones located on the boundary nodes, also called ”master” nodes. This is possible through the condensation of the inner nodes, or ”slave” nodes, that are now expressed through the first ones. After static condensation is applied, and the inner nodes are removed, a superelement remains in the boundary region, that retains the stiffness of the whole model [58, 59]. This simplification results in improved computational efficiency without significantly reducing accuracy in the results.

Considering a generic body associated with a finite element mesh, the first step when applying static condensation is distinguishing between which degrees of freedom should remain and which ones should be condensed and removed. When using FEM, the body's degrees of freedom are associated with its nodes, and so, in other words, the first step is defining which nodes will be featured in the condensed state (master) and which ones can be removed (slave).

Therefore, three groups of degrees of freedom arise and are showcased in Figure 4.2: the DOFs that are solely coupled to linear constituents (inner nodes) and that are associated with the subscript a; the DOFs that are coupled to both linear and nonlinear constituents (interface nodes), which are represented by the subscript b; and the DOFs that are only coupled to nonlinear constituents (outer nodes) and are linked to subscript c.

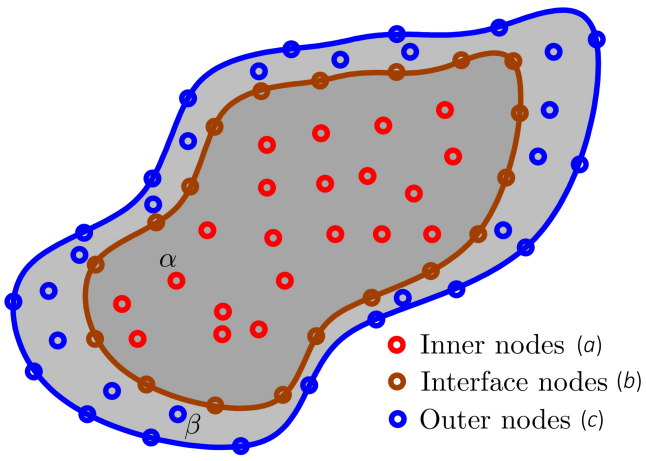

Figure 4.2: Node and constituent partition for a system containing linear and nonlinear constituents.

Furthermore, it is possible to define two sets of elements (or phases) α and β. The first one is composed by elements containing inner nodes and the second one features the elements that do not contain any inner nodes.

Therefore, considering the three sets of nodes (a, b and c) and the two sets of elements (α and β), Newton iteration is established as:

$$\begin{bmatrix} \mathbf{K}_{aa}^{\alpha} & \mathbf{K}_{ab}^{\alpha} & \mathbf{0} \\ \mathbf{K}_{ba}^{\alpha} & \mathbf{K}_{bb}^{\alpha} + \mathbf{K}_{bb}^{\beta} & \mathbf{K}_{bc}^{\beta} \\ \mathbf{0} & \mathbf{K}_{cb}^{\beta} & \mathbf{K}_{cc}^{\beta} \end{bmatrix} \cdot \begin{Bmatrix} \Delta\mathbf{u}_a \\ \Delta\mathbf{u}_b \\ \Delta\mathbf{u}_c \end{Bmatrix} = \begin{Bmatrix} -\mathbf{r}_a\left(\mathbf{u}_a, \mathbf{u}_b\right) \\ -\mathbf{r}_b\left(\mathbf{u}_a, \mathbf{u}_b, \mathbf{u}_c\right) \\ -\mathbf{r}_c\left(\mathbf{u}_b, \mathbf{u}_c\right) \end{Bmatrix} \tag{4.4}$$

where $\mathbf{K}$ represents the stiffness matrix, $\Delta\mathbf{u}$ is the nodal displacement and $\mathbf{r}_a, \mathbf{r}_b$ and $\mathbf{r}_c$ are the residual vectors for each one of the node sets.

And so, static condensation can be performed, resulting in a reduced system graphically and numerically represented in Figure 4.3 and equation (4.5), respectively:

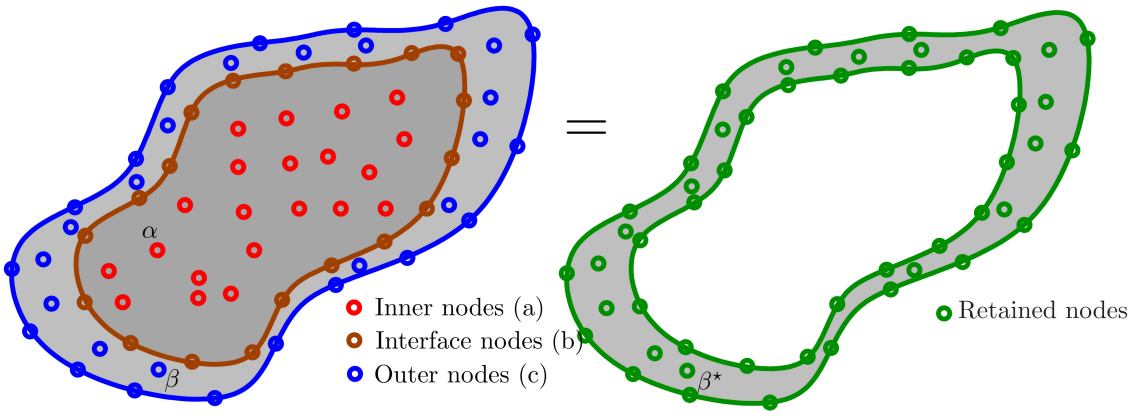

Figure 4.3: Static condensation of a generic body.

$$\left[\begin{array}{c|c} \boxed{\mathbf{K}_{bb}^{\beta}} + \underbrace{\left(\mathbf{K}_{bb}^{\alpha} - \mathbf{K}_{ba}^{\alpha} \cdot \mathbf{K}_{aa}^{\alpha^{-1}} \cdot \mathbf{K}_{ab}^{\alpha}\right)}_{\mathbf{K}_{bb}^{\star\alpha}} & \mathbf{K}_{bc}^{\beta} \\ \hline \mathbf{K}_{cb}^{\beta} & \mathbf{K}_{cc}^{\beta} \end{array}\right] \cdot \begin{Bmatrix} \Delta\mathbf{u}_b \\ \Delta\mathbf{u}_c \end{Bmatrix} = \begin{Bmatrix} \dfrac{-\mathbf{r}_b^{\beta}\left(\mathbf{u}_b, \mathbf{u}_c\right) - \mathbf{K}_{bb}^{\star\alpha} \cdot \mathbf{u}_b}{-\mathbf{r}_c^{\beta}\left(\mathbf{u}_b, \mathbf{u}_c\right)} \end{Bmatrix} \tag{4.5}$$

in which, the term $\mathbf{u}_b$ represents a vector of interface DoFs. It is important to note that the term $\mathbf{K}_{bb}^{\beta}$ in (4.5) is not included in the first determination of the global stiffness matrix.

Rotational Neutralization

When dealing with a nonlinear case, although constant when considering the local reference frame, the stiffness matrix $\mathbf{K}_{bb}^{\star\alpha}$ and residual force $\mathbf{r}_b^{\star\alpha}$ are affected by rotation when the global reference frame is considered. Therefore, rotational neutralization is necessary.

Static condensation is performed once at instant $t = 0$ and the condensed-out stiffness matrix is defined as:

$$\mathbf{K}_{bb}^{\star\alpha} = \mathbf{K}_{bb}^{\alpha} - \mathbf{K}_{ba}^{\alpha} \cdot \mathbf{K}_{aa}^{\alpha^{-1}} \cdot \mathbf{K}_{ab}^{\alpha} \tag{4.6}$$

The corresponding residual force is calculated as follows:

$$\mathbf{r}_b^{\star\alpha} = \mathbf{K}_{bb}^{\star\alpha} \cdot \mathbf{u}_b$$

Considering a local reference frame $\mathbf{T}_l$ and a global reference frame $\mathbf{T}_g$, for a generic time t, the rotation matrix between reference frames is given by:

$$\mathbf{R}_{lg} = \mathbf{T}_l^T \cdot \mathbf{T}_g \tag{4.7}$$

in which $\mathbf{R}_{lg}$ is a block diagonal matrix:

$$\mathbf{R}_{0t} = \begin{bmatrix} \mathbf{R} & \mathbf{0} & \cdots & \mathbf{0} \\ \mathbf{0} & \mathbf{R} & \cdots & \mathbf{0} \\ \vdots & \vdots & \ddots & \mathbf{0} \\ \mathbf{0} & \mathbf{0} & \mathbf{0} & \mathbf{R} \end{bmatrix} \tag{4.8}$$

Consequently, the rotationally neutralized residual force is given by

$$\mathbf{r}_b^{\star t\alpha} = \mathbf{R}_{lg}^T \cdot \mathbf{r}_b^{\star\alpha} = \mathbf{R}_{lg}^T \cdot \mathbf{K}_{bb}^{\star\alpha} \cdot \mathbf{u}_b \tag{4.9}$$

Similarly, the rotationally neutralized displacement degrees-of-freedom are written as:

$$\mathbf{u}_b^t = \mathbf{R}_{lg}^T \cdot \mathbf{u}_b \tag{4.10}$$

and, therefore,

$$\mathbf{r}_b^{\star t\alpha} = \mathbf{R}_{lg}^T \cdot \mathbf{K}_{bb}^{\star\alpha} \cdot \mathbf{R}_{lg} \cdot \mathbf{u}_b^t \tag{4.11}$$

The system Jacobian is the derivative of $\mathbf{r}_b^{\star t\alpha}$ with respect to $\mathbf{u}_b^t$ and is calculated as follows

$$[\mathbf{J}_{bb}^{\alpha}]_{kl} = \frac{\partial}{\partial [\mathbf{u}_b^t]_l} \left[\mathbf{r}_b^{\star t\alpha}\right]_k \tag{4.12}$$

in more detail using index notation,

$$\begin{aligned} [\mathbf{J}_{bb}^{\alpha}]_{kl} = & \left[\mathbf{R}_{lg}^T \cdot \mathbf{K}_{bb}^{\star\alpha} \cdot \mathbf{R}_{lg}\right]_{kl} \\ & + \left\{\mathbf{R}_{lg}^T \left[\mathbf{u}_b^t\right]_l\right\} \cdot \left[\mathbf{K}_{bb}^{\star\alpha} \cdot \mathbf{R}_{lg} \cdot \mathbf{u}_b^t\right]_k \\ & + \left[\mathbf{R}_{lg}^T \cdot \mathbf{K}_{bb}^{\star\alpha} \cdot \left\{\mathbf{R}_{lg} \left[\mathbf{u}_b^t\right]_l\right\} \cdot \mathbf{u}_b^t\right]_k \end{aligned} \tag{4.13}$$

Finally, when this result is added to equation (4.5) in the place of $\mathbf{K}_{bb}^{\star\alpha}$, the system's rotation become neutralized.

4.2.2 Contact Detection through ADF

Once all the preprocessing steps are complete, the *Matlab* simulation is initiated. Once inside *Matlab's* contact module, the position of the secondary body's points are expressed in the main body's local coordinates and *SimPlas* is called as an executable file.

The first operation performed by *SimPlas* is contact detection. Through a computational technique called bucket sorting, *SimPlas* organizes the points associated with the secondary body in terms of its location in space. Once the points are sorted, the software starts to go through them and determines if they have penetrated the main body's surface, in other words, if contact has occurred. This operation is associated with an approximate distance function (ADF), which is presented next.

Approximate Distance Function (ADF)

An approximate distance function is a computational method used to estimate or approximate the distance between two points in a space. ADFs allow for faster calculations and are a more efficient solution than algorithms that heavily rely on computational geometry. Naturally, this improved efficiency comes with a potential loss of accuracy compared to exact distance methods.

The ADF considered in this present work follows closely the one proposed by Areias et al. [60]. Let Ω be the deformed configuration of a generic body and Γ its boundaries. An arbitrary point with coordinates $\mathbf{x}_I$ is also considered and a potential function $\phi(\mathbf{x}_I)$, which is the solution of a scalar partial differential equation (PDE). Once the necessary definitions are established, it is possible to introduce the gap function as a differentiable function $g[\phi(\mathbf{x}_I)]$:

$$g[\phi(\mathbf{x}_I)] = \begin{cases} < 0 & \mathbf{x}_I \in \Omega \\ = 0 & \mathbf{x}_I \in \Gamma \\ > 0 & \mathbf{x}_I \notin \Omega \cup \Gamma \end{cases} . \tag{4.14}$$

Assuming that an unique normal $\mathbf{n}(\mathbf{x}_I)$ exists when $\mathbf{x}_I \in \Gamma$, the gradient of $g[\phi(\mathbf{x}_I)]$ can be decomposed into parallel $(\|)$ and orthogonal $(\perp)$ terms:

$$\nabla g[\phi(\mathbf{x}_I)] = \nabla g[\phi(\mathbf{x}_I)]_{\|} + \nabla g[\phi(\mathbf{x}_I)]_{\perp} \tag{4.15}$$

with $\nabla g[\phi(\mathbf{x}_I)]_{\perp} \parallel \mathbf{n}(\mathbf{x}_I)$.

The normal contact force component is identified as f_c and contact conditions correspond to the following complementary conditions:

$$\begin{cases} g[\phi(\mathbf{x}_I)] \cdot f_c = 0 \\ f_c = 0 \\ g[\phi(\mathbf{x}_I)] = 0 \end{cases} . \tag{4.16}$$

By substituting the generic point with coordinates $\mathbf{x}_I$ for the points associated with the secondary

body, it becomes clear how *SimPlas* obtains the respective contact forces.

The vector form of the contact force is given by:

$$\mathbf{f}_c = f_c \nabla g[\phi(\mathbf{x}_I)] = \kappa \; min\{0, g[\phi(\mathbf{x}_I)]\}^2 \nabla g[\phi(\mathbf{x}_I)] \qquad (\kappa > 0) \tag{4.17}$$

with κ as a penalty parameter for the Courant-Beltrami function. The interested reader is directed to the work by Courant [61] and Beltrami [62].

Considering the screened Poisson equation:

$$\begin{cases} c_L \nabla^2 \phi(x) - \phi(x) = 0 \;\; in \; \Omega \\ \phi(x) = 1 \;\; on \; \Gamma \end{cases} . \tag{4.18}$$

Varadhan [63] states that its solution produces an ADF given by $-c_L log[\phi(x)]$. Finally, the exact distance is obtained as the limit:

$$d(x) = - lim_{c_L \to 0} \;\; c_L log[\phi(x)] \tag{4.19}$$

In this chapter, a brief overview of the used FEM formulation was provided, with special focus on the specific computational techniques used in the developed contact model. *SimPlas* is a vast and complete software and, therefore, its description in full falls outside of this present work's scope. The same applies for the finite element method. The information provided suffices for the understanding of the work developed. However, if a deeper explanation should be required, the interest reader is directed to Bonet et al. [64].

Chapter 5

Co-simulation of Bouncing Ball Problem

This section is dedicated to the implementation and theoretical validation of the developed contact model, presented in the previous section.

Firstly, the bouncing ball example is used for the validation of the implemented contact module based on Flores' formulation, through the comparison of the obtained results with the ones shown in Flores et al. [51]. The implementation of Flores' model served as an introductory step before advancing into the innovative contact module. It allowed for a better understanding of some of the obstacles associated with the chosen methodology, namely the comprehension of some contact related concepts, familiarization with the Matlab code and the selection of the integrator.

The results obtained using Flores' model were used as reference in validating the previously described continuum contact model associated with a co-simulation methodology.

For a better and more complete comparison of the results obtained, the characteristics chosen for the bouncing ball example were kept the same as the ones used in Flores et al. [51]. Therefore, it was considered that an elastic ball made of PTFE and $1\ kg$ of mass is dropped from an initial height of $1\ m$. The ball has a radius of $0.1\ m$, a moment of inertia of $0.1\ kg\ m^2$ and a equivalent stiffness equal to $140 \times 10^6 N/m^{\frac{3}{2}}$. The ball is released from the initial position under the action of gravity only, falling until it collides with the ground, which is considered rigid and stationary. Upon contact with the ground, the ball rebounds to a certain height, depending on the chosen coefficient of restitution.

5.1 Application of Flores' Contact Model

The first contact model to be implemented in the *Matlab* software's contact module was the one proposed by Flores et al. [51]. As observed in equation (2.7), in order to determine the contact force correspondent to a specific moment, it is necessary to know the relative normal deformation between the contacting bodies (δ) and the relative normal contact velocity, not only at the current instant ($\dot{\delta}$), but also right before contact begins ($\dot{\delta}^{(-)}$).

In order to test the implementation of this contact model, the classical bouncing ball problem was chosen. Therefore, the contact between a sphere and a plane was simulated. For a better understanding of the problem's formulation, Figure 5.1 is presented next, followed by a detailed explanation of how contact detection occurs.

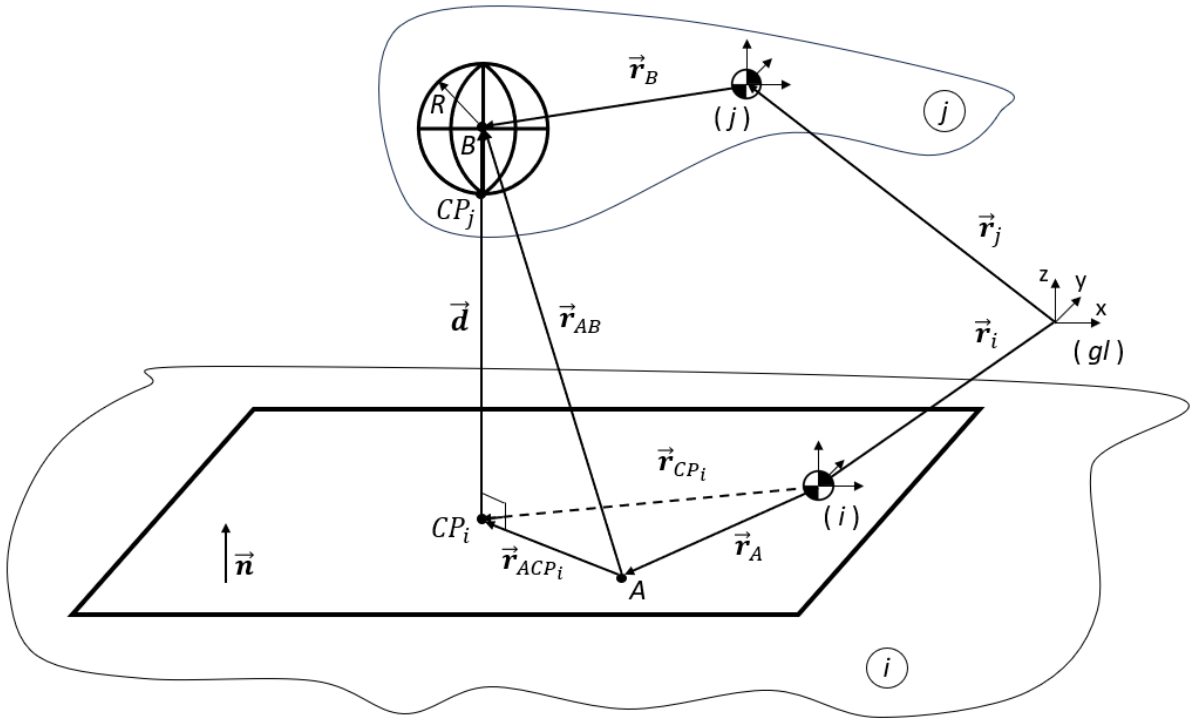

Figure 5.1: Bouncing ball example.

From Figure 5.1 it is possible to observe that the contact problem being studied occurs between two geometries (one plane and one sphere), each associated with a different generic body (body *i* and body *j*, respectively). A generic body can be associated to multiple contact geometries and its center of mass (CoM) can be located outside these geometries, as represented in Figure 5.1 by its international symbol, the sectioned circle. However, for the purpose of simplicity, in the following examples associated with the bouncing ball problem, the center of the geometries was defined as the CoM of the respective body. Each body has its own local reference frame, that can be distinct from the global reference frame of the problem. Additionally, a random point that belongs to the plane (point *A*) is selected to, along with the normal vector of the plane (vector $\mathbf{n}$), to characterize the plane's position and orientation. It is important to note that in the way this example is set up, the contact occurs between only two points: the contact point at the base of the sphere (CP_j) and the contact point in the plane directly below the first one (CP_i). Therefore, the total contact force of each one of the bodies is applied in a single point.

When using this contact model, contact occurs when the relative deformation between the contacting bodies is positive ($\delta > 0$). In order to determine the relative deformation between the contacting bodies (δ), it is necessary to know the sphere's radius (R) and subtract from it the norm of vector $\mathbf{d}$, as follows:

$$\delta = R - ||\mathsf{d}|| \tag{5.1}$$

As one can observe in Figure 5.1, vector $\mathbf{d}$ is obtained from the dot product between the vector between points *A* and point *B* ($\mathbf{r}_{AB}$), and the plane's normal vector ($\mathbf{n}$):

$$\mathbf{d} = \mathbf{r}_{AB}^T \cdot \mathbf{n} \tag{5.2}$$

with

$$\mathbf{r}_{AB} = \mathbf{r}_B - \mathbf{r}_A \tag{5.3}$$

where $\mathbf{r}_B$ and $\mathbf{r}_A$ represent the global position vectors of point *B* and point *A*, respectively. It is important to note that, when detecting contact while using this model, the points and vectors used should be associated with the global reference frame and, therefore, they should be obtained from their local equivalent by using equations (3.18) and (3.24):

$$\mathbf{r}_B = \mathbf{C}_j^B \mathbf{q}_j \tag{5.4}$$

$$\mathbf{r}_A = \mathbf{C}_i^A \mathbf{q}_i \tag{5.5}$$

$$\mathbf{n} = \mathbf{C}_i^{\mathbf{n}} \mathbf{q}_i \tag{5.6}$$

When determining the relative normal contact velocity ($\dot{\delta}$), one has to calculate the time derivative of vector $\mathbf{d}$, as follows:

$$\dot{\delta} = -\dot{\mathbf{d}} = (\dot{\mathbf{r}}_{AB}^T \cdot \mathbf{n} + \mathbf{r}_{AB}^T \cdot \dot{\mathbf{n}}) \tag{5.7}$$

with

$$\dot{\mathsf{n}} = \mathbf{C}_i^{\mathbf{n}} \dot{\mathbf{q}}_i \tag{5.8}$$

With all the required variables defined, the contact force ($\mathbf{F}_C$) can be determined and applied to both bodies. The force value obtained from equation (2.7) is multiplied by the planes' normal vector ($\mathbf{n}$) and, naturally, the force applied to body *i* must be symmetrical to the one applied to body *j*:

$$\mathbf{F}_C^i = -F \cdot \mathbf{n} \tag{5.9}$$

$$\mathbf{F}_C^j = F \cdot \mathbf{n} \tag{5.10}$$

Finally, these concentrated contact forces need to be transformed into their generalized equivalents

equation, using equation (3.27), so they can be added to the vector of generalized forces ($\mathbf{g}$):

$$\mathbf{g}_i^{\mathbf{F}_C^i} = \mathbf{C}_i^{CP_i^T} \mathbf{F}_\mathbf{C}^\mathbf{i} \tag{5.11}$$

$$\mathbf{g}_j^{\mathbf{F}_C^j} = \mathbf{C}_j^{CP_j^T} \mathbf{F}_\mathbf{C}^\mathbf{j} \tag{5.12}$$

where CP_i and CP_j represent the contact points in bodies *i* and *j*, respectively.

In similarity to the methodology followed in Flores et al. [51], five different simulations were considered, in which the coefficient of restitution was set as $cr = 1$, $cr = 0.8$, $cr = 0.6$, $cr = 0.4$ and $cr = 0.2$; and the exponent n was considered to be 1.5. The impact of these variations was studied in regards to: the ball deformation (Figure 5.2), the ball deformation velocity (Figure 5.3) and the contact force (Figures 5.4 and 5.5). These results are presented next and are associated with the contact period that characterizes the first bounce.

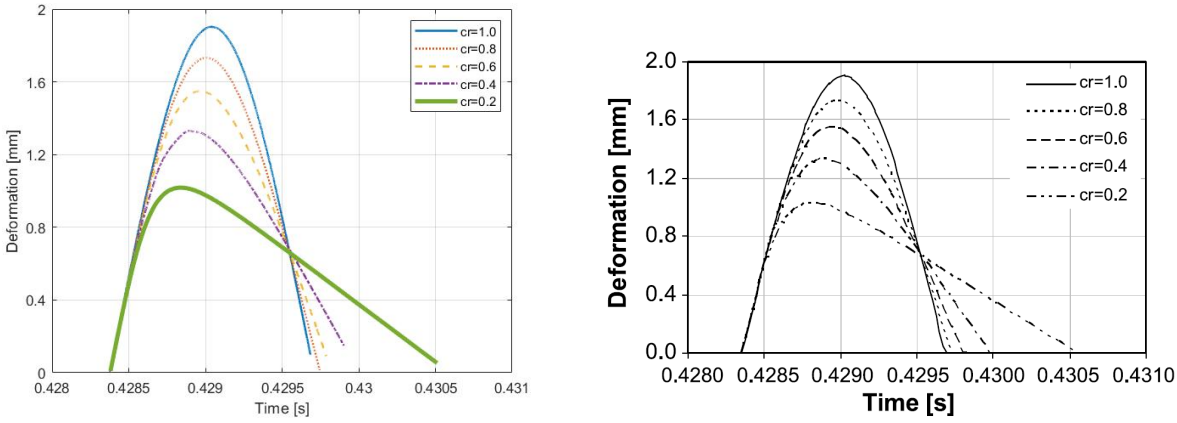

(a) (b)

Figure 5.2: Influence of the coefficient of restitution on ball deformation through time: implemented contact model (a); Flores et al. [51] (b).

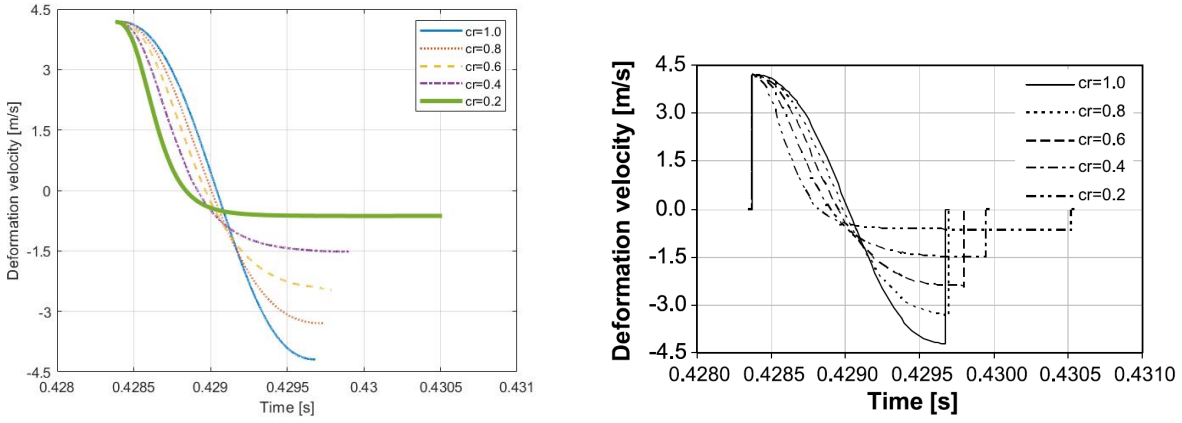

(a) (b)

Figure 5.3: Influence of the coefficient of restitution on ball deformation velocity through time: implemented contact model (a); Flores et al. [51] (b).

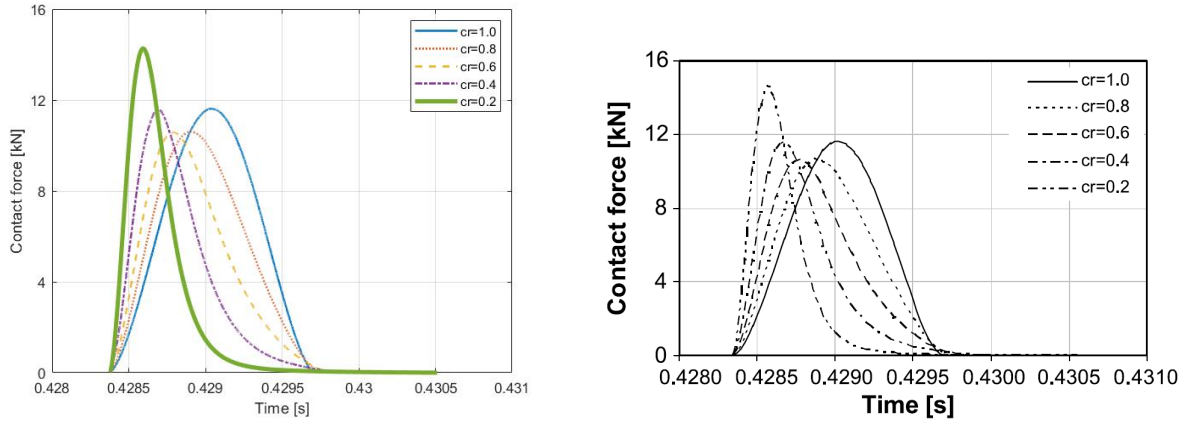

Figure 5.4: Influence of the coefficient of restitution on contact force through time: implemented contact model (a); Flores et al. [51] (b).

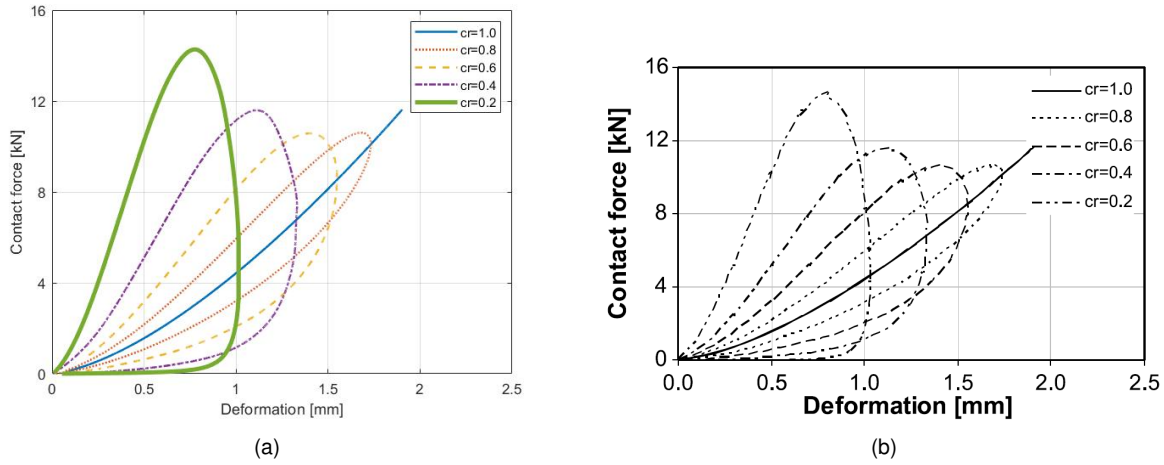

Figure 5.5: Influence of the coefficient of restitution on contact force versus ball deformation: implemented contact model (a); Flores et al. [51] (b).

From a quick observation of all four figures, it is clear that the results obtained from the implemented contact module are identical to the ones proposed by Flores et al. [51]. However, it is important to analyze in greater detail each one of the figures, not only to understand the influence of the coefficient of restitution on contact situations, but also to understand what happens during the contact phenomena.

In Figure 5.2, it is possible to observe that, as the coefficient of restitution is reduced, the maximum value for the ball deformation is also reduced, while the contact duration is increased. A reduction in the coefficient of restitution leads to an increase in the structural damping of the material, also known as hysteresis damping, and, consequently, a loss of energy after contact. This results, not only in less energy associated with the deformation of the ball, but also in less structural reaction in restituting its original shape, which leads to a longer contact period.

Focusing now on Figure 5.3, it is possible to conclude that during the compression phase, the deformation velocity is positive (deformation is increasing) and it decreases until it reaches zero, moment at which maximum deformation is reached. After that, during the restitution phase, there is a change in direction of the deformation velocity as the ball begins to return to its original form. It is clear that when

varying the coefficient of restitution, although the value of the deformation velocity right before impact with the ground remains the same, its value at the end differs. The first observation can be justified by the fact that the same characteristics are kept for all cases and the ball is initially dropped under the action of gravity only, resulting in the impact of the coefficient of restitution only being felt once contact is initiated. The second observation is related to the fact that for higher coefficients of restitution, less energy is lost during contact and, consequently, the ball tends to more closely restore the conditions at which it initiated the contact. In this case, the velocity at which the ball leaves the ground after contact tends to be closer to the one at which it reaches the ground (but with opposite signs), for higher coefficients of restitution. It is also interesting to note that, for smaller coefficients of restitution and, therefore, greater losses of energy during contact, the deceleration is greater and the null velocity is reached more quickly.

Moving on to Figure 5.4, it is noticeable that higher maximum values for the contact force are associated with lower coefficients of restitution, with the exception of $cr = 1$, and that the moment at which this maximum is registered coincides with the moment of maximum deformation and null deformation velocity.

Finally, from Figure 5.5 one can observe that a decrease in the value of the coefficient of restitution results in a increase of the hysteresis loop, which is directly associated with the energy lost during contact. This is particularly clear for $cr = 1$, which corresponds to the pure Hertz' contact law, and in which, because there is no energy dissipation, the hysteresis loop is absent.

As a consequence of the very high resemblance between the obtained results and the ones proposed by Flores et al. [51], the implemented contact module based on the Flores' contact model is considered validated.

5.2 Application of the Co-simulation Contact Model

Moving on to the application of the continuum contact model developed in the context of this work, a different formulation had to be applied to the bouncing ball problem and, consequently, Figure 5.1 had to suffer some changes (see Figure 5.6). It is worth highlighting that the physical data chosen for the problem was kept the same as in the Flores' application case. The contact example is still between a sphere and a plane that belong, respectively, to a generic body *j* and a body *i*. From *SimPlas'* perspective, body *j* is considered to be the main body and body *i* is associated with the role of secondary body. This means that *SimPlas* assumes that the sphere is still and the points that compose the plane move up and down, penetrating the sphere's surface.

By observing Figure 5.6, it is necessary to conciliate the two different approaches that the *Matlab* multibody code and *SimPlas* have of the same problem.

On the one hand, from the multibody side's perspective, there are two bodies: bodies *i* and *j*. Body *i* represents the floor as a plane and is, therefore, still. Body *j* represents the ball as a sphere, which moves vertically, colliding with body *i* and bouncing up and down. On the other hand, inside *SimPlas*, there is a main body, which in this present case is the ball, that is still. A secondary body that represents

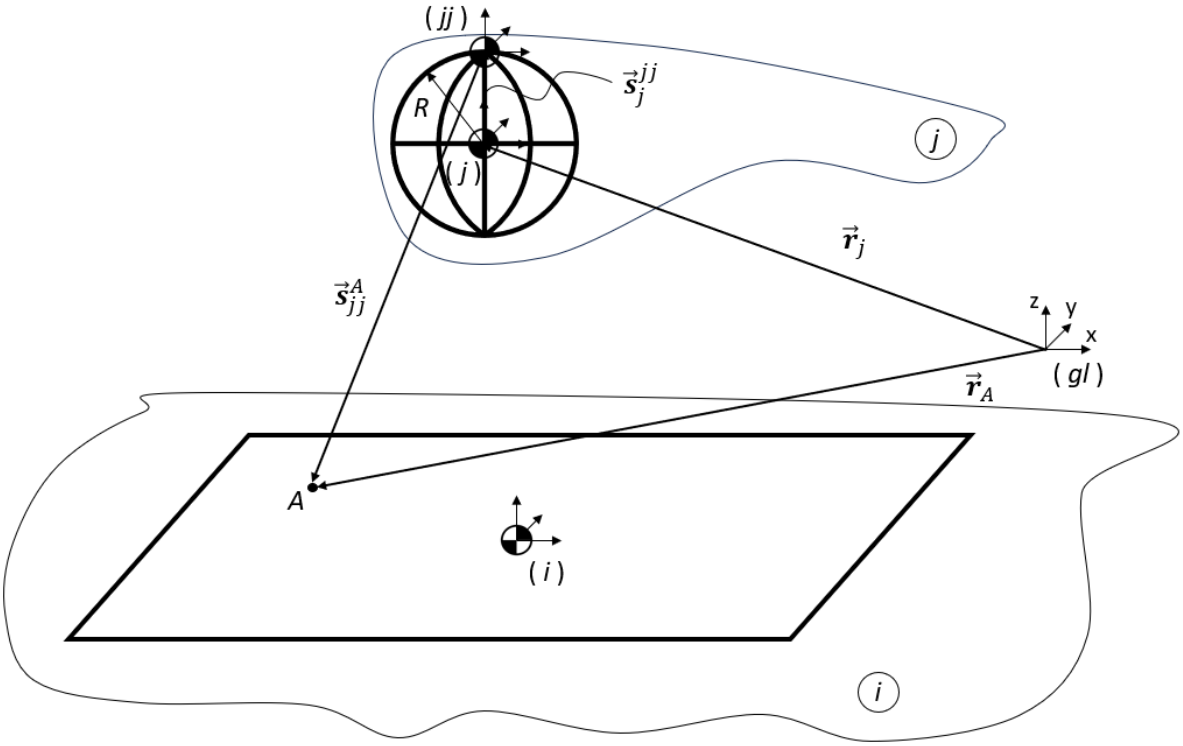

Figure 5.6: Bouncing ball example (*SimPlas*).

the ground is composed by a group of points that travel up and down, and interact with the main body. Although the decision of having these opposite perspectives ended up not being relevant in this particular problem, it will be justified in more practical applications discussed in the next chapter.

Since the following explanation is associated with multiple reference frames, it is important to first clearly identify them: the global reference frame is identified as (*gl*); the local reference frame associated with the sphere, which has its origin located in the body's CoM, is identified as (*j*); the second local reference frame associated with the sphere, which has its origin on the top point of the body and is the one considered by SimPlas, is identified as (*jj*); and, finally, the local reference frame associated with the plane, which has its origin located in the body's CoM, is identified as (*i*).

Now that the relevant nomenclature of Figure 5.6 has been established, a detailed deduction of the process to obtain the coordinates of a generic point A (in this case, a point that belongs to body *i*) expressed in the coordinates of the reference frame (*jj*) is presented. Starting by considering a closed vector loop, it is possible to write:

$$\mathbf{r}_j + \mathbf{s}_j^{jj} + \mathbf{s}_{jj}^{A} - \mathbf{r}_A = \mathbf{0} \tag{5.13}$$

or alternatively,

$$\mathbf{r}_A = \mathbf{r}_j + \mathbf{s}_j^{jj} + \mathbf{s}_{jj}^{A} \tag{5.14}$$

in which $\mathbf{r}_A$ refers to the global position vector of point A; $\mathbf{r}_j$ is associated with the global position vector

of the origin point of reference frame (*j*); $\mathbf{s}_j^{jj}$ represents the vector that goes from the origin point of the reference frame (*j*) to the origin point of the reference frame (*jj*), expressed in global coordinates; and $\mathbf{s}_{jj}^{A}$ is the vector that goes from the origin point of the reference frame (*jj*) to point A, expressed in global coordinates.

Equation (5.14) can be expanded by writing vectors $\mathbf{s}_j^{jj}$ and $\mathbf{s}_{jj}^{A}$ in the local coordinates of the reference frames (*j*) and (*jj*), respectively. Vectors expressed in the local coordinate system of reference frame (*j*) will be associated with the subscript ', while the ones expressed in the local coordinate system of reference frame (*jj*) will be associated with the subscript ". Therefore, equation (5.14) becomes:

$$\mathbf{r}_A = \mathbf{r}_j + \mathbf{A}_j \mathbf{s}_j^{jj'} + \mathbf{A}_{jj} \mathbf{s}_{jj}^{A''} \tag{5.15}$$

with $\mathbf{A}_j$ as the transformation matrix between the global reference frame and the reference frame (*j*); and $\mathbf{A}_{jj}$ as the transformation matrix between the global reference frame and the reference frame (*jj*).

Matrix $\mathbf{A}_{jj}$ can be expressed as:

$$\mathbf{A}_{jj} = \mathbf{A}_j \mathbf{A}_{jj'} \tag{5.16}$$

in which $\mathbf{A}_{jj'}$ represents the matrix that transforms the coordinates of a vector expressed in the local coordinates of reference frame (*jj*) in a vector expressed in the local coordinates of reference frame (*j*).

Consequently, equation (5.15), when solved for $\mathbf{s}_{jj}^{A''}$ becomes:

$$\mathbf{s}_{jj}^{A''} = \mathbf{A}_{jj'}^{T} (\mathbf{A}_j^{T} (\mathbf{r}_A - \mathbf{r}_j) - \mathbf{s}_j^{jj'}) \tag{5.17}$$

The final required step for obtaining the position of the points associated with body *i*, expressed in the local coordinates of reference frame (*jj*), is to define the constant vector $\mathbf{s}_j^{jj'}$. This vector expresses the location of the origin point of reference frame (*jj*) in the local coordinates of reference frame (*j*). On the one hand, as previously mentioned, the CoM of body *j* and, consequently, the origin point of reference frame (*j*), are coincident with the center of the sphere geometry. On the other hand, the origin point of reference frame (*jj*) was defined as the top point of body *j*. This results in:

$$\mathbf{s}_j^{jj'} = \begin{bmatrix} 0 & 0 & R \end{bmatrix} \tag{5.18}$$

in which R represents the radius of the body *j*.

With the determination of $\mathbf{s}_{jj}^{A''}$, the *Matlab* program is ready to provide this information to SimPlas and receive in return the corresponding contact forces, if contact detection occurs.

Before the co-simulation of the contact between a 3D sphere and a plane, using a forward dynamics approach, a simpler case was considered using a cylinder, in which each node only had two DoFs instead of three. The same bouncing ball problem was considered and the exact formulation previously presented was followed. This simplification allowed for quicker simulations while the focus was on establishing the communication between the two programs, performing debug procedures on both software codes and assessing the benefits and implications of some computational techniques used. The inter-

mediate studies performed on understanding the behavior of the integrator, the computational efficiency gained from performing static condensation and the results' sensitivity to the penalty parameter used are presented next.

5.2.1 Integrator Behavior on Stiff Problems

When considering a multibody system in which contact is being simulated using a forward dynamics' formulation, the problem needs to be analyzed as a stiff problem. A stiff problem is a problem described by a set of stiff ordinary differential equations. The stiffness of a set of equations is as greater as how much time-constants differ in the problem to be analyzed. Time-constants are associated with the rate of decay, which in turn, are related to the eigenvalues of the system's Jacobian matrix. If within the problem at hands, some of the decay rates are slow and others are fast, the last ones will dictate the stability of the numerical method used to solve the system of equations [65]. In other words, an ordinary differential equation problem is considered stiff if at certain time periods, the solution varies slowly while in others it varies with high frequencies. This is relevant in terms of computational efficiency. If the size of the time step used to solve the problem can be adjusted to how much the solution is varying, the CPU time can be greatly minimized.

In order to depict the change in the size of the time step throughout a contact event, the vertical position of the CoM of a cylinder throughout all the integration steps, in the conditions of the bouncing ball problem, is presented in Figure 5.7.

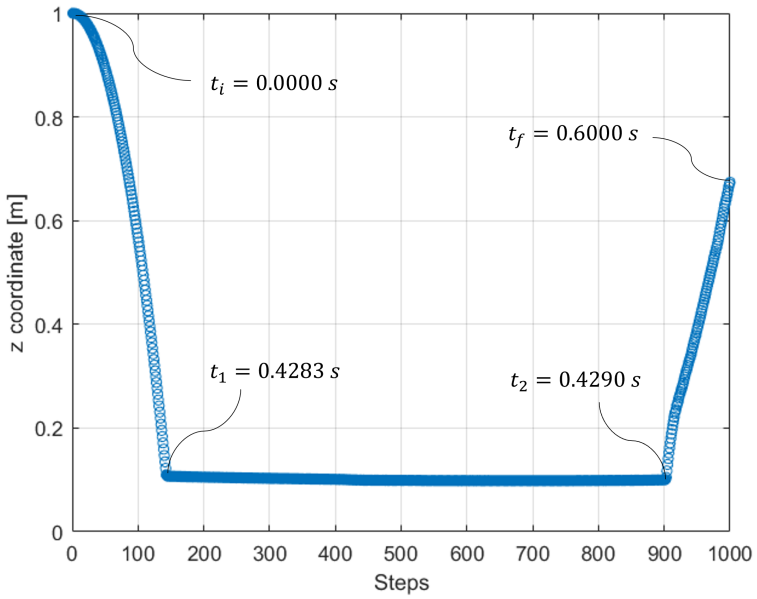

Figure 5.7: Position of cylinder CoM during contact event.

In the case of a multibody system, while the bodies are not in contact, the solution for the integration of the next time step is very similar to the last one (little variation), and so the size of the time step can confidently be increased without the lost of numerical accuracy. This is depicted in the first 140 integration steps, during which the cylinder is falling only under the application of the gravitational force.

However, when contact occurs, the solution shifts very quickly, and so the time discretization needs to be increased. From step 140 until step 900, the time step considered is so small the plot resembles a continuous line. Once again, as contact ends in step 900, the size of the time step increases and the simulation progresses at a higher pace. From the four times provided associated with the beginning of the simulation (t_i), the beginning of the contact event (t_1), the end of the contact event (t_2) and the end of the simulation (t_f), it is possible to conclude: although the contact event corresponds to 0.12 % of the simulation time, it is associated with 76 % of all integration steps taken. It is important to note that a non-stiff numerical method, with a constant time steps size, would also solve this type of problem, but it would be extremely inefficient. Therefore, when selecting the right integrator for the present problem, its ability to deal with stiff equations is instrumental.

The dynamic analysis of a multibody system presupposes the resolution of the equations of motion, which are a set of ordinary differential equations (ODEs). For this purpose, in the present work, a *Matlab* ODE solver was used. After comparing the available options, ODE23s was selected because it is prepared to solve stiff differential equations by allowing a variable time-step integration. This solver is associated with an implicit integration method based on a predictor-corrector scheme. In the predictor step, an initial estimate of the solution is obtained through a simpler and less accurate numerical integration method. This approximation is used to predict the next value of the function at a small time step. In the corrector step, a more accurate estimate of the solution is determined with a more complex integration method, in order to refine the value obtained in the predictor step. Basically, a predicted value is used to compute a corrected one, becoming closer to the actual solution. This prediction and correction steps occur as part of an iterative process, meaning that the value keeps getting refined until a desired level of accuracy is achieved through a defined tolerance. If this boundary error is achieved within a defined maximum number of iteration steps, the method converges and a true corrector step occurs. Otherwise, a false corrector step is set and the process starts all over again with a smaller time increment from the previous evaluation step.

5.2.2 Static Condensation Impact on Computational Efficiency

In order to assess the benefits of performing static condensation on the models analyzed in this present work and in what conditions it should be considered, simulation times with and without this technique were compared (see Figure 5.8). It was once again considered the cylinder simplification applied to the bouncing ball problem. The times depicted in the results are associated with one contact step and are normalized for the time related to the model without static condensation for the coarser mesh ($t = 0.522\ s$).

Being that *h* represents the element size, it is possible to observe that, for higher values of *h*, and therefore, less refined meshes, models in which static condensation was not applied present higher computational efficiency. However, as the mesh is refined, static condensation starts to justify its use and its computational efficiency increases exponentially when compared to the models in which it was not performed. This is related to the ratio between external and internal nodes. For coarser meshes, this

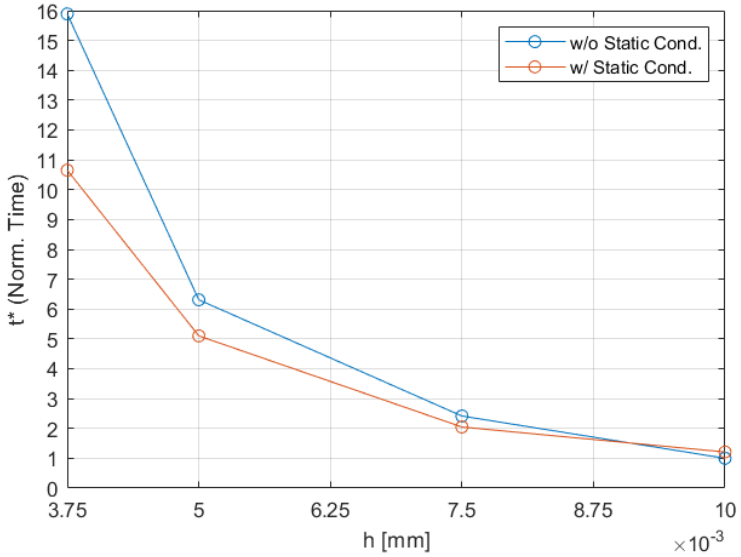

Figure 5.8: Computational efficiency of simulation with and without static condensation.

ratio is smaller and the additional steps associated with performing static condensation do not compensate the reduction in DoFs of the system used in the simulation. However, as the value of h decreases, the initial time spent on performing static condensation becomes less and less relevant when compared to the efficiency it provides during the simulation.

Before presenting the obtained results, it is important to note that, as considered by Flores' contact model, the deformation of the sphere should be measured from its center point (equation (5.1)). Therefore, to simplify the problem to solve, the contact of the sphere was simulated with the use of symmetry planes.

In Figure 5.9, the comparison between contact models is done through the obtained ball deformation throughout the period of time associated with contact.

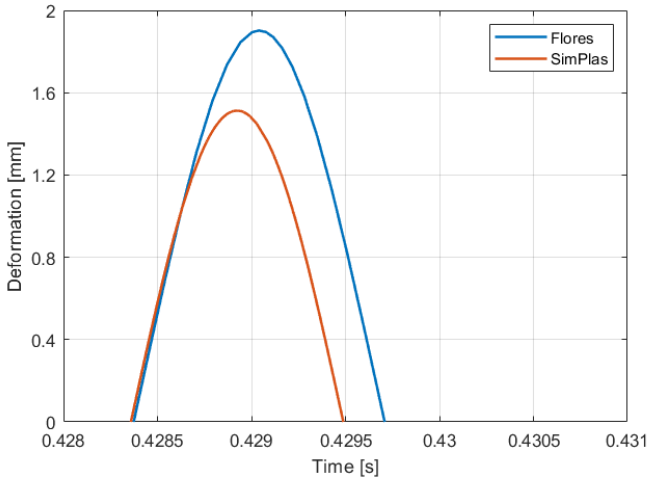

Figure 5.9: Contact model comparison for ball deformation through time.

Although there is some variation between the deformation values associated with both contact mod-

els, this does not result in a variation of contact force values, as depicted in Figure 5.10.

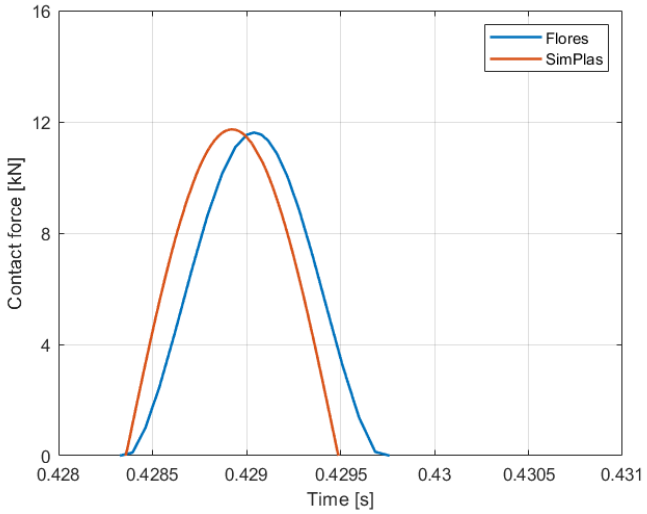

Figure 5.10: Contact model comparison for contact forces through time.

And as a last comparison, Figure 5.11 depicts the relation between the contact force determined and the ball's deformation. As expected, it is possible to observe that the force-deformation relation associated with Flores' model is exponential (in equation (2.7) δ^n, with $n = 1.5$), while SimPlas considers a linear relation.

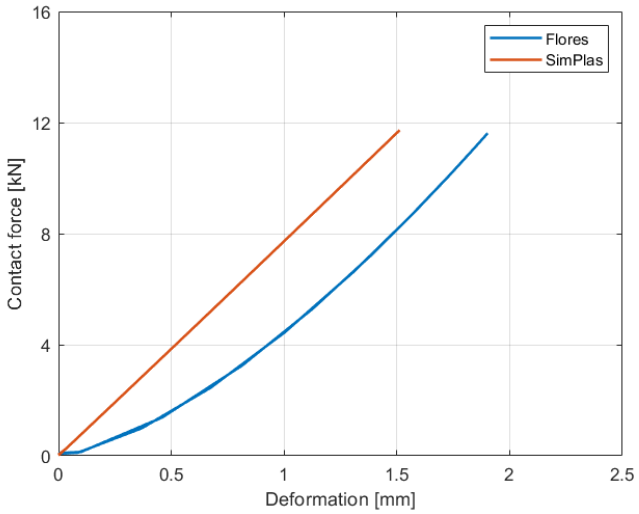

Figure 5.11: Contact model comparison for contact forces versus ball deformation.

Once compared the equivalent results between the two contact models, it is important to highlight the additional data that the implemented co-simulation model provides, allowing for a deeper analysis. These include the local displacement of the points belonging to the sphere during contact (see Figure 5.12), the internal stress values (see Figure 5.13), which are of relevance if the structural design of the sphere is being considered, and the pressure distribution on the contact points (see Figure 5.14). The three figures are associated with the point of maximum deformation and SI units are used.

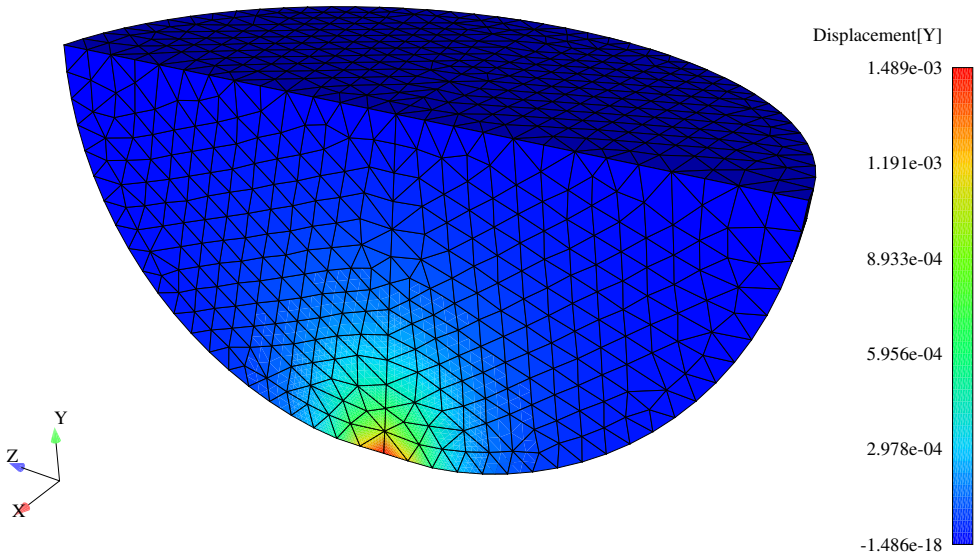

Figure 5.12: Displacement values for maximum ball deformation.

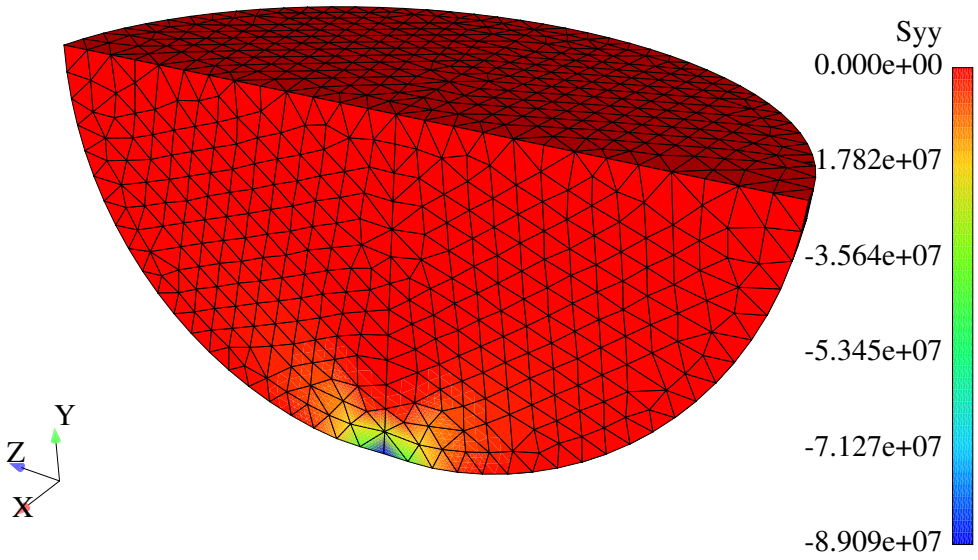

Figure 5.13: Internal stresses distribution and value for maximum ball deformation.

It is important to note that, in the case of comfort analysis (for exoskeletons, for example), the pressure distribution resultant of skin-machine contact is very important. Furthermore, the use of static condensation on the model has no influence on the type of results showcased in Figure 5.14, since only the outside nodes are required. However, if the desired results require the stress values in the interior of the body, static condensation cannot be performed, because in this case the interior nodes are needed for the calculation of the internal stress distribution.

After this presentation of the results associated with the co-simulation methodology implemented for the bouncing ball problem, its application to practical scenarios is finally possible. The next chapter focuses on the application of the developed software to gait analysis.

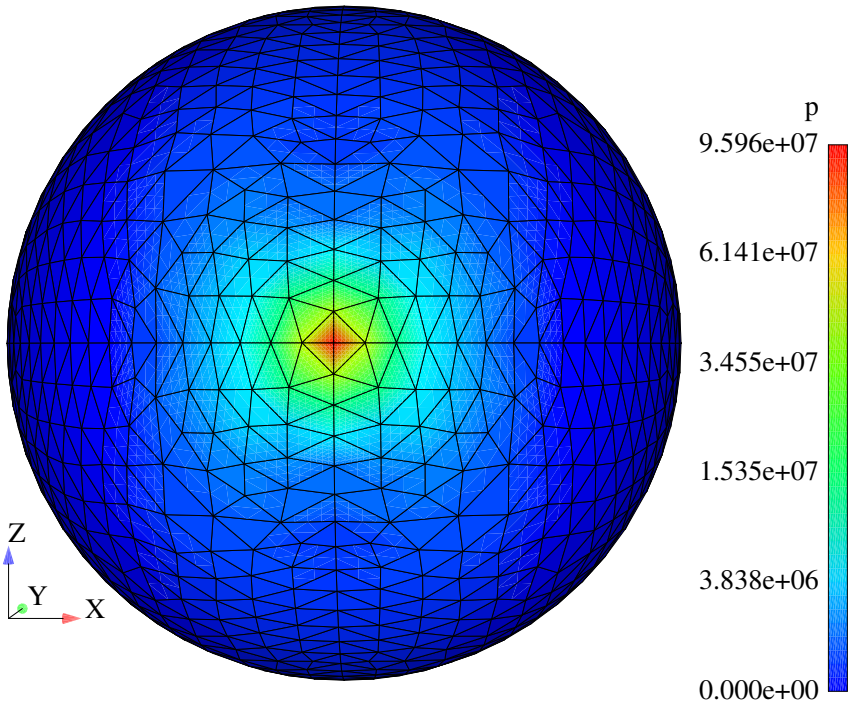

Figure 5.14: Pressure distribution for maximum ball deformation.

Chapter 6

Co-simulation of Foot-Ground Contact

Theoretical simulations are instrumental for validation of software, methodologies or even new models. But once it is established that the tools being used are capable of replicating realistic results that are in accordance to what has already been published in the literature, it is finally possible to push the boundary of progress further by applying what has been developed into producing new data and by tackling practical cases.

This section is dedicated to showcasing the practical applications of the developed co-simulation methodology, considering gait analysis. It starts highlighting the overwhelming similarities and few changes between this new case and the bouncing ball problem, previously described in detail. Next, the foot model used in the simulations and all the simplifications considered are introduced. After that, all the data that was acquired is listed and the respective acquisition procedures are described in depth. Then, it moves onto explaining how said data was used as input for the considered simulations, followed, naturally, by the obtained results.

6.1 Foot Model

When compared to the different foot models previously discussed, the one used in this work is simultaneously more detailed in some aspects, while introducing considerable simplifications in others. On the one hand, it does not represent the foot's geometry as a summation of geometrical shapes, such as spheres and ellipsoids. It has an extremely realistic shape, due to the fact that it was obtained through 3D scanning. A detailed contact surface is instrumental for realistic contact detection between the foot and the ground. On the other hand, in terms of the internal structure and material of the foot, the model presents a simple homogeneous isotropic single material structure, as the definition of an anatomically and physiologically detailed internal foot structure is outside the scope of this work. This means that no distinction was made between the different foot constituents: bones, muscles, tendons, ligaments and skin. The mechanical properties of all these components were represented as realistically as possible in an hypothetical equivalent material. Furthermore, since no bones and joints were considered, the deformability of the foot in a realistic way was partially compromised.

6.2 Experimental Data Acquisition

The data acquired in the scope of the present work refers to a healthy 23 years old male, measuring 181 cm of height, weighing 63.4 kg, and it was all gathered in Lisbon's Biomechanical Laboratory, located at the Department of Mechanical Engineering of Instituto Superior Técnico.

The experimental data acquired are of geometrical, kinematic and kinetic nature, and the associated procedures are described next.

6.2.1 Acquisition of the Foot Geometry

In order to simulate the contact of a human foot with the ground, it is necessary to obtain a virtual representation of said foot. Depending on the desired accuracy of the results and, naturally, the available resources, the foot is often simplified into a combination of geometrical shapes, usually spheres. However, in the present work, a 3D scanner was available, allowing for a much more realistic representation of a human foot. Therefore, the subject´s feet were scanned using an Einscan Pro HD scan (SHINING 3D, Hangzhou, China) (see Figure 6.1). The subject was in the siting position, with their leg placed on top of another chair, leaving the foot to be scanned in a suspended and undeformed state. It is important to note that the development of the foot model was based on the subject's left foot.

Figure 6.1: 3D scanning of human foot.

During the scanning procedure, the 3D scan records the foot's geometry and generates a computer file with a list of point coordinates. This file was exported to a computer program named GID (GID Simulation, Barcelona, Spain), in which the geometry was processed and a mesh was generated.

6.2.2 Static and Dynamic Tests on Pressure Plates

Once the foot geometry was acquired, static and dynamic tests were preformed using pressure plates. The foot scanning system used was composed by one 1.0 x 0.5 m^2 pressure plate by RSscan.

At first, the subject was asked to stand in the standard anatomical position with one foot on each one of the plates. This originated the pressure distribution illustrated in Figure 6.2.

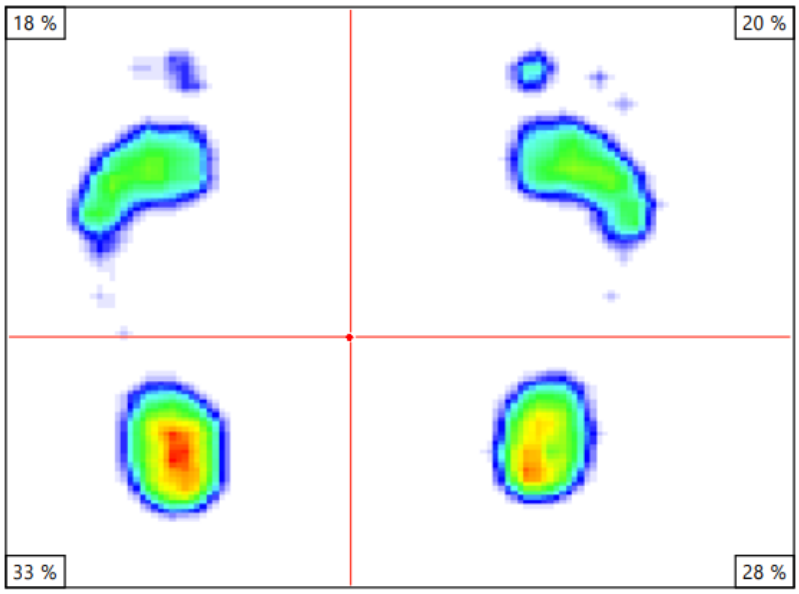

Figure 6.2: Pressure distribution of foot-ground contact during standing position.

After, the subject was asked to take some steps away from the plates, walk towards them, assuring that a single step was recorded for each foot.

6.2.3 Foot Deformation Test on Force Plates

As previously mentioned, as a result of the simplifications applied to the foot model used, a homogeneous and equivalent material had to be characterized in terms of its mechanical properties, namely its Young modulus (E) and Poisson ratio (ν).

In order to determine an equivalent value for the Young modulus, which will be explained in the section dedicated to the preprocessing of the foot model, an experimental test was performed at the laboratory, followed by a trial and error methodology applied during the post-processing of the gathered data.

Firstly, the deformation on the subject's foot between its undeformed and maximum deformed states was measured. This was achieved through a test performed at the laboratory, using one force plate and a motion capture system. The force plate is an AMTI OR 6-7 and the marker-based MOCAP system was composed by 14 Qualisys ProReflex 1000 infrared cameras. As part of the preparation phase of the trial, one reflective marker was placed on each side of the subject's ankle joint and their location was tracked at all times by the surrounding cameras. It is important to note that the position of the ankle joint was

considered to be the mean value between the ones associated with the two markers placed on opposite sides. Furthermore, it is worth highlighting that because of data noise, any force value registered in the force plate that was below 5 N was considered as a null value.

At the beginning of the trial, the subject was positioned in the reference anatomical position, with only his left foot on top of the force plate. After this, the subject began to shift his weight between his feet: one foot would lift up, losing contact with the ground and assuming an undeformed state, while the other one would support the subject's full body weight and, thus, achieving its maximum deformed state. This alternating movement was repeated cyclically. The position of the ankle joint and the ground reaction forces felt in the force plate were recorded simultaneously, and the data collected associated with the z coordinate is presented in Figures 6.3 and 6.4, respectively.

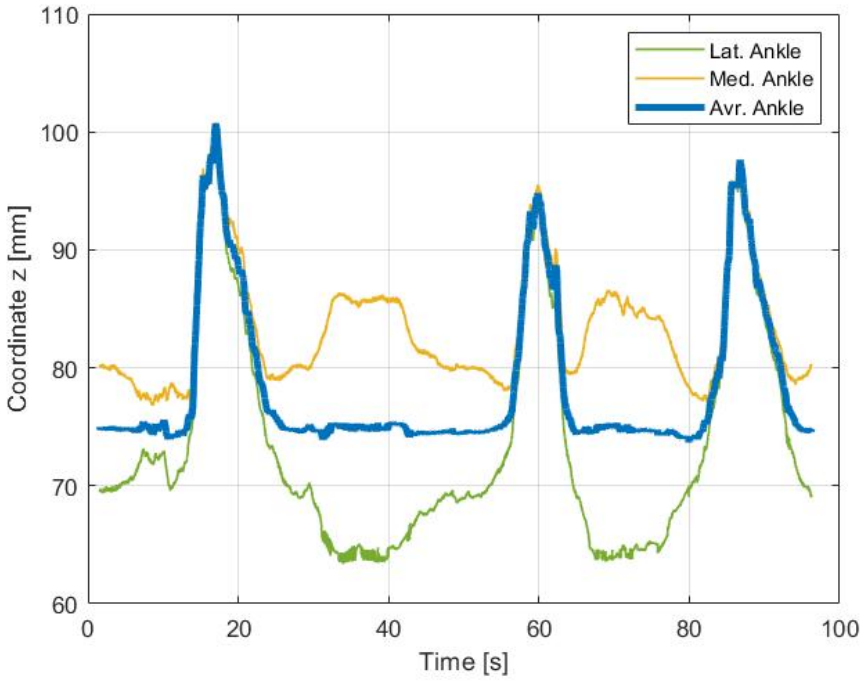

Figure 6.3: Ankle position (coordinate z) during deformation test.

By analyzing Figure 6.4, it is possible to determine the moments in which the foot initiates contact with the ground (recorded force close to zero) and the moments in which the subject is fully supported by his left foot (recorded force at maximum value). Once these moments are identified, and since the recording of the two types of data was synchronized, one can determine the corresponding position of the ankle joint at those moments. The displacement of the ankle joint within each cycle provides the amplitude of deformation of the human foot.

By considering the two recorded cycles of the movement, an average value was calculated and, thus, the final results are: $\Delta z = 8.8\ mm$ and $F_{máx} = 622\ N$. This means during the one support phase of gait, when the subject has its full body weight over one foot, the foot deforms around $8.8\ mm$.

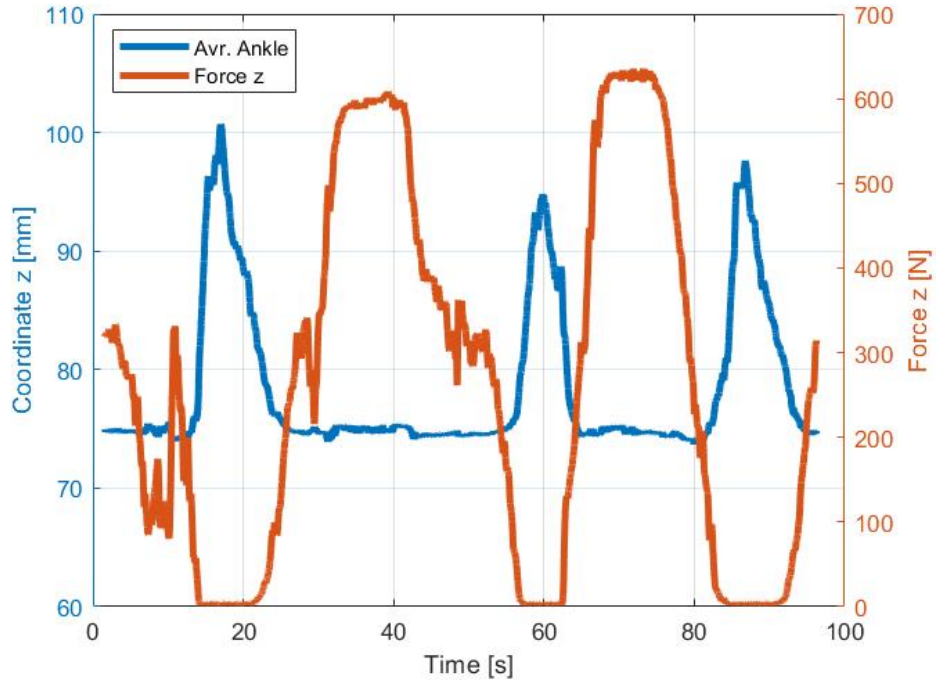

Figure 6.4: Ground reaction forces (vertical component) and ankle displacement during deformation test.

6.2.4 Kinematics and Dynamics of a Gait Cycle

For the final data acquisition procedure performed, the kinematic and kinetic behavior of the subject's foot, ankle, leg and knee during gait were obtained. Three force plates and the motion capture system were used.

Once again, as part of the preparation phase of the trial, reflective markers were placed in key location in accordance with the market set protocol adopted by the gait lab (see Figure 6.5).

Once all the conditions were gathered for the initiation of the trial, the subject was asked to walk on top of three force plates, which were laid out as illustrated in Figure 6.6. The subject was instructed to step with only one foot on each of the force plates, starting always with his right foot. Therefore, the data used in this work was associated with the second force plate, in which the subject stepped with his left foot. The kinematics were recorded by the motion capture system, while the kinetic response was obtained through the force plates.

After this description of all the data that was obtained in the laboratory, in the following sections, it is explained how the collected data was used to not only preprocess the foot model but also as input for the simulations in which it was subsequentially utilized

6.3 Preprocessing of the Foot Model

Once the foot's geometry was obtained through 3D scanning, the output file was opened in GID (GID Simulation, Barcelona, Spain) with the purpose of initiating its preprocessing procedure.

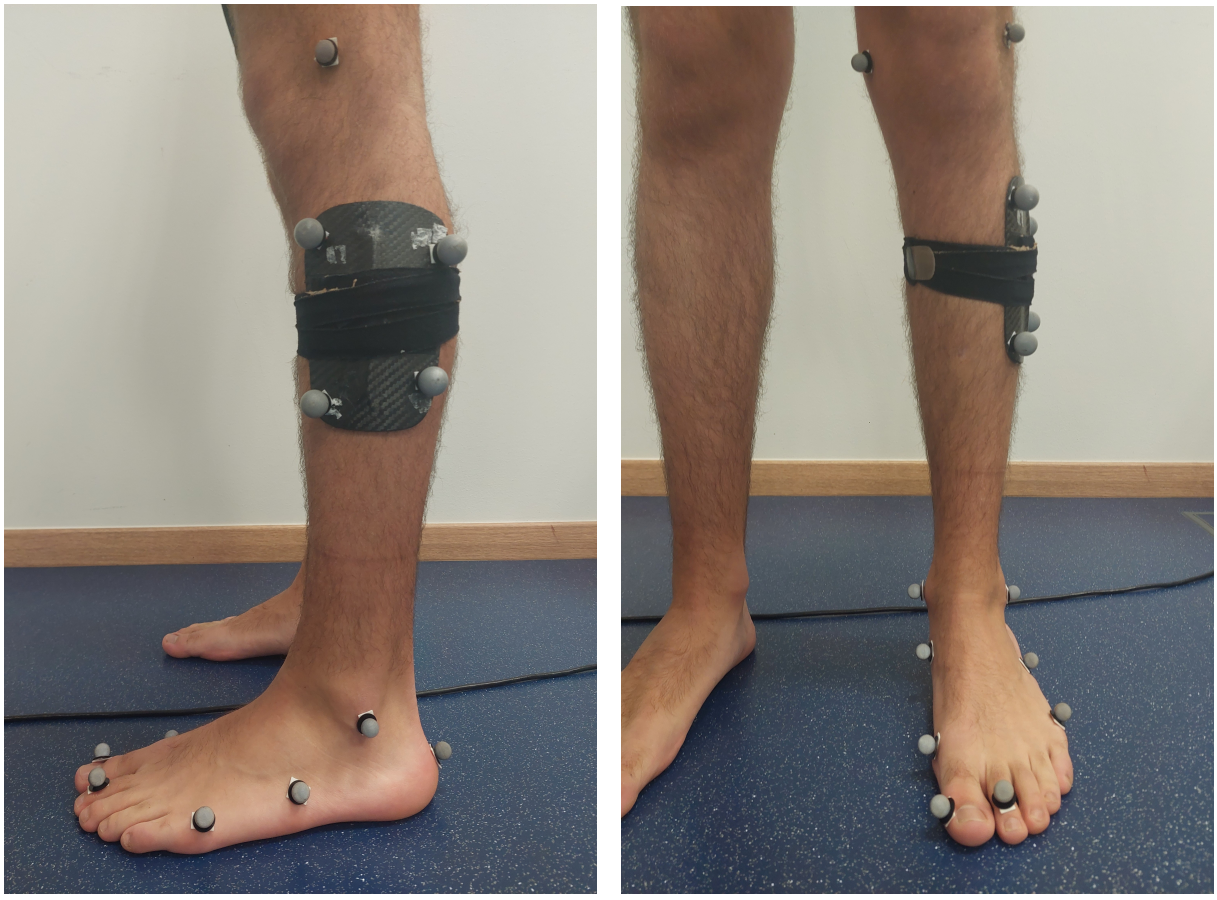

(a) (b)

Figure 6.5: Positioning of reflective markers for the gait cycle trial: side view (a) and front view (b).

Firstly, the geometry was cut at the ankle joint level. This decision was motivated by the fact that, at this stage of development, the main focus is to simulate the contact between a human foot and the ground. Therefore, the leg area will not register contact with another body during a gait cycle and its inclusion in the simulations will only contribute to reduce computational efficiency. Additionally, since the considered foot model does not represent realistically the behavior of joints, by encompassing the ankle joint, another level of inaccuracy would have been introduced to the model.

Secondly, once the desired geometry was achieved, a volume mesh was generated. Some areas required manual correction of elements in order to guarantee the best uniform distribution possible. This was specifically important at the top of the foot, in the irregular surface that resulted from the geometry's cut, as the elements were big and irregular, and this could compromise the results. Smoothing was avoided with the purpose of losing as little definition as possible of the foot surface's details, in order to assure a realistic contact surface. Additionally, it was necessary to associate the foot to an equivalent homogeneous material, meaning that a Young modulus and a Poisson ratio had to be defined. This was obtained through a trial and error process that used the results determined through the static deformation test previously described. In *SimPlas*, the contact between the foot and the ground with a relative deformation of $\delta = \Delta z = 8.8\ mm$ was simulated multiple times, while the values of the material's E and ν and the orientation of the foot were tweaked, until a realistic response was achieved. The final iteration

Figure 6.6: Force plates and surrounding motion capture system.

is presented in Figure 6.7 and the corresponding parameter values are: $E = 3.62MPa$, $\nu = 0.3$. This initial calibration of the foot model was done through a qualitative comparison of the obtained results with the pressure distribution associated with the experimental trial. It is worth noting that a quantitative and more robust calibration of the model could be done in the future. An optimization process based on deep learning could be a great solution for tackling the multiple variables that characterize this problem. This possibility is further discussed at the end of this document. It is also important to note that the obtained mechanical properties for this equivalent material fit the ones featured in the materials used for this type of applications. For external protheses, especially in applications like a prosthetic foot, a combination of flexibility and support is very important when choosing a material. One option is EVA (ethylene-vinyl acetate) foam, a copolymer of ethylene and vinyl acetate that is associated with a Young's Modulus between 1 and 4 MPa, which aligns with the obtained value of 3.62 MPa.

Thirdly, a mesh convergence study was performed and a satisfactory number and size of elements was attained. With h as the characteristic length of the elements, three meshes are presented ($h = 3\ mm$, $h = 4\ mm$ and $h = 5\ mm$). The three meshes are showcased in Figure 6.8 and its respective foot-ground contact test results are presented in Figures 6.9 and 6.10 in SI units (it is worth noting that the negative values of pressure are only related to the type of scale used; in the foot regions where contact does not occur, the pressure value is 0). In Figure 6.11 is possible to observe that the reaction

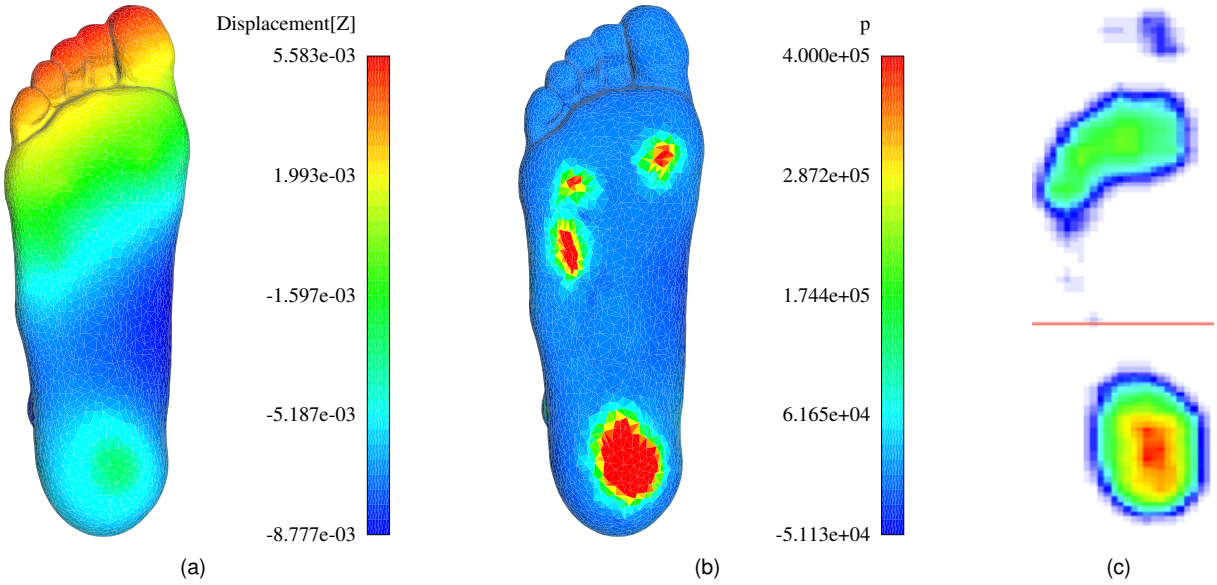

Figure 6.7: Local displacement (a), pressure distribution (b), experimental pressure distribution on the left foot sole (c).

force obtained for each one of the meshes is very similar and in accordance to the $622N$ measured in the deformation test performed in the laboratory. The mesh associated with $h = 4\ mm$ was chosen as the final mesh for the analyses that follows.

Before advancing into the use of this foot model in the context of foot-ground contact during gait, some remarks can be made about the model's strengths and limitations. Once again considering Figure 6.7, it is possible to observe some differences between the experimental data gathered and the most realistic foot model's response achieved. Firstly, as evidenced by the experimental data of pressure distribution, when a healthy human foot fully contacts with the ground, the resulting footprint includes contact of the biggest toe, sometimes even the second one. This was not possible to achieve with the computational model for two reasons. On the one hand, the foot's geometry features an elevation of the toes, as it can be observed in Figure 6.8. During the 3D scanning procedure, the subject was asked to rest his leg on top of a chair and maintain a 90 degree angle between the foot and the lower leg. The dorsiflexion movement of the foot required to maintain the said position promotes the extension of the toes, resulting in their elevation. On the other hand, since the model does not feature metatarsophalangeal joints, the contact of the metatarsal region with the ground results in an additional elevation of the toes. This is evident by the positive displacement associated that area. Secondly, the pressure distribution on the metatarsal region was not as significant as the one evidenced in the experimental data. The absence of contact in the middle section is associated with the application of an unrealistic high stiffness value for that region, in consequence of considering a homogeneous equivalent stiffness for the entirety of the foot. This prevented the foot from bending, as it should do, and achieve full contact in the metatarsal region.

Both these differences between the computational response of the foot model and the experimental data were mitigated by expanding the *clamped* region closer to the foot's bottom. This region is composed by nodes, in which all DoFs are restricted and its purpose is to simulate the foot's connection to

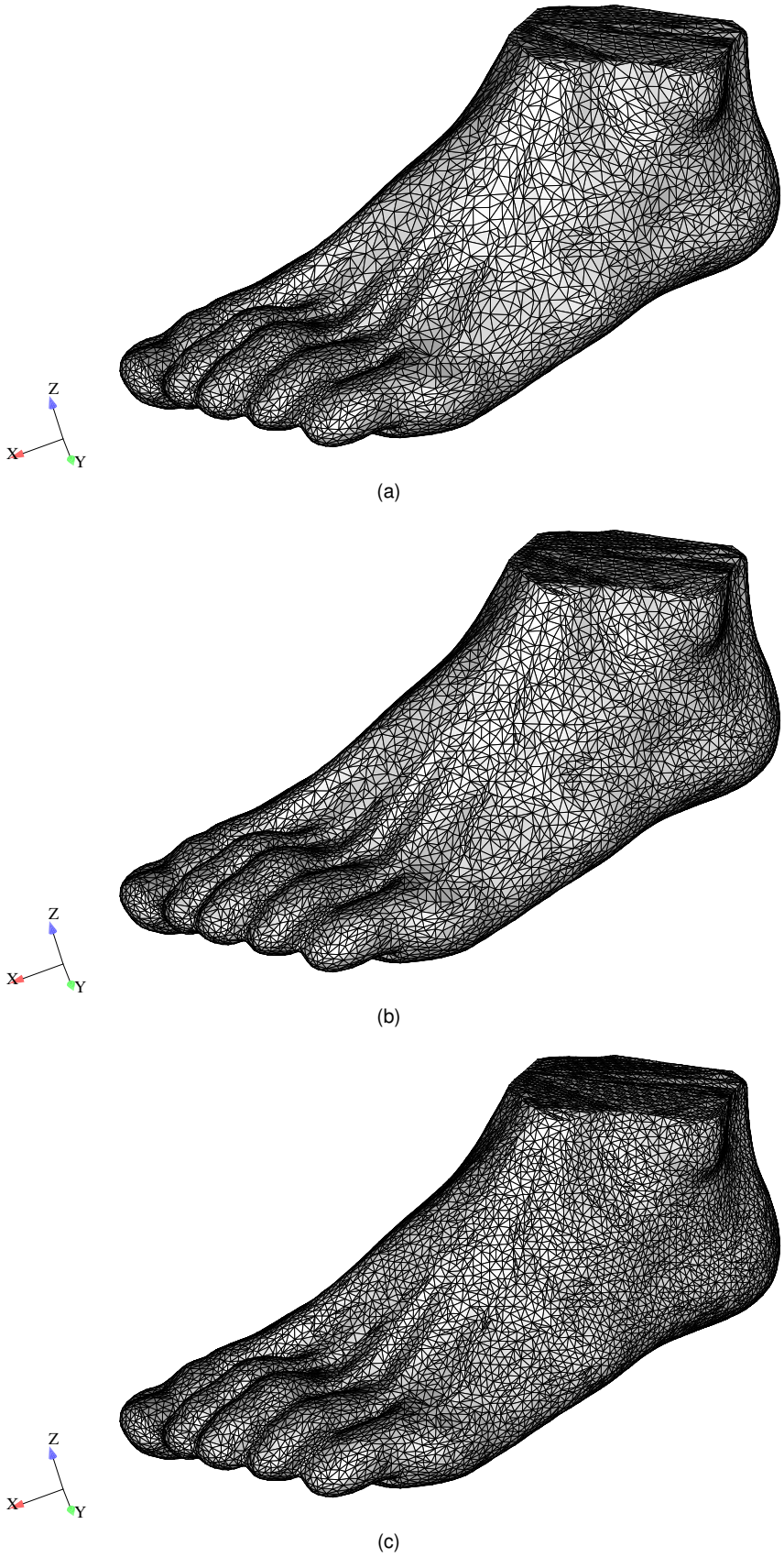

Figure 6.8: Coarse mesh ($h = 3\ mm$) (a), medium mesh ($h = 4\ mm$) (b), fine mesh ($h = 5\ mm$) (c).

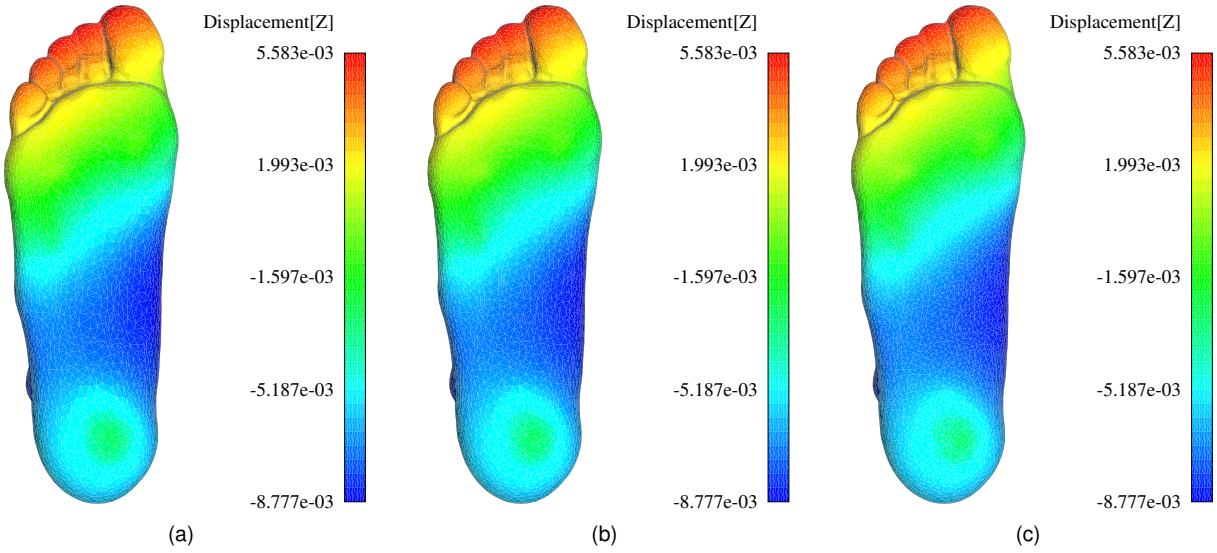

Figure 6.9: Local displacement of coarse mesh ($h = 3\ mm$) (a), medium mesh ($h = 4\ mm$) (b), fine mesh ($h = 5\ mm$) (c).

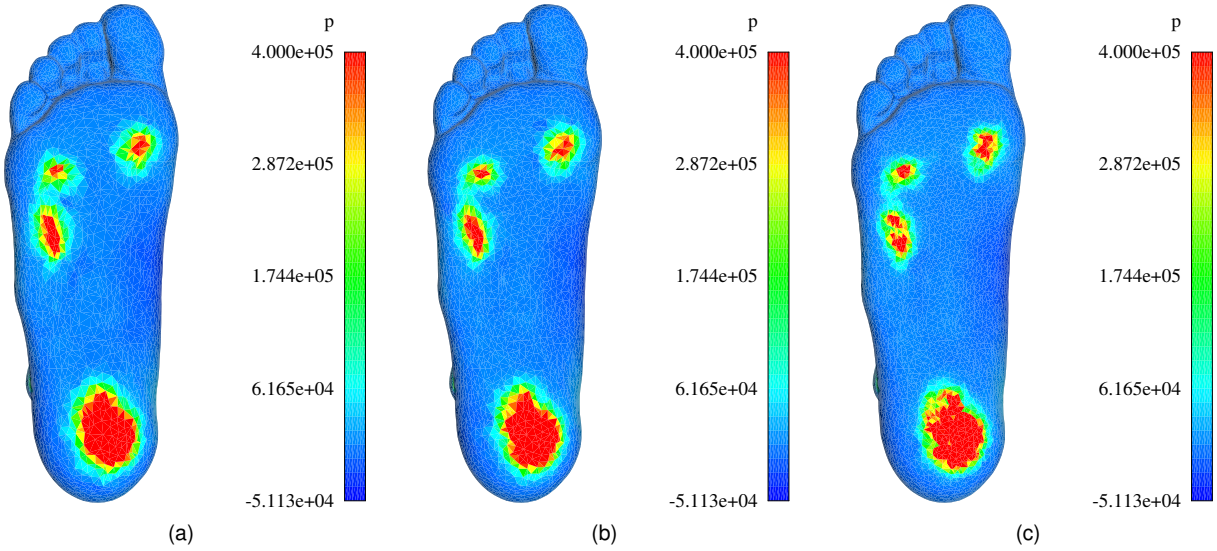

Figure 6.10: Pressure distribution of coarse mesh ($h = 3\ mm$) (a), medium mesh ($h = 4\ mm$) (b), fine mesh ($h = 5\ mm$) (c).

the rest of the human body, considering the absence of the internal skeletal structure of bones. The chosen nodes are located at the top of the foot. However, if the *clamped* region is expanded down and it becomes less concentrated on the posterior portion of the foot, more contact in the metatarsal and toe areas is achieved. However, this increased restriction proved to be incompatible with the use of the foot model in gait simulations. The purpose of this region is discussed in the next section.

6.4 Foot-Ground Contact during Gait

With a tuned foot model ready to be used in simulation and the gathering of the required kinematic data complete, the conditions for studying the foot-ground contact during gait are all available.

The co-simulation methodology used for simulating the gait movement was identical to the one used

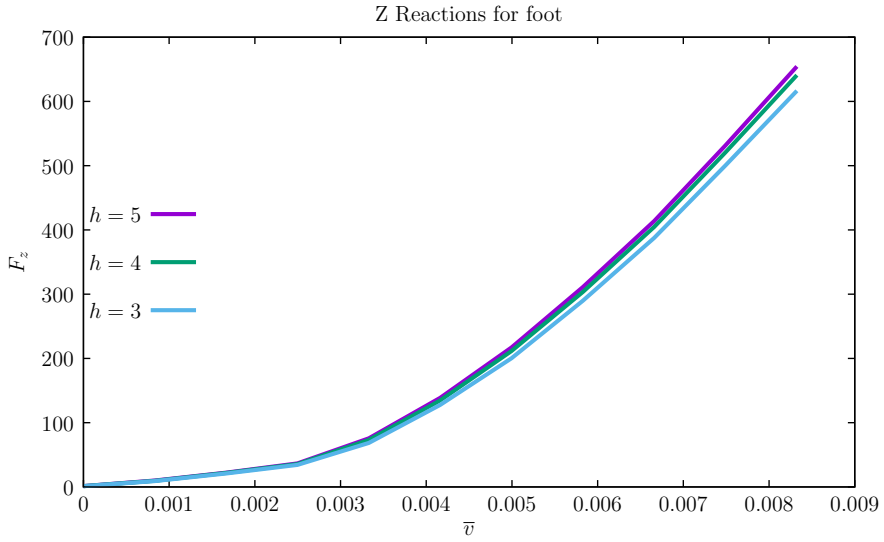

Figure 6.11: Reaction forces associated with the deformation test for three different meshes.

for the bouncing ball example with two exceptions. First, the introduction of the *clamped* region that is defined in *SimPre*, during the preprocessing procedure. Second, given that the human foot is a much more geometrically complex body than a sphere, the definition of vector $\boldsymbol{s}_j^{jj'}$ is not as easily deduced as in the case of the bouncing ball problem (see equation (5.18)).

In order to determine this vector that connects the CoM of the foot (origin point of reference frame (*j*)) and the origin point of reference frame (*jj*), expressed in the local coordinates of reference frame (*j*), kinematic data gathered during a static trial was used.

The kinematic data associated with a gait cycle gathered in the laboratory was used as input to study the contact forces and pressure distribution between the subject's left foot and the ground. Although the followed procedure features the same steps as an inverse dynamics analysis, the present analysis was carried out only until the contact forces were calculated. A complete inverse dynamics analysis, that would allow for the calculation of the moments of force at the ankle joint fall outside the scope of the present work, as such would require a more detailed and complex biomechanical model. Therefore, the relative position of the ground in regards to the foot is deduced by the multibody code from the kinematic data. Once again, this information is communicated to *SimPlas*, that returns to the multibody side the corresponding contact forces (ground reaction forces).

It is important to note that, in order to achieve a realistic result in terms of contact forces between the foot and the ground, a Coulomb friction model was implemented and a coefficient of friction of 0.3 was considered [66]. Although this value can be considered as low, simulations using higher values were done with very similar results.

Next, the results obtained for the simulation of a gait cycle are presented. From the full movement, the five most important moments that characterize gait were selected: heel strike (Figure 6.12), foot flat (Figure 6.13), heel-off (Figure 6.14), toe-off (Figure 6.15) and swing (Figure 6.16). For each one of the moments, the foot deformation and respective pressure distribution obtained are presented in SI units, alongside the experimental pressure distribution measured in the laboratory. It is worth noting that the reference frame displayed in each figure corresponds to reference frame (*j*).

(a)

(b)

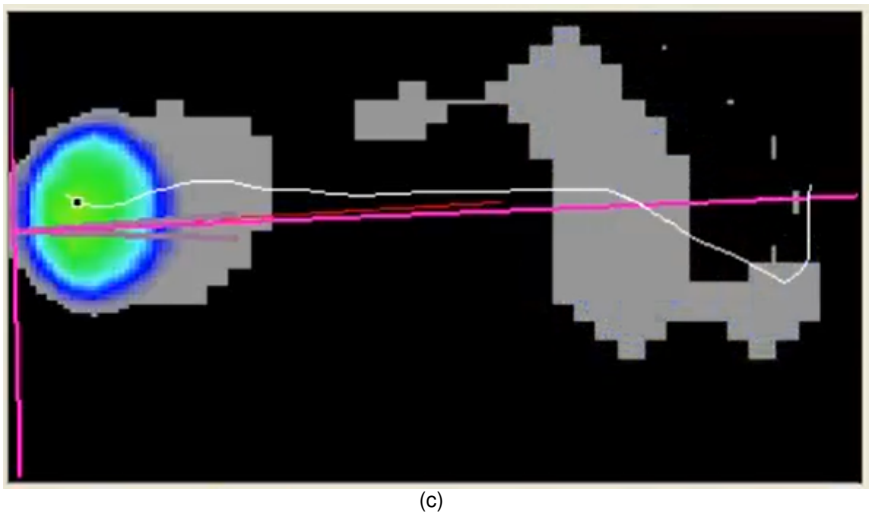

(c)

Figure 6.12: Heel strike: foot deformation (a), pressure distribution (b) and experimental pressure distribution (c).

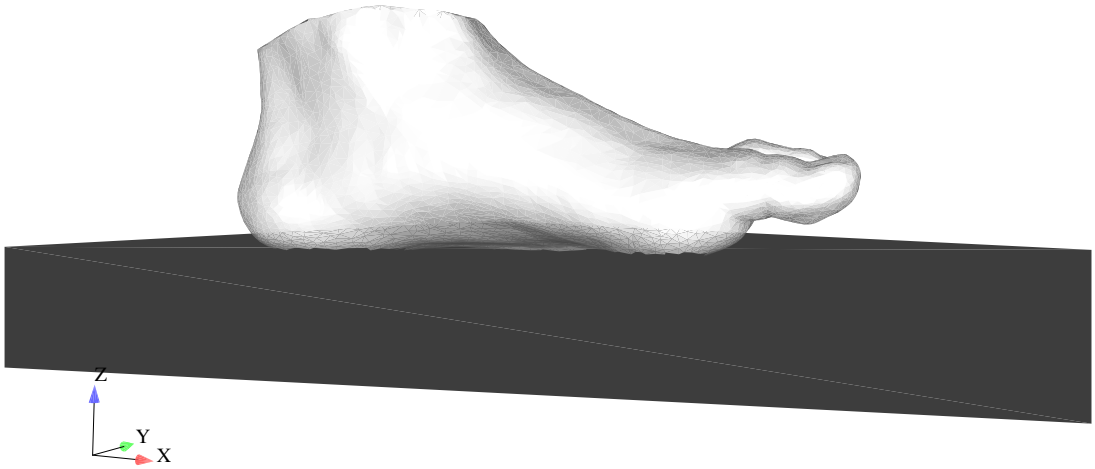

(a)

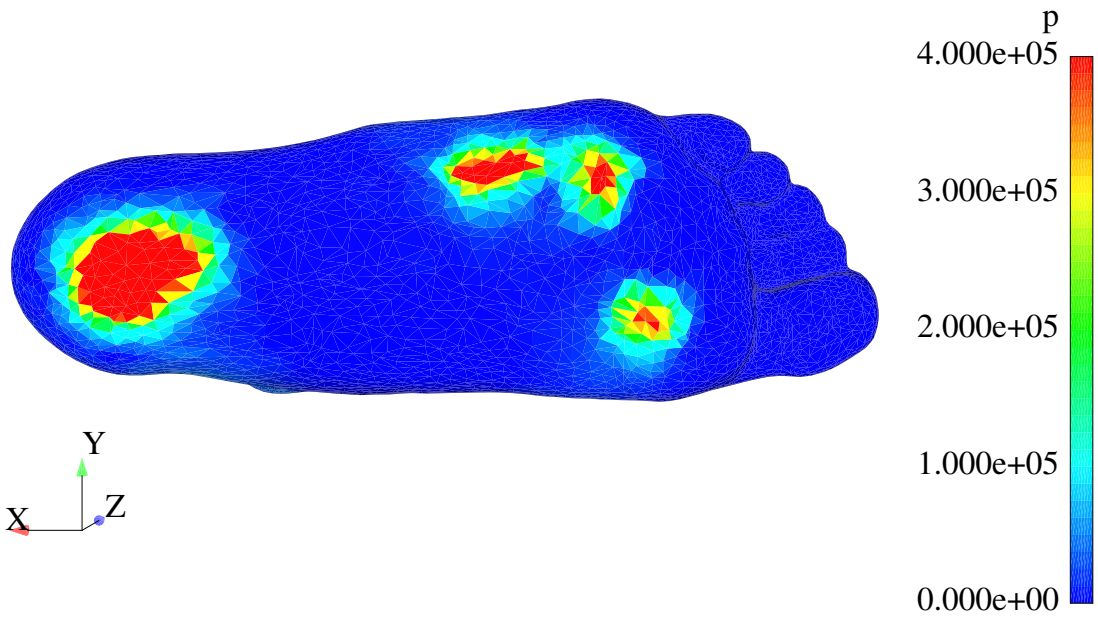

(b)

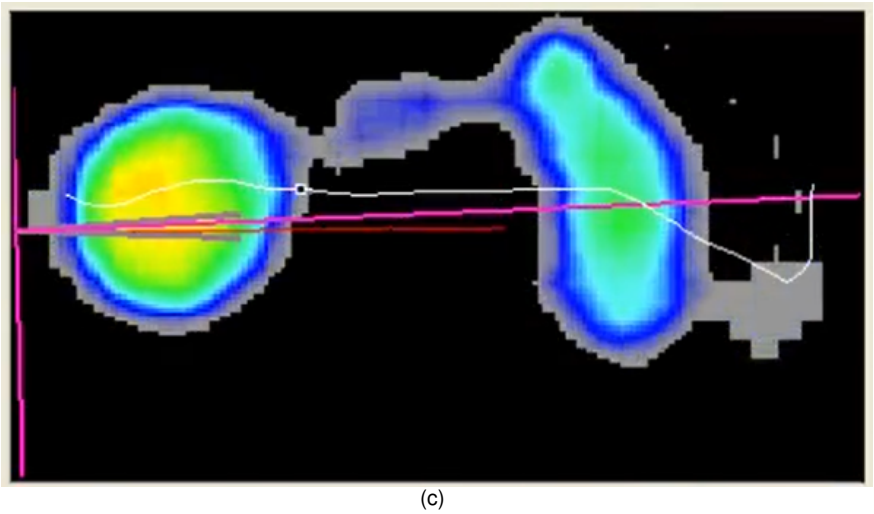

(c)

Figure 6.13: Foot flat: foot deformation (a), pressure distribution (b) and experimental pressure distribution (c).

(a)

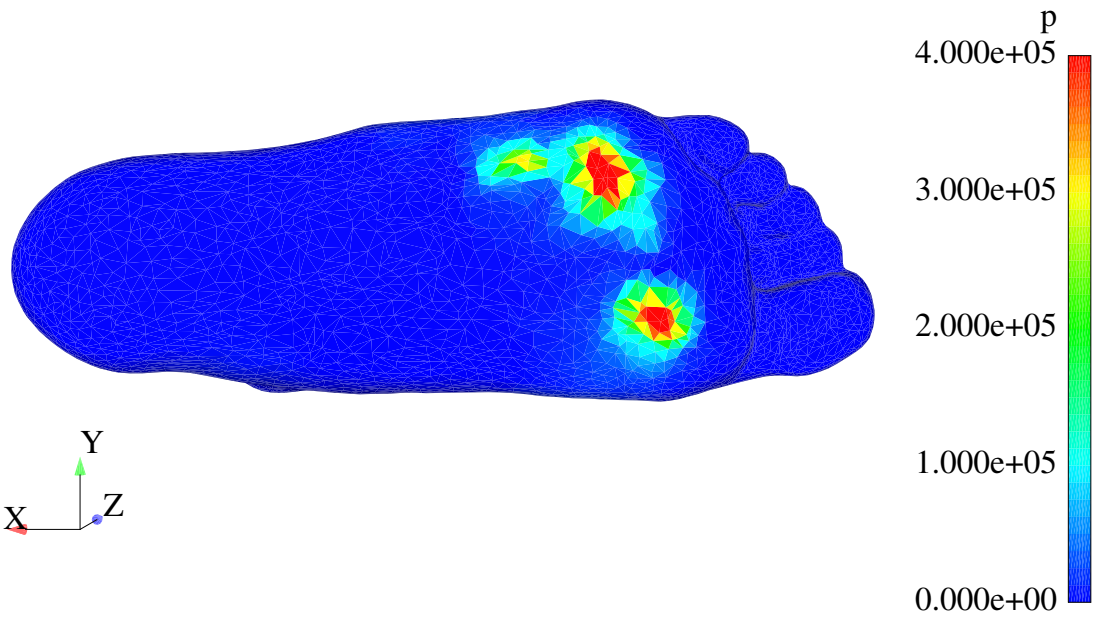

(b)

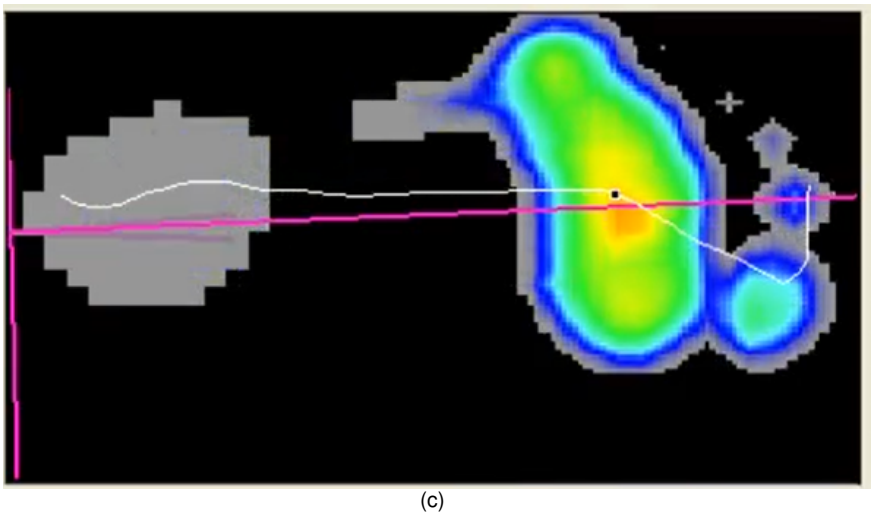

(c)

Figure 6.14: Heel-off: foot deformation (a), pressure distribution (b) and experimental pressure distribution (c).

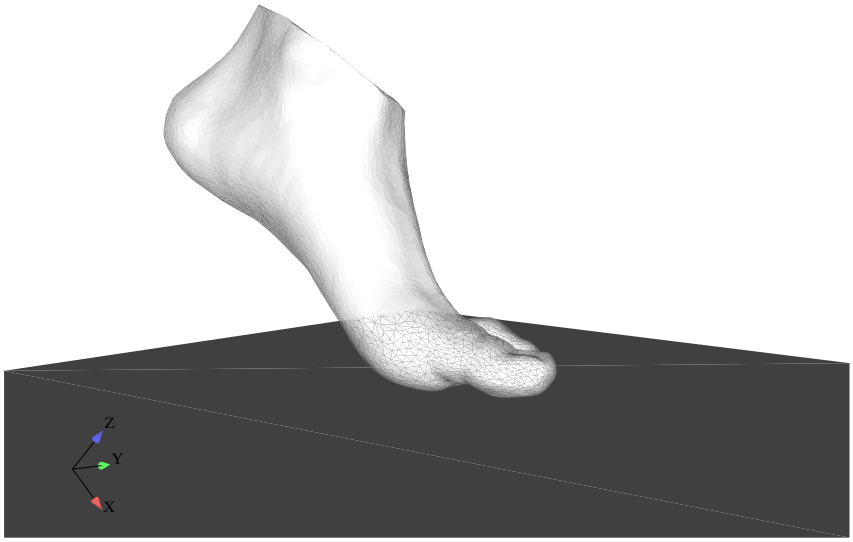

(a)

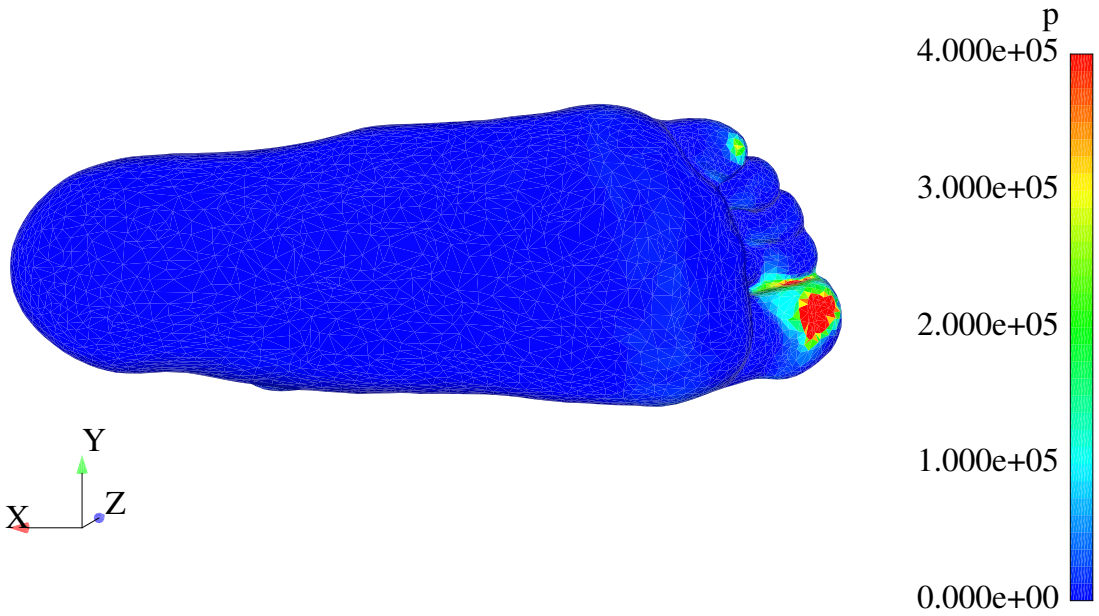

(b)

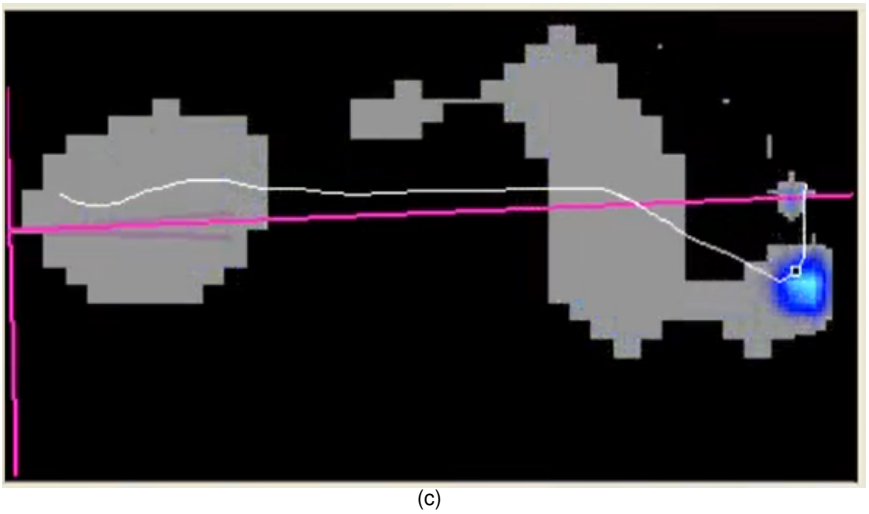

(c)

Figure 6.15: Toe-off: foot deformation (a), pressure distribution (b) and experimental pressure distribution (c).

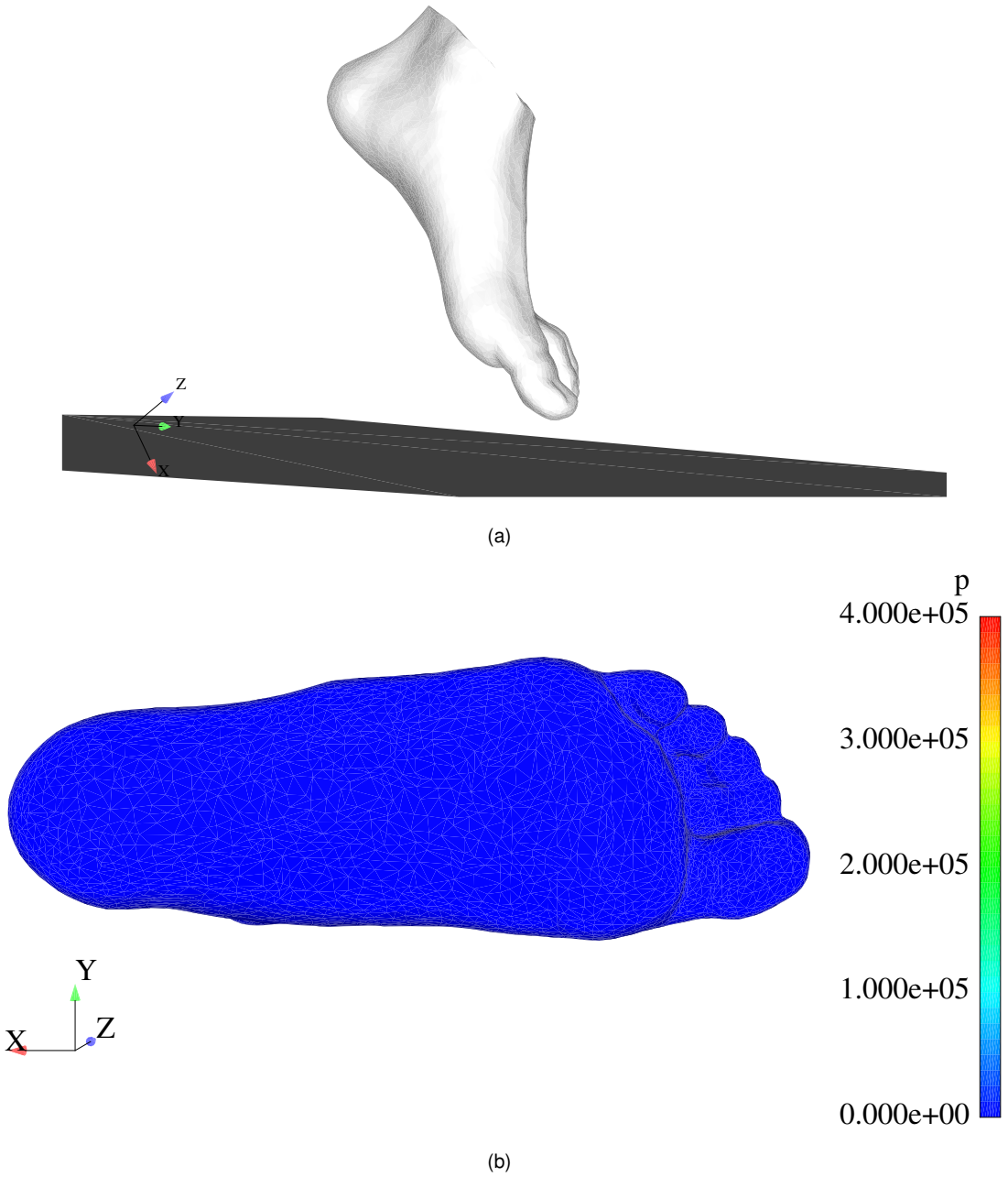

Figure 6.16: Swing: foot deformation (a) and pressure distribution (b).

The obtained pressure distribution is in accordance with the correspondent experimental data: through a qualitative comparison, it is possible to observe the similarities between the pressure footprints for each of the five moments (there is pressure distribution for the swing moment because there is no pressure being registered) and, in a quantitative capacity, the peak values registered in the experimental data were $4.2e+05Pa$ for the heel region, $4.8e+05Pa$ for the metatarsal region, similar to the ones obtained in the results.

Additionally, the obtained ground reaction forces are presented in Figure 6.17 for F_x, Figure 6.18 for F_y and Figure 6.19 for F_z.

From observing Figures 6.17, 6.18 and 6.19 it is clear that in some instances the ground reaction forces obtained in the simulation are similar to the experimental data, while in other sections of the movement they present different values. The analysis of these forces can be divided between F_x and

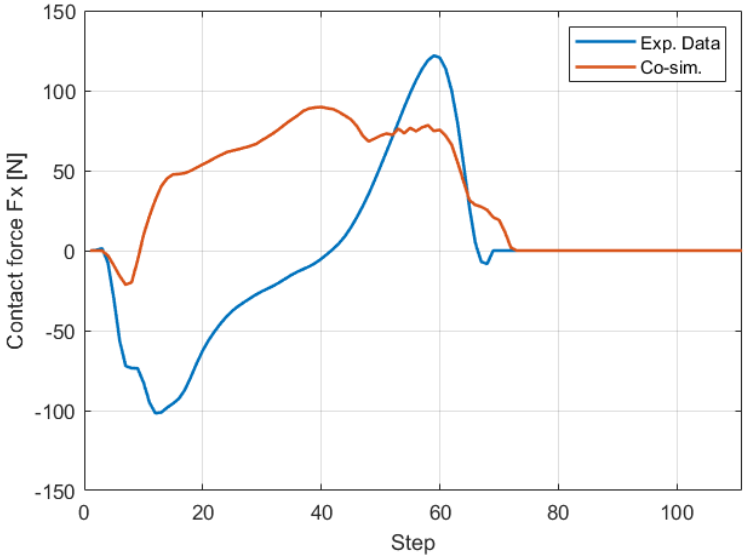

Figure 6.17: Ground reaction force (coordinate *x*).

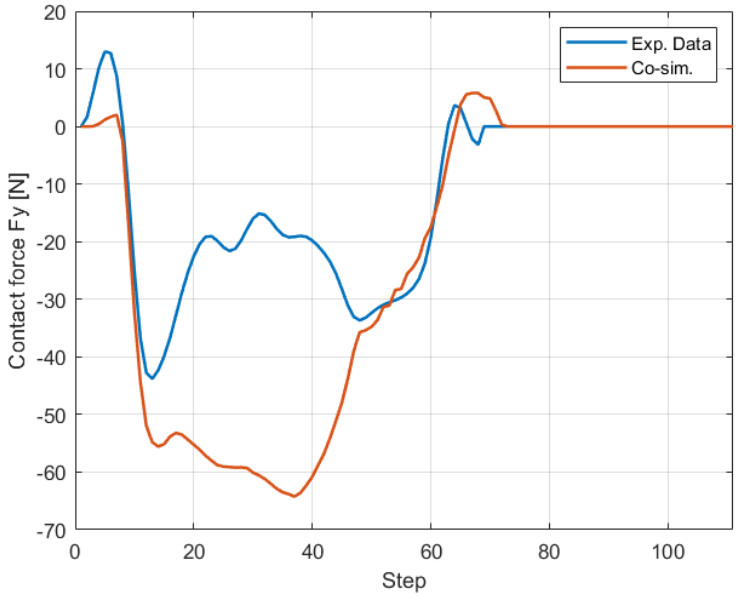

Figure 6.18: Ground reaction force (coordinate *y*).

F_y, which are forces closely related to the friction between the foot and the ground, and F_z, which represents the component of the force normal to the contact plane.

Starting from the analysis of F_z, the first point worth highlighting is the correspondence between the subject's full weight ($622\ N$) and the obtained results. The subject's full body weight usually corresponds to a value slightly below the first force peak, and thus, this result is in accordance to the previously calculated value. However, the results obtained do not feature a second peak. This is related to a very light contact between the toes and the ground. As previously referred, since that in the foot's geometry used the toes are elevated, its interaction with the floor is decreased and in the place of a second force peak, the results show a sudden drop in the force value. In future analyses, it is very important to aim for a more neutral position while its geometry is being scanned. A more correctly positioned foot will lead to

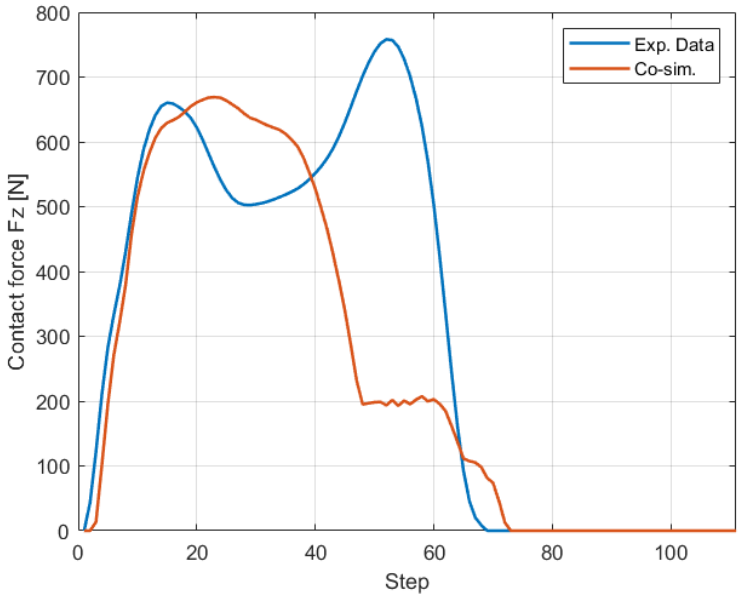

Figure 6.19: Ground reaction force (coordinate *z*).

a more realistic model and, thus, more realistic results. Additionally, the lack of a drop in the force value during foot flat (region between the two peaks of force) can be related to a high stiffness of the foot arch that does not allow the foot to fully contact with the ground.

Moving on to F_x, some challenges associated with the friction model used are highlighted in the results. Since *SimPlas* solves each step as a static contact problem, no information is provided about the history of the system, namely the relative velocity of the contacting bodies. This can be related to the differences seen between the obtained results and the experimental data in the F_x values. In the experimental data, in the first half of the movement the foot is breaking and, therefore, the respective friction force is negative (opposite to the direction of the velocity). In the second half of the movement the foot pushes back the ground to propel the body forward and, naturally, the friction force is positive (once again, opposite to the foot's movement). In the first half, the contacting velocity is positive and reducing, while in the second half, it is null and increasing. Since the implemented friction model does not feature knowledge of the previous step, it is always assumed that the contacting velocity is null. This explains why the obtained results present positive forces during both halves of the movement.

Finally, focusing now on F_y, a very similar behavior is registered between heel strike and the lowering movement of the foot. However, once the anterior portion of the foot initiates contact with the floor, the force values felt by the foot model differ from the ones registered in the laboratory. This can be related to the orientation of the foot geometry during the simulation. As evidenced in Figure 6.12, a slight inversion of the foot is visible, resulting in an increase of the force in the medial direction. Once heel-off occurs the experimental data and the obtained results present, once again, a high level of similarity.

It is worth noting that, although both F_x and F_y are associated with friction forces, since the gait movement is performed mainly in the saggital plane, bigger differences were expected in the x coordinate of the ground reaction forces than in the y coordinate, which is mainly associated with foot stabilization.

As an additional observation, it possible to verify that the pressure distribution associated with the

moment of foot flat is very similar to the one obtained in the deformation test, both resulting from the support of the subject's full body weight (see Figure 6.20).

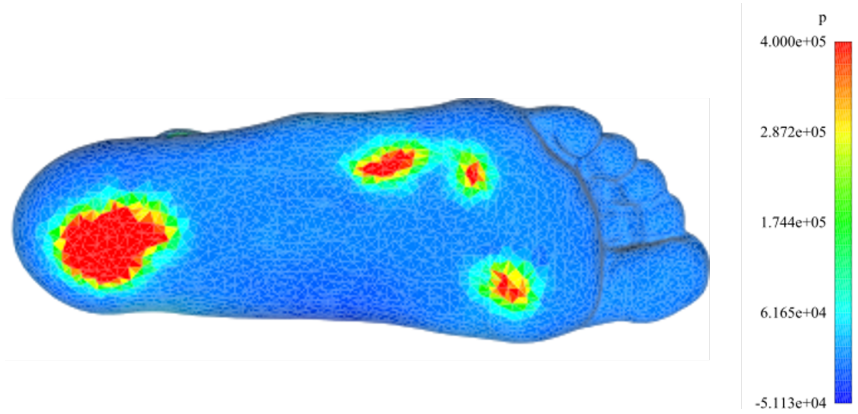

(a)

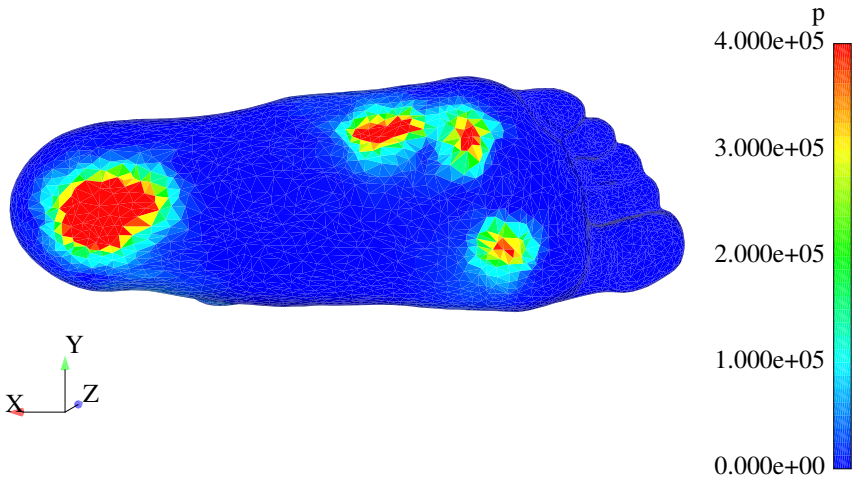

(b)

Figure 6.20: Foot flat: foot deformation (a) and pressure distribution (b).

Although some limitations of the foot model conditioned the realism of the obtained results, it is important to highlight the benefits of the co-simulation methodology used. The positioning of the foot in regards to the ground was done correctly, as evidenced by the realistic deformation of the foot throughout the gait cycle. The software was able to handle a large number of contact points and in different regions of the contacting bodies. When considering inverse dynamic analyses, the simulation time is small, proving that the communication between programs is efficient. The desired objective of combining the simplicity of MSD with the detailed structural analysis of FEM was fulfilled, proving that co-simulation methodologies that connect these two fields of engineering can create tools with a lot of potential in the future.

Chapter 7

Conclusions

7.1 Final Considerations

A co-simulation methodology that features the use of a Multibody System Dynamics (MSD) software in constant communication with a Finite Element Method (FEM) program in order to simulate the foot-ground contact during gait was presented and discussed in this work. The combination of the simplicity and efficiency of the multibody formulation in handling the global kinematics and kinetics of the system with the detailed structural analysis provided by FEM resulted in a successful strategy.

Through the input kinematic data regarding the gait movement, in an inverse dynamic analysis, the multibody code provides the relative position of the two contacting bodies to the FEM software, which statically solves each contact problem presented in each step. It starts by performing contact detection, followed by the subsequent calculation of the contact forces. The system was also used in forward dynamic analysis for less complex contact events, such as the benchmark problem of the bouncing ball, in which the communication between codes was continuous and bilateral.

On the multibody side, a contact module was added to a *Matlab* software developed in house. First, a simpler contact model proposed by Flores et al. [51] was implemented, allowing for better understanding of the contact phenomena and the structure of the program. On the FEM side, a *Fortran* program was adapted and further developed to feature the system's contact model. Static condensation was implemented, increasing the computational efficiency during simulations. The communication between programs was done through text files.

In order to analyze the foot-ground contact for the gait cycle, a foot model was developed. This model is characterized by a high level of geometric realism, since a 3D scan of a subject's left foot was acquired. However, the model presents a low physiological level of resemblance to a human foot, since it does not feature any bone, muscle or joint behavior in its structure. An equivalent homogeneous material was used for the entire foot and its mechanical properties were obtained through a calibration process based on experimental data gathered in a laboratory setting.

When simulating the foot-ground contact, the developed system provided satisfactory results in regards to the ground reaction forces and the pressure distribution, proving the potential of the adopted co-

simulation methodology. Some relevant discrepancies were highlighted, resulting from the foot model's limitations combined with a simple Coulomb friction model, which requires improvement with the addition of dynamic information about the history of the system.

With further development, this type of methodology could be seen as a powerful alternative to expensive laboratory equipment, such as force plates, when performing motion analysis.

Finally, it is important to note that this work was an initial step in the development of a methodology capable of simulating not only contact between humans and the surrounding environment, but also contact in the human-machine interface of exoskeleton users. Even though further development is required, the combination of MSD and FEM in a co-simulation methodology to simulate contact can be seen as a powerful tool in future analyses.

7.2 Future Work

As previously stated, further development is required in order to increase the realistic nature of the obtained results.

Firstly, a more realistic foot model can be developed. This can be achieved by either featuring bone, muscle and joint structures in the model or by performing a more robust calibration the foot's equivalent homogeneous material. For the latter, an optimization procedure using deep learning to determine the mechanical parameters of the material to use can lead to better behavior of the foot model.

Secondly, the use of dynamic boundary conditions would remove the need of a *clamped* region. This would more closely simulate the contact phenomena and, furthermore, it would contribute for more accurate friction forces.

Thirdly, the use of a different integrator with a higher level of user control is needed. In simulations in which forward dynamic analysis was performed, the behavior of the integrator was hard to control and predict, resulting in long simulation times with very limited results.

Fourthly, parallelization of the software could be advantageous if multiple contact events are to be analyzed at the same time.

Fifthly, the determination of the center of pressure (CoP) can be added as a possible output of the system to allow for a more complete analysis of the movement. Furthermore, considering the application of a more complete pressure analysis to exoskeleton design, a better understanding of the user's comfort with more detailed data will be possible.

Finally, since the geometry of the model of the contacting bodies can be obtained through 3D scanning, the methodology presented can be applied to any body section. Contact simulations of the upper limbs should also be considered if full body exoskeletons are to be studied.

References

[1] V. Kumar, Y. V. Hote, and S. Jain. Review of exoskeleton: history, design and control. In *2019 3rd international conference on recent developments in control, automation & power engineering (RDCAPE)*, pages 677–682. IEEE, 2019.

[2] J. C. Perry, J. Rosen, and S. Burns. Upper-limb powered exoskeleton design. *IEEE/ASME transactions on mechatronics*, 12(4):408–417, 2007.

[3] D. Hill, C. S. Holloway, D. Z. M. Ramirez, P. Smitham, and Y. Pappas. What are user perspectives of exoskeleton technology? a literature review. *International journal of technology assessment in health care*, 33(2):160–167, 2017.

[4] J. Wang, X. Li, T.-H. Huang, S. Yu, Y. Li, T. Chen, A. Carriero, M. Oh-Park, and H. Su. Comfort-centered design of a lightweight and backdrivable knee exoskeleton. *IEEE Robotics and Automation Letters*, 3(4):4265–4272, 2018. doi: 10.1109/LRA.2018.2864352.

[5] G. Serrancolí, A. Falisse, C. Dembia, J. Vantilt, K. Tanghe, D. Lefeber, I. Jonkers, J. De Schutter, and F. De Groote. Subject-exoskeleton contact model calibration leads to accurate interaction force predictions. *IEEE Transactions on Neural Systems and Rehabilitation Engineering*, 27(8):1597–1605, 2019. doi: 10.1109/TNSRE.2019.2924536.

[6] N. M. B. Monteiro, M. P. T. da Silva, J. O. M. G. Folgado, and J. P. L. Melancia. Structural analysis of the intervertebral discs adjacent to an interbody fusion using multibody dynamics and finite element cosimulation. *Multibody System Dynamics*, 25:245–270, 2011.

[7] J. H. Müller, S. Razu, A. Erdemir, and T. M. Guess. Prediction of patellofemoral joint kinematics and contact through co-simulation of rigid body dynamics and nonlinear finite element analysis. *Computer methods in biomechanics and biomedical engineering*, 23(11):718–733, 2020.

[8] J. Ambrósio, J. Pombo, F. Rauter, and M. Pereira. A memory based communication in the co-simulation of multibody and finite element codes for pantograph-catenary interaction simulation. *Multibody Dynamics: Computational Methods and Applications*, pages 231–252, 2009.

[9] S. Dietz, G. Hippmann, and G. Schupp. Interaction of vehicles and flexible tracks by co-simulation of multibody vehicle systems and finite element track models. *Vehicle system dynamics*, 37(sup1): 372–384, 2002.

[10] B. Olivier, O. Verlinden, and G. Kouroussis. A vehicle/track/soil model using co-simulation between multibody dynamics and finite element analysis. *International Journal of Rail Transportation*, 8(2): 135–158, 2020.

[11] L. Saraiva, M. R. da Silva, F. Marques, M. T. da Silva, and P. Flores. A review on foot-ground contact modeling strategies for human motion analysis. *Mechanism and Machine Theory*, 177: 105046, 2022.

[12] F. Moissenet, C. Bélaise, E. Piche, B. Michaud, and M. Begon. An optimization method tracking emg, ground reactions forces, and marker trajectories for musculo-tendon forces estimation in equinus gait. *Frontiers in neurorobotics*, 13:48, 2019.

[13] Y. Jung, M. Jung, J. Ryu, S. Yoon, S.-K. Park, and S. Koo. Dynamically adjustable foot-ground contact model to estimate ground reaction force during walking and running. *Gait & posture*, 45: 62–68, 2016.

[14] S. R. Hamner, A. Seth, and S. L. Delp. Muscle contributions to propulsion and support during running. *Journal of biomechanics*, 43(14):2709–2716, 2010.

[15] M. Q. Liu, F. C. Anderson, M. H. Schwartz, and S. L. Delp. Muscle contributions to support and progression over a range of walking speeds. *Journal of biomechanics*, 41(15):3243–3252, 2008.

[16] K. Hase and N. Yamazaki. Computer simulation study of human locomotion with a three-dimensional entire-body neuro-musculo-skeletal model (i. acquisition of normal walking). *JSME International Journal Series C Mechanical Systems, Machine Elements and Manufacturing*, 45(4): 1040–1050, 2002.

[17] R. Fluit, M. S. Andersen, S. Kolk, N. Verdonschot, and H. F. Koopman. Prediction of ground reaction forces and moments during various activities of daily living. *Journal of biomechanics*, 47(10):2321–2329, 2014.

[18] K. Jansen, F. De Groote, W. Aerts, J. De Schutter, J. Duysens, and I. Jonkers. Altering length and velocity feedback during a neuro-musculoskeletal simulation of normal gait contributes to hemiparetic gait characteristics. *Journal of neuroengineering and rehabilitation*, 11:1–15, 2014.

[19] Y.-C. Lin and M. G. Pandy. Three-dimensional data-tracking dynamic optimization simulations of human locomotion generated by direct collocation. *Journal of biomechanics*, 59:1–8, 2017.

[20] P. Brown and J. McPhee. A 3d ellipsoidal volumetric foot–ground contact model for forward dynamics. *Multibody System Dynamics*, 42:447–467, 2018.

[21] P. Moreira. Development of a three-dimensional contact model for the foot-ground interaction in gait simulations. MSc Thesis in Biomedical Engineering, Escola de Engenharia da Universidade do Minho, Minho, Portugal, 2009.

[22] J. Baptista. Human-orthotic integrated biomechanical model for comfort analysis evaluation. MSc Thesis in Biomedical Engineering, Instituto Superior Técnico, Lisboa, Portugal, November 2011.

[23] V. Firouzi, A. Seyfarth, S. Song, et al. Biomechanical models in the lower-limb exoskeletons development: A review. 2023.

[24] G. Bao, L. Pan, H. Fang, X. Wu, H. Yu, S. Cai, B. Yu, and Y. Wan. Academic review and perspectives on robotic exoskeletons. *IEEE Transactions on Neural Systems and Rehabilitation Engineering*, 27 (11):2294–2304, 2019.

[25] M. Cenciarini and A. M. Dollar. Biomechanical considerations in the design of lower limb exoskeletons. In *2011 IEEE International conference on rehabilitation robotics*, pages 1–6. IEEE, 2011.

[26] A. Gesta, S. Achiche, and A. Mohebbi. Design considerations for the development of lower limb pediatric exoskeletons a literature review. *IEEE Transactions on Medical Robotics and Bionics*, 2023.

[27] C. Siviy, L. M. Baker, B. T. Quinlivan, F. Porciuncula, K. Swaminathan, L. N. Awad, and C. J. Walsh. Opportunities and challenges in the development of exoskeletons for locomotor assistance. *Nature Biomedical Engineering*, 7(4):456–472, 2023.

[28] N. Yagn. Apparatus for facilitating walking, running, and jumping. *U. S. Patents*, 1890.

[29] Berkeley lower extremity exoskeleton (bleex). `https://bleex.me.berkeley.edu/project/bleex/`. Accessed: 2023-10-15.

[30] Human universal load carrier (hulc). `https://www.army-technology.com/projects/human-universal-load-carrier-hulc/`. Accessed: 2023-10-15.

[31] Y. Sankai. Hal: Hybrid assistive limb based on cybernics. In *Robotics Research: The 13th International Symposium ISRR*, pages 25–34. Springer, 2011.

[32] elegs. `https://bleex.me.berkeley.edu/project/elegs/`. Accessed: 2023-10-15.

[33] Rewalk and restore. `https://rewalk.com/`, note = Accessed: 2023-10-15.

[34] Hal for medical use (lower limb type). `https://www.cyberdyne.jp/english/products/LowerLimb_medical.html`. Accessed: 2023-10-15.

[35] P. C. Silva, M. T. Silva, and J. M. Martins. Evaluation of the contact forces developed in the lower limb/orthosis interface for comfort design. *Multibody System Dynamics*, 24(3):367–388, 2010.

[36] M. L. Siefert. Concept analysis of comfort. In *Nursing Forum*, volume 37, page 16. Blackwell Publishing Ltd., 2002.

[37] Oxford's dictionary - comfort. `https://www.oxfordlearnersdictionaries.com/definition/english/comfort_1?q=comfort`. Accessed: 2023-08-24.

[38] A. E. Dubin, A. Patapoutian, et al. Nociceptors: the sensors of the pain pathway. *The Journal of clinical investigation*, 120(11):3760–3772, 2010.

[39] M. Melia, B. Geissler, J. König, H. J. Ottersbach, M. Umbreit, S. Letzel, and A. Muttray. Pressure pain thresholds: subject factors and the meaning of peak pressures. *European Journal of Pain*, 23 (1):167–182, 2019.

[40] S. R. Grabowski and G. J. Tortora. *Principles of anatomy and physiology*. Wiley New York/Chichester, 2000.

[41] Treatment options for foot ankle arthritis. `https://www.footankledc.com/news/treatment-options-for-foot-ankle-arthritis/114`. Accessed: 2023-10-17.

[42] Anatomical terminology: Developing a common language - body planes. `https://www.labxchange.org/library/pathway/lx-pathway:a06432a8-ddb3-4c1f-bb19-f02deb9fe530/items/lx-pb:a06432a8-ddb3-4c1f-bb19-f02deb9fe530:html:53109aae`. Accessed: 2023-10-17.

[43] P. Sui, L. Yao, J. S. Dai, and H. Wang. Development and key issues of the ankle rehabilitation robots. In *13th world congress in mechanism and machine science, Guanajuato*, pages A12–416, 2011.

[44] S. J. Hall. *Basic Biomechanics*. Mosby, 1995.

[45] M. W. Whittle. *Gait analysis: an introduction*. Butterworth-Heinemann, 2014.

[46] R. Baker. The history of gait analysis before the advent of modern computers. *Gait & posture*, 26 (3):331–342, 2007.

[47] M. Jacquelin Perry. Gait analysis: normal and pathological function. *New Jersey: SLACK*, 2010.

[48] J. Rueterbories, E. G. Spaich, B. Larsen, and O. K. Andersen. Methods for gait event detection and analysis in ambulatory systems. *Medical engineering & physics*, 32(6):545–552, 2010.

[49] T. Everett and C. Kell. *Human movement: An introductory text*. Elsevier health sciences, 2010.

[50] Laboratório de biomecânica de lisboa. `https://lbl.tecnico.ulisboa.pt/index.html`. Accessed: 2023-10-20.

[51] P. Flores, M. Machado, M. T. Silva, and J. M. Martins. On the continuous contact force models for soft materials in multibody dynamics. *Multibody system dynamics*, 25:357–375, 2011.

[52] G. Gilardi and I. Sharf. Literature survey of contact dynamics modelling. *Mechanism and machine theory*, 37(10):1213–1239, 2002.

[53] M. Machado, P. Moreira, P. Flores, and H. M. Lankarani. Compliant contact force models in multibody dynamics: Evolution of the hertz contact theory. *Mechanism and machine theory*, 53:99–121, 2012.

[54] H. Hertz. On the contact of solids—on the contact of rigid elastic solids and on hardness. *Miscellaneous papers*, pages 146–183, 1896.

[55] K. H. Hunt and F. R. E. Crossley. Coefficient of restitution interpreted as damping in vibroimpact. 1975.

[56] I. Roupa, S. B. Gonçalves, and M. T. da Silva. Kinematics and dynamics of planar multibody systems with fully cartesian coordinates and a generic rigid body. *Mechanism and Machine Theory*, 180:105134, 2023.

[57] Simplas. http://www.simplassoftware.com/.

[58] P. Dunaj, S. Berczyński, P. Pawełko, Z. Grzadziel, and M. Chodźko. Static condensation in modeling roller guides with preload. *Archives of Civil and Mechanical Engineering*, 19:1072–1082, 2019.

[59] A. Cammarata, R. Sinatra, and P. D. Maddìo. Static condensation method for the reduced dynamic modeling of mechanisms and structures. *Archive of Applied Mechanics*, 89:2033–2051, 2019.

[60] P. Areias, N. Sukumar, and J. Ambrósio. Continuous gap contact formulation based on the screened poisson equation. *Computational Mechanics*, pages 1–17, 2023.

[61] R. Courant. Variational methods for the solution of problems of equilibrium and vibrations. 1943.

[62] E. Beltrami. A constructive proof of the kuhn-tucker multiplier rule. *Journal of Mathematical Analysis and Applications*, 26(2):297–306, 1969.

[63] S. R. S. Varadhan. On the behavior of the fundamental solution of the heat equation with variable coefficients. *Communications on Pure and Applied Mathematics*, 20(2):431–455, 1967.

[64] J. Bonet and R. D. Wood. *Nonlinear continuum mechanics for finite element analysis*. Cambridge university press, 1997.

[65] T. D. Bui and T. Bui. Numerical methods for extremely stiff systems of ordinary differential equations. *Applied Mathematical Modelling*, 3(5):355–358, 1979.

[66] K. W. Li and H.-C. Wen. Friction between foot and floor under barefoot conditions: A pilot study. In *2013 IEEE International Conference on Industrial Engineering and Engineering Management*, pages 1651–1655. IEEE, 2013.